INSTITUTO POTOSINO DE INVESTIGACIÓN CIENTÍFICA Y TECNOLÓGICA, A.C.

POSGRADO EN CIENCIAS EN BIOLOGÍA MOLECULAR

"Light in biology as a measuring tool and as an environmental cue"

Tesis que presenta

Carmen Noemí Hernández Candia

Para obtener el grado de

Doctora en Ciencias en Biología Molecular

Director de la Tesis:

Dr. Braulio Gutiérrez Medina

IPICYT

Constancia de aprobación de la tesis

La tesis ***"Light in biology as a measuring tool and as an environmental cue"*** presentada para obtener el Grado de Doctora en Ciencias en Biología Molecular fue elaborada por **Carmen Noemí Hernández Candia** y aprobada el **veintitrés de mayo de dos mil diecisiete** por los suscritos, designados por el Colegio de Profesores de la División de Biología Molecular del Instituto Potosino de Investigación Científica y Tecnológica, A.C.

Dr. Braulio Gutiérrez Medina
Director de la tesis

Dr. J. Sergio Casas Flores
Miembro del Comité Tutoral

Dr. Gerardo Rafael Argüello Astorga
Miembro del Comité Tutoral

Dr. Samuel Lara González
Miembro del Comité Tutoral

Dr. Jay C. Dunlap
Miembro del Comité Tutoral

Créditos Institucionales

Esta tesis fue elaborada en el Laboratorio de Pinzas ópticas de la División de Materiales Avanzados del Instituto Potosino de Investigación Científica y Tecnológica, A.C., bajo la dirección del Dr. Braulio Gutiérrez Medina.

Durante la realización del trabajo el autor recibió una beca académica del Consejo Nacional de Ciencia y Tecnología (No. de registro 330541) y del Departamento de Biología Molecular del Instituto Potosino de Investigación Científica y Tecnológica, A. C.

El trabajo aquí presentado fue realizado gracias al apoyo de UCMEXUS-CONACYT, Fondos Sectoriales-SEP-2009 (CB-2009/133053), CONACYT SEP-CB-2013-01-223377, CONACYT-Fronteras de la Ciencia, Proyecto 1144

Agradecemos al Laboratorio de Genómica Funcional y Comparativa y al Laboratorio de Biología Estructural por permitirnos hacer uso de sus instalaciones. Agradecemos al Laboratorio Nacional de Investigaciones en Nanociencias y Nanotecnología (LINAN) por su apoyo para analizar muestras por medio de LC-MS/MS, TEM y SEM (CONACYT-MEXICO GRANT 56787 and INFRA-2013-01 No. 204373)

IPICYT

Instituto Potosino de Investigación Científica y Tecnológica, A.C.

Acta de Examen de Grado

El Secretario Académico del Instituto Potosino de Investigación Científica y Tecnológica, A.C., certifica que en el Acta 094 del Libro Primero de Actas de Exámenes de Grado del Programa de Doctorado en Ciencias en Biología Molecular está asentado lo siguiente:

En la ciudad de San Luis Potosí a los 23 días del mes de mayo del año 2017, se reunió a las 12:00 horas en las instalaciones del Instituto Potosino de Investigación Científica y Tecnológica, A.C., el Jurado integrado por:

Dr. Gerardo Rafael Argüello Astorga	**Presidente**	**IPICYT**
Dr. J. Sergio Casas Flores	**Secretario**	**IPICYT**
Dr. Braulio Gutiérrez Medina	**Sinodal**	**IPICYT**
Dr. Jay C. Dunlap	**Sinodal externo**	**Dartmouth College**

a fin de efectuar el examen, que para obtener el Grado de:

DOCTORA EN CIENCIAS EN BIOLOGÍA MOLECULAR

sustentó la C.

Carmen Noemí Hernández Candia

sobre la Tesis intitulada:

Light in biology as a measuring tool and as an environmental cue

que se desarrolló bajo la dirección de

Dr. Braulio Gutiérrez Medina

El Jurado, después de deliberar, determinó

APROBARLA

Dándose por terminado el acto a las 14:05 horas, procediendo a la firma del Acta los integrantes del Jurado. Dando fe el Secretario Académico del Instituto.

A petición de la interesada y para los fines que a la misma convengan, se extiende el presente documento en la ciudad de San Luis Potosí, S.L.P., México, a los 23 días del mes de mayo de 2017.

Dr. Horacio Flores Zúñiga
Secretario Académico

Mtra. Ivonne Lizette Cuevas Vélez
Jefa del Departamento del Posgrado

INSTITUTO POTOSINO DE INVESTIGACIÓN CIENTÍFICA Y TECNOLÓGICA, A.C.
IPICYT
SECRETARIA ACADEMICA

Dedicated to Ma del Carmen Candia

& David García Hernandez my loving parents.

Acknowledgements

Thanks to my beloved family for all their support along these years. Thanks to my father who taught me to question the world, thanks for always being behind me supporting and helping me to achieve my goals. To my mom who showed me that giving up is never an option and that self-improvement is always possible, thanks for helping me to believe in myself. To Eduardo who accompanied me along this adventure, making the journey unforgettable.

Thanks to Dr. Braulio Gutiérrez, he was a wonderful mentor always encouraging me to ask, seek and propose new ideas. His true love for science is contagious and I am so proud of have been part of his lab since its beginning. Thanks to Dr. Sergio Casas, who opened me the door of his lab and was always ready to have a nice talk about science, politics or my experimental troubleshoots. Thanks to all my tutorial committee for their support and teachings along these years.

Thanks to all the people that showed me how fun science is and thanks to all my friends that made me have a lot of fun even in those bad lab days. I am grateful for all the amazing people that I initially met as lab mates and now they have become friends for life.

Thanks to IPICYT and to the Molecular Biology Department for letting me become part of their community and thanks for giving me the resources and proper environment to transform myself into a happy biologist.

Table of Contents

List of figures

Appendixes

List of Abbreviations

3D	Three Dimensional
BF	Bright Field
BFM	Bright Field Microscopy
CEFBM	Computer Enhanced Bright Field Microscopy
MTs	Microtubules
PSF	Point Spread Function
PSFp	phase-Point Spread Function
SNR	Signal Noise Ratio
DNA	Deoxyribonucleic Acid
RNA	Ribonucleic Acid
dsDNA	Double Strand DNA
ssDNA	Single Strand DNA
CCD	Charge-Coupled Device
PSD	Position Sensitive Detector
(x,y,z)	Position of a trapped bead
(x0,y0,z0)	Equilibrium position of a trapped bead
(*x*,*y*,*z*)	Coordinated directions, z points in the direction of light propagation
FJC	Freely Jointed Chain
WLC	Worm Like Chain
Lp	Persistence Length
L_o	Contour Length
bp	base pair

sem	Standard Error form the Mean
BL	Blue Light
FAD	Flavin Adenine Dinucleotide
FMN	Flavin Mononucleotide
PAS	Period circadian protein-Aryl hydrocarbon receptor nuclear translocator protein-Single-minded protein
BLUF	Blue-Light Using FAD proteins
CRYs	Cryptochromes proteins
LOV	Light Oxygen Voltage
VVD	VIVID
WC-1	White Collar-1
WC-2	White Collar-2
NMR	Nuclear Magnetic Resonance
SEC	Size Exclusion Chromatography
TEM	Transmission Electron Microscopy
SEM	Scanning Electron Microscopy
miniSOG	mini Singlet Oxygen Generator
GST	Glutathione S-Transferase
PA	Protein Aggregation
BSA	Bovine Serum Albumina
GSH	Glutathione
DTT	Dithiothreitol

Resumen

La luz en la biología como una herramienta de medición y como un estímulo medioambiental

Tanto en los organismos como en la biología las interacciones de la luz con la materia tienen varias consecuencias. Para los organismos, una de las consecuencias ha sido el desarrollo de proteínas fotorreceptoras, con las cuales los organismos pueden adaptase mejor a las condiciones impuestas por la radiación solar. Por otro lado, la biología actual se beneficia de las interacciones luz-materia por medio de técnicas ópticas como la microscopía, la espectroscopia y los ensayos de fluorescencia entre muchos otros. En este trabajo se presentan dos técnicas ópticas para el estudio de procesos biológicos y se describe un nuevo efecto de la luz azul sobre el fotorreceptor VIVID (VVD). Primero, se presenta un método para potenciar la microscopía de campo claro por medio del procesamiento digital de imágenes, el cual permite visualizar objetos de fase con suficiente contraste tal que, por primera vez, fue posible adquirir la función de dispersión de punto para objetos de fase (FDPf) y se mostró que es posible aplicar algoritmos de deconvolución estándar para mejorar la calidad de las imágenes de células no teñidas. En segundo lugar, se construyó un sistema de pinzas ópticas para el estudio de moléculas individuales. El correcto funcionamiento de nuestro sistema de pinzas ópticas fue validado por medio de dos ensayos estándar: se midieron las propiedades elásticas de una cadena de ADN y se midió la fuerza máxima ejercida y el tamaño de paso del motor molecular cinesina. En tercer lugar, se trabajó con la flavoproteína fotorreceptora de luz azul VVD, la cual pertenece al hongo filamentoso *Neurospora crassa*. Se mostró que en condiciones *in vitro* VVD presenta agregación al ser oxidada por especies reactivas de oxígeno producidas por la misma proteína. Encontramos que la sensibilidad de VVD a la luz, el oxígeno y la temperatura regulan la cinética de agregación de la proteína. Con base en nuestras observaciones dilucidamos la ruta de agregación de VVD y proponemos que su agregación podría tener efectos en el hongo *N. crassa.*

PALABRAS CLAVE: Microscopía de campo claro | Función de dispersión de punto | Molécula única | fotorreceptores|

Abstract

Light in biology as a measuring tool and as an environmental cue

For organisms as for biology the light-matter interactions have several consequences. For organisms, one of these consequences has been the development of proteins specialized in light detection which provide organisms with a better fit to sunlight cues. On the other hand, current biology exploits the light-matter interactions through optical techniques such as microscopy, spectroscopy, and fluorescence assays among many others. Herein two optical techniques to study biological processes and a new effect of blue light over the photoreceptor protein VIVID (VVD) are presented. First, the power of bright field light microscopy was enhanced by digital image processing, which allows us to visualize sub-diffraction phase objects with enough contrast to acquire, for the first time, the phase point-spread function (PSF_P) of a bright field light microscope. As a proof of concept, we used the measured PSF_P to apply conventional deconvolution to bright field images, increasing image contrast and the definition of boundaries in unstained cellular samples. Second, an optical tweezers apparatus for single-molecule studies was built and tested by performing two standard single-molecule assays: stretching single dsDNA molecules, and measuring the step size and maximum sustainable load for the molecular motor kinesin. Third, the flavin-binding blue-light (BL) photoreceptor VIVID from the filamentous fungus Neurospora crassa was shown to present an in vitro aggregation mechanism triggered by a self-produced reactive oxygen species (ROS). We found that VIVID (VVD) is sensitive to light, oxygen and temperature and these factors modulate the aggregation of the protein. Based on our observations we elucidate an aggregation pathway for VVD and propose aggregation as a possible mechanism to regulate diverse processes in N. crassa.

Keywords: Bright field microscopy | Point spread function | Single molecule | photoreceptors|

Chapter 1. Introduction

How to define what is alive? Clearly, it is an important question. However, to set a precise definition is a tricky task. In the best of cases a list of characteristic traits common to all organisms has been proposed. These seven traits are: organization, metabolism, homeostasis, sensitivity, growth, reproduction, and evolution[1] with the condition that all these traits must be present to consider the system to be alive. This list helps to establish a border that separates the living from the non-living. However, this is not a satisfactory definition, since examples of obviously living organisms escape from the rule (such as mules, lacking the reproduction trait). Daniel Koshland proposes a set of seven traits that include the previously mentioned traits but provides a more open definition of what means being alive. These seven traits are: program, improvisation, compartmentalization, energy, regeneration, adaptability, and seclusion[2]. Surprisingly, all the traits described are sustained at the molecular level by only four kinds of macromolecules: lipids, carbohydrates, proteins and nucleic acids. So we can say that if something is formed by these four molecules of life and presents the enlisted common traits, then that entity has a good probability of being alive.

Molecular biology, biochemistry and biophysics are endeavored to provide a bottom-top approach to understand living beings, and have been focused in explaining processes involving the four macromolecules of life. Accordingly, a proper set of experimental tools and measuring probes that allow reproducible and quantitative measurement are required -- and light has become the keystone to fulfill that demand. The convergence between optics and biology started with the

development of the microscope by Leeuwenhoek and his incursion into the microscopic world. Nowadays, main experimental techniques in molecular biology, biochemistry and biophysics are related to optics: light microscopy, spectroscopy, flow cytometry, and fluorescence-based methods. Furthermore, other light-based techniques such as optical tweezers have helped to enlarge the strategies to study the macromolecular functioning. Until 20 years ago, all the biological experimental techniques were focused on the behavior of many macromolecules (in bulk) at the same time, producing macroscopic measurements where millions of macromolecules are involved. The power of these bulk techniques has been questionless, but recently optical tweezers and other single-molecule techniques have allowed performing measurements on the mechanisms of individual molecules, providing a new and complementary approach to the bulk perspective of macromolecular functioning[3].

The role of light in biology goes further than just being a convenient probe to perform measurements. On Earth light is a ubiquitous environmental factor, thus life has evolved to respond, to fit and to flourish under the influence of sunlight. The living trait of being able to adapt or respond to environmental cues, such as light, is performed at the molecular level by proteins. Proteins have developed the ability to harvest light, transforming the energy of photons into chemical energy through photosynthesis, or performing the transduction of light cues into the organism, triggering a biological response. Both cases are examples of the effects of light over life and highlight the biological importance of understanding how light-sensitive macromolecules work[4].

Herein I present the three main results obtained during my enrollment at the Doctoral Molecular Biology program at IPICYT. Over this entire dissertation the connection between light and biology is noticeable. First using light as a tool for visualization of biological samples and to perform single molecule assays, and then focusing on fungal blue light photoreceptors and how aggregation can take place among these proteins.

In Chapter 2, I describe how digital imaging processing in bright field microscopy images was implemented to allow the visualization of small objects that lack contrast. We developed Computer enhanced bright field microscopy (CEBFM), allowing us to obtain the point spread function of the microscope, enabling us to perform deconvolution on images of *Escherichia coli* cells, improving the overall image quality of unstained samples. In Chapter 3 the construction of an optical tweezers for single-molecule studies is presented, together with our realization of two standard single-molecule assays, which confirmed that our instrument is fully functional. In Chapter 4 the blue light receptors VIVID and ENVOY from *Neurospora crassa* and *Trichoderma atroviride*, respectively, were characterized *in vitro*. For ENVOY, stable recombinant protein was obtained and the mean lifetime of the photoadduct was measured. For VIVID, the aggregation pathway and factors regulating its aggregation were elucidated in a comprehensive way. In each chapter a proper introduction and a summary of the published results are presented. The detailed protocols and the corresponding front page of the published papers are presented as appendixes.

Chapter 2. Improving the imaging of unstained specimens in bright field microscopy

In late 17th century, when Anton van Leeuwenhoek used a small polished lens to observe for first time the microscopic world inside a drop of water, the world changed forever. Leeuwenhoek was the first person to see and describe unicellular organism such as yeasts and bacteria, and later Robert Hooke extended the catalogue of microscopic objects observed. In 1665 Hooke published *Micrographia*, where he reported the detailed structure of fleas' bodies and the microscopic structure of the cork, calling its pores as "cells" which in fact were plant cells (Figure 2-1). Two centuries later Carl Zeiss, a microscope manufacturer, improved the lenses quality with help of Otto Schott, and with Ernest Abbe they developed a theory of image formation to understand and improve images produced by the microscope[5].

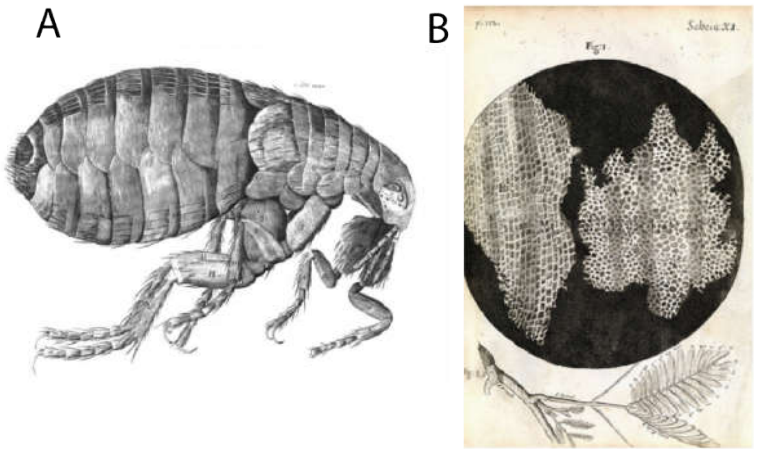

Figure 2-1. Hooke's illustrations published in *Micrographia* in 1665. A) A flea body. B) A sample of cork where plant cells are visible.

Microscopy quickly became a milestone for biology and many different microscopy techniques have been developed to increased image quality and the magnification power. Nowadays, microscopes can be divided in two main kinds: light microscopy and electron microscopy. Electron microscopy is the most powerful microscopy technique allowing the visualization of subcellular structures with resolution in the nanometer scale, with the drawbacks of being incompatible with biological samples in its hydrated state and that laborious processes have to be performed to prepare the samples[6]. Light microscopy, even when it is not (yet!) as powerful as electron microscopy, fits to a wider scope of biological requirements, allowing direct observation even in living samples.

Regarding light microscopy, fluorescent microscopy techniques and the development of engineered fluorescent proteins have enhanced molecular biology research in the last 25 years[7,8]. Currently, super-resolution fluorescent microscopy techniques allow to obtain images of subcellular structures with outstanding definition and lateral resolution ~20 nm[9]. On the other hand, **bright field microscopy (BFM)**, the first and simplest configuration of light microscopes, is still commonly found at biology labs, or coupled to more complex microscopy techniques (e.g. differential interference contrast, dark field, phase contrast, among others) as a way to get a first look of the sample. The biggest limitation for biological applications of BFM is its lack of contrast for thin and transparent samples such as cells. Herein we present a simple way to overcome lack of contrast, allowing the visualization of transparent objects and the improvement of image quality for unstained bacteria.

2.1 Bright field microscopy

Bright field microscopy is the simplest and most widespread light microscopy modality. It consists of a compound microscope formed by an illumination system, a condenser lens, an objective lens, the ocular lens, and the detector. Light from the illumination system is sent by the condenser lens to the sample, where light passes through or interacts with the sample. The outcome light is collected by the objective lens and sent to the ocular lens which provides a second amplification of

the sample and forms the final image in the eye of the observer or in the detection system. The quality of a bright field image relies mainly on the objective lens and in the illumination system. The objective lens is the main contributor to the magnification and resolution of the image, and it is usually formed by several lenses that correct for optical aberrations.

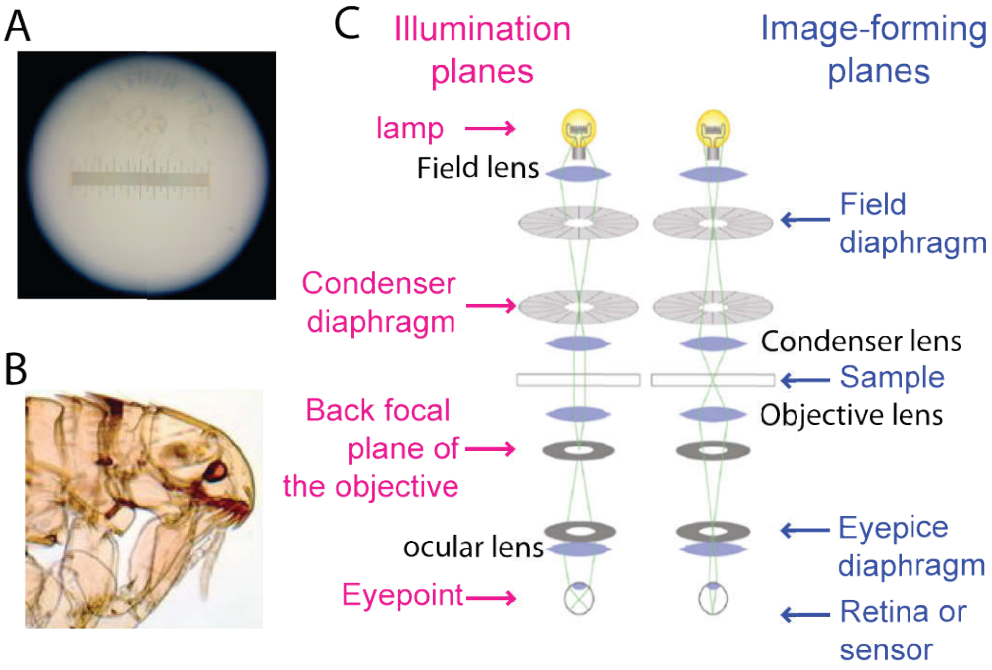

Figure 2-2. Microscope illumination system. A) Micrometric ruler observed under critical illumination. The image of the illumination source, a 60 W lamp, overlaps to the image of the sample. Image taken from reference [11]. B) Flea body observed with bright field microscopy in a Koehler illumination configuration. Image taken from reference [12]. C) Standard bright field microscope configuration under Koehler illumination. Red arrows show the image-forming conjugate planes and blue arrows the illumination conjugated planes.

Regarding the illumination system, one of the first configurations employed was critical illumination or Nelsonian, which forms the image of the illumination source in the sample image. In 1893 to overcome critical illumination deficiencies, August Koehler reported a lenses plus apertures (or diaphragm) configuration that provides an even illumination of the sample plane without the formation of the illumination source image within the sample image. Currently, Koehler illumination is the usual illumination method for BFM, and is achieved through two sets of

conjugate focal planes known as the image-forming conjugate focal planes, and the illumination conjugate focal planes (Figure 2-2)[10].

In Koehler illumination the image of the lamp is formed in the condenser aperture and at the back focal aperture of the objective lens, preventing the overlapping of the lamp and sample images. It is important to notice that since the illumination system is focused in the back focal plane of the condenser, the light will emerge collimated, providing a homogenous field at the sample plane. In an ideal situation when the condenser aperture is almost completely closed the sample is illuminated by a punctual source of light and the contrast in the image sample increases, but resolution is lower.

2.2 Abbe´s theory of image formation in the microscope

In the second part of XIX century Carl Zeiss and Ernest Abbe studied the wave nature of light and the effects exhibited by light when it interacts with matter, such as interference, diffraction, transmission, absorption, reflection, refraction and dispersion. They understood that these common matter-wave interaction effects are responsible for the image formation in a light microscope.

Abbe proposed that for a transmission microscope as BFM, the specimen acts like the overlay of multiple diffraction gratings, where the different details in the specimen correspond to gratings with different spacing between the slits. So the finest details of the specimen correspond to a grating with a smaller spacing between the slits, thus producing diffraction orders with a higher angle (θ) with respect to the normal of the grating (Figure 2-3 A). If the information of the fine details wants to be recorded then the diffracted orders need to be collected and an objective lens with a high numerical aperture is required. More important, Abbe showed that the image is formed by the **interference** of the multiple diffraction orders that emerge from the sample. According to Abbe´s theory the image will be formed only if at least 2 orders of the diffracted light are captured by the objective lens, so they can interfere on the image plane. The greater the numbers of diffracted orders are collected by the objective lens then more accurately the image

will represent the original object. This is why lenses with high NA produced better images.

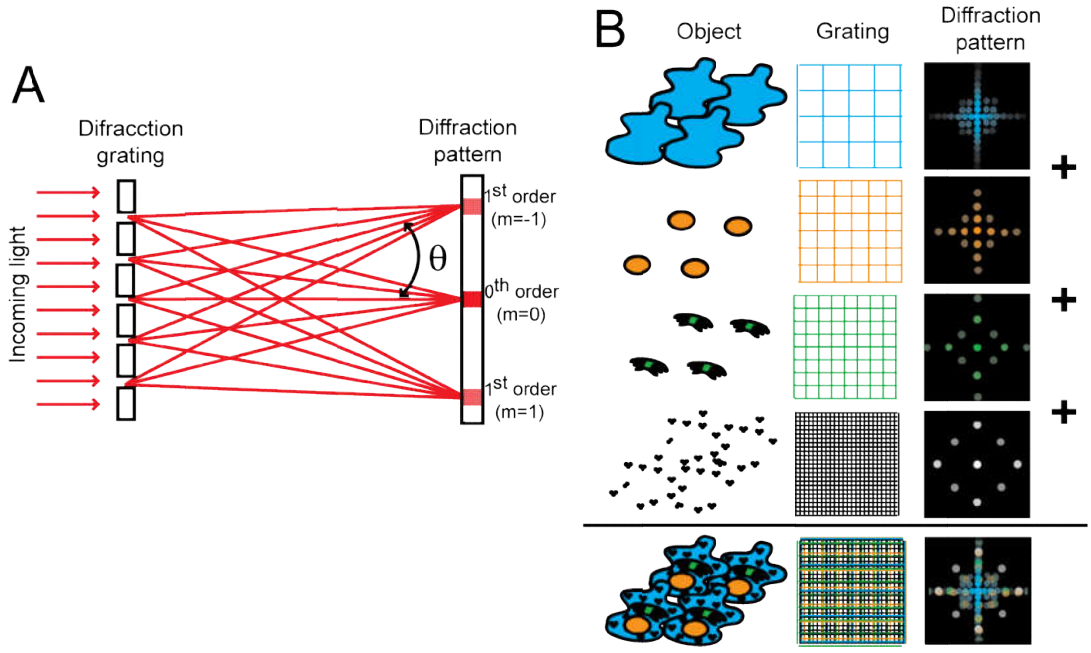

Figure 2-3. Abbe´s theory proposes that a specimen acts like the overlaying of multiple diffraction gratings. A) Light diffracted by a grating. Diffracted orders are separated by and angle θ. B) The specimen acts like the overlaying of multiple diffraction gratings, where each grating corresponds to details in the object with different spatial distribution. Then the object produces a diffraction pattern that corresponds to the merge of the diffraction pattern of each grating.

To prove Abbe's theory that image formation is due to the interference of the diverse diffraction orders, a grille was used as the specimen and a lens was used to form the image of the grille. In the focal plane of the lens a diffraction pattern is formed and, if some orders of the diffracted light are stopped the formed image is modified (Figure 2-4).

It is important to emphasize that when we are observing an image, we are detecting the intensity associated to the electric field of light. However, image forming interference occurs between the electric field of the diffracted (higher orders) and non–diffracted (zero order) light. Therefore, the intensity distribution of light that forms the image is given by

$$I = |E_{\text{non diffracted}} + E_{\text{diffracted}}|^2 , \qquad 1$$

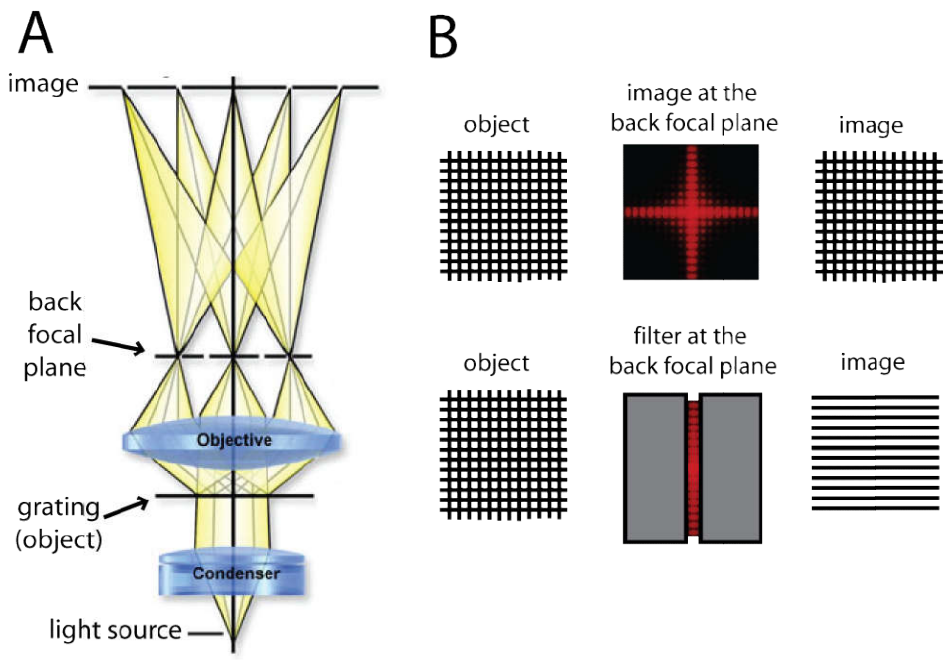

Figure 2-4. Abbe image formation theory. A) The specimen acts like a diffraction grating. The diffracted orders are collected by the lens and are sent to the image plane where they interfere and form the image. Image modified from reference [12]. B) Spatial filtering experiment proves that the final image is due to the interference of the diffracted orders coming from the sample. Image modified from reference[13].

where I is the intensity, $E_{\text{non diffracted}}$ is the electric field of the zero diffraction order of the light and $E_{\text{diffracted}}$ is the electric field of the higher diffraction orders. If the relation presented at Equation1 could be computed, then the image formed by the microscope could be known. For simple objects such as point sources some approximations can be made and a form for the diffracted and non-diffracted electric fields is proposed in this work.

For standard BFM the non-diffracted light corresponds to the unperturbed, transmitted illumination light. For thin and transparent objects the diffraction of light is very small. Thus when thin transparent objects are observed the $E_{\text{non diffracted}}$ term dominates in Equation1 ($E_{\text{non diffracted}} > E_{\text{diffracted}}$) and the object cannot be seen ($I=E^2_{\text{non diffracted}}$). This is the mayor limitation for BFM and digital imaging processing has been used to overcome this limitation[14].

2.3 Computer enhanced bright field microscopy

Computer-based image processing started in 1960´s as part of the NASA's Jet Propulsion Laboratory to support its early unmanned space probes[15]. However, digital imaging processing remained underexploited until standard computers were powerful enough to perform the image processing in a daily fashion. Nowadays, digital imaging processing is used to improve image quality reducing noise, improving contrast, and restoring images among other processes. Digital imaging processing is also used for pattern recognition, with important applications to industrial production lines, military intelligence, and object recognition for blind people[16] among many other applications.

For BFM, we recently introduced a digital image processing method called Computer enhanced bright field microscopy (CEBFM)[14], showing increased contrast and reduced noise, allowing the visualization of thin and transparent unstained objects.

To perform CEBFM, a background (BG) image is first acquired, and then this BG image is subtracted from all the incoming frames. Next, a number (N) of these background-free frames are averaged to get the final image. This simple procedure reduces noise and enhances contrast, allowing the visualization of objects that cannot be observed by simple BFM. CEFBM has been used to visualize small, thin, and transparent objects such as microtubules (MTs), which are filaments of the cellular cytoskeleton of 25 nm in diameter and tens of micrometers long. Figure 2-5 shows how *in vitro* polymerized unstained MTs are clearly visualized after the CEBFM digital image process.

CEBFM has been used to allow the visualization of MTs, but we propose that this method can also improve the quality of bright field image of thin and transparent objects, through a deconvolution process. For deconvolution, the image of a punctual object has to be obtained; before our work, the lack of contrast in BFM had been the major impediment for its acquisition.

The following section summarizes important standard concepts of resolution, point spread function and standard deconvolution in fluorescent microscopy. In section 2.6 we use these concepts to discuss Deconvolution in BFM.

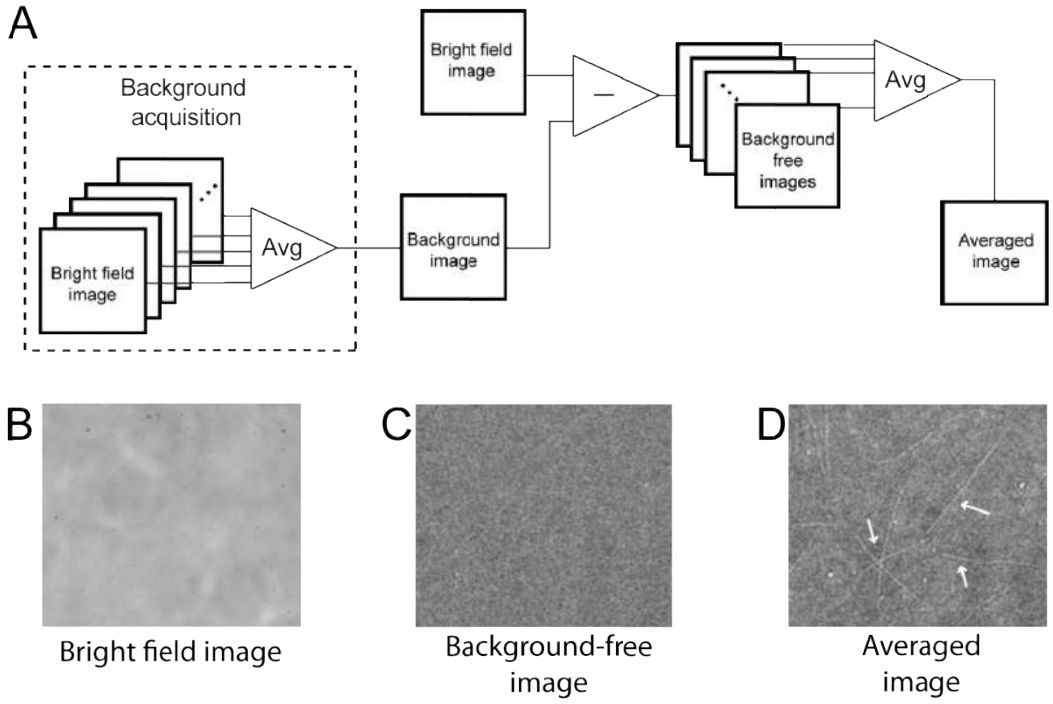

Figure 2-5. CEBFM procedure allows unstained microtubules visualization. A) Schematic representation of the CEBFM procedure. First, frames of a void field of vision are averaged to set the background image. Then the background image is subtracted from all new frames, and the background-free images are averaged to get the final image. B) Standard bright field image of a sample with polymerized MTs attached to the surface. MTs cannot be seen. C) After subtracting the background image the unwanted specks of dust or reflections in lenses are removed. D) After averaging free background images the MTs attached to the coverslip became clearly visible. White arrows indicate some of the MTs visualized in the image.

2.4 Microscope resolution and the Point spread function

The final goal of a microscope is to obtain an enlarged image of a microscopic specimen. If the magnification power of the objective lens increases then the image size increases and we will be able to see more detail in the sample. This is true until the size of the details that we want to observe are comparable with the light wavelength, at which point diffraction effects have to be considered and the

definition of the image cannot be increased even when we increase the magnification. The ability to distinguish small details in the specimen is described by the **resolution** of the microscope. Resolution is defined as the minimum distance between distinguishable objects in an image.

A more precise definition of a microscope resolution is established from the microscope impulse response. When the light from a point object (the impulse) is collected by the objective lens it is diffracted and the formed image is a 3D intensity distribution named **Point Spread Function (PSF)**[13].

For fluorescence microscopy, the point object imaged is a small (below the diffraction limit) fluorophore that acts as a point source of light, resulting in a pattern of concentric rings that corresponds to the Airy function and to the two dimensional (2D) image of the PSF. This pattern of concentric lit and dark rings is due to constructive and destructive interference of light diffracted by the circular apertures in the microscope. The resolution of the microscope will be given by the size of the central spot in the Airy pattern and two point sources will be distinguishable only if they are apart by a distance higher than the radius of the first disk in the Airy pattern (Figure 2-6). This criterion to quantify resolution is known as the Rayleigh criterion:

$$d_{min} = \frac{0.61\,\lambda}{NA_{obj}} \quad , \qquad 2$$

where d_{min} is the minimum distance between two distinguishable particles in the sample, λ is the wavelength of illumination, NA_{obj} is the numerical aperture of the objective lens.

The consequences of diffraction in a microscope are that objects closer than the resolution of the microscope are undistinguishable, so the fine details in the specimen cannot be distinguished, and secondly that all the objects smaller than the resolution limit size will look the same, being its image the PSF of the microscope.

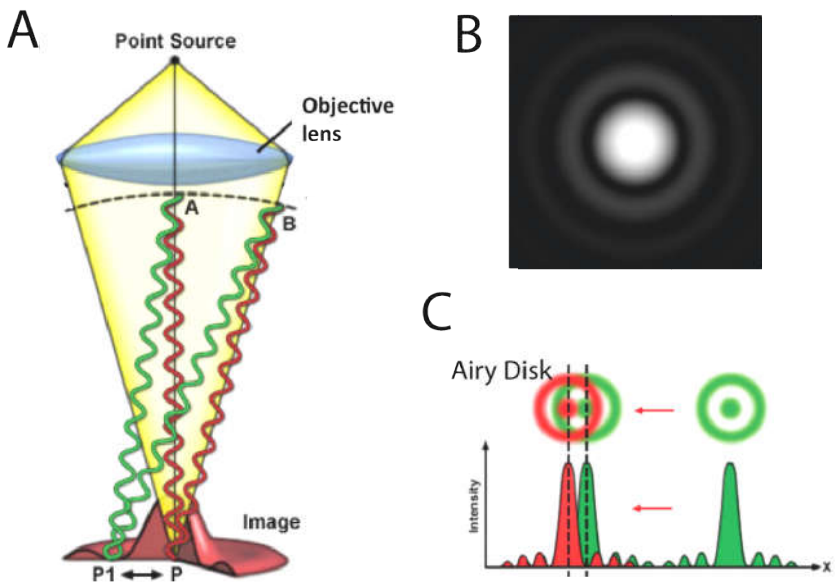

Figure 2-6. Diffraction of a point source forms a pattern of concentric rings in the image and determines microscope resolution. A) Different light beams from a point source travel different distances to reach the image plane, where interference produces dark and lit concentric rings in the image. Light from point A interferes in the image plane with the light coming from point B. At the center of the image (P) the light form A and B have traveled an integer multiple of the light wavelength (λ), thus interfering constructively. For other point in the image as P1 the light form A and B have traveled an integer multiple of $\lambda/2$, thus interfering destructively. B) The interference along all the points in the image plane produces a pattern described by an Airy function. C) Two point objects produce each one its PSF, and the Rayleigh criterion establishes that they will be distinguished only if they are separated by the radius of the first Airy disk. Images were reproduced from reference [17].

The latter is also the cause of fuzziness in images, independently of the microscope quality. A real sample can be thought of as a collection of points, so in the final image each point from the sample will produce a PSF, where the overlapping of all the intensity distributions will blur the image. It is important to note that the overlapping PSF comes from points in the same focal plane or from points in different focal planes. This can be rephrased as

$$\mathrm{image} = \mathrm{object} \otimes \mathrm{PSF}, \qquad 3$$

where the image is the convolution of the ideal object image with the PSF of the microscope. So the image will not represent exactly the object due to effect of

diffraction. However, the image can be restored to represent the original object via a **deconvolution** process.

2.5 Deconvolution in fluorescence microscopy

In cell biology, fluorescence microscopy deconvolution was first introduced in 1983 when Agard and Sedat obtained the first high-resolution images of fluorescently stained chromatin in the nucleous of *Drosophila melanogaster* cells[18], and has been increasingly used since it improves contrast and resolution [19](revealing structures that are barely visible in the raw images) at a level comparable to those images obtained with confocal microscopy[20]. In confocal microscopy the out-of-focus light is eliminated by using small apertures that discriminate between the focal plane and the rest of planes in the sample.

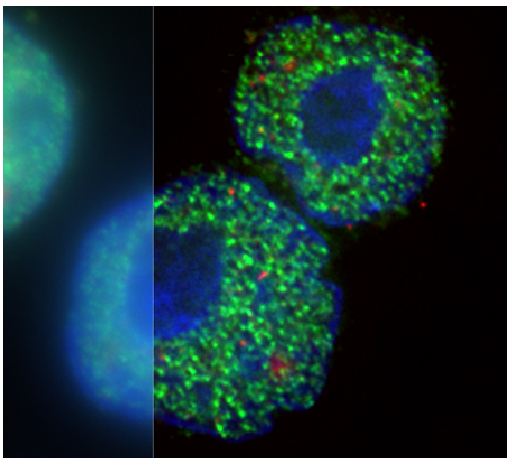

Figure 2-7. Example of image quality improvement by deconvolution in a fluorescence microscopy image. Transcriptional activity in the nucleus. Jill Brown and Veronica Buckle, MRC Molecular Haematology Unit, Weatherall Institute of Molecular Medicine. Deconvolution was performed using Huygens Software. Image reproduced from reference [22]

Meanwhile, wide field microscopes collect light from all planes, blurring the image. In this case, deconvolution processing is an option since it reverses the blurring due to diffraction (Figure 2-7)[21].

To perform a deconvolution processing three requirements are needed: 1) the PSF of the microscope, 2) a *z*-stack of 2D images of the sample, and 3) a deconvolution

algorithm. Since deconvolution in fluorescence microscopy is a widespread technique, methods to obtain the experimental PSF are well standardized. Briefly, a fluorescent bead of size below (~1/3) the resolution limit of the microscope (so it resembles a point object) is immobilized on a coverslip, then the bead is imaged at different axial positions resulting in a stack of 2D images that is the PSF[23]. Then, a stack of 2D images of the sample is acquired (Figure 2-8), in the same fashion than the PSF. Finally a selected deconvolution algorithm must be applied (different options of free software are available on the web). The PSF can be measured for each microscope, but when signal to noise ratio (SNR) is poor analytical methods have been used to compute the PSF[24].

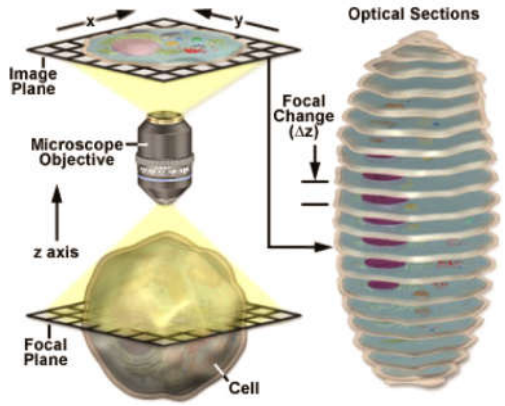

Figure 2-8. Acquisition of optical sections for deconvolution. The sample or the point object (to get the PSF) is moved along the z axis to capture the focused images along the sample volume. It is important to acquire the PSF stack and the sample stack with the same focal change. Image reproduced from reference [17].

Several algorithms to perform deconvolution have been developed, and can be classified in six broad classes: no neighbors methods, neighboring methods, linear methods, nonlinear methods, statistical methods and blind deconvolution methods[25]. Linear methods, as the Wiener filter, are the simplest methods. In these methods, the problem of finding the object is solved in the frequency domain, through a Fourier transformation. Convolution operation turns into multiplication in the Fourier space, thus the object information can be isolated through a simple division.

$$\mathcal{F}(object) = \frac{\mathcal{F}(image)}{\mathcal{F}(PSF)} \qquad 4$$

Where $\mathcal{F}(object)$, $\mathcal{F}(image)$, $\mathcal{F}(PSF)$ are the object, image and PSF in the Fourier space. However, problems to compute the object arise when $\mathcal{F}(PSF)$ is zero. Wiener filter can be used as a first guess of the deconvolved image and then other iterative deconvolution methods can be used[26].

2.6 Deconvolution in Bright field microscopy

Contrary to fluorescence microscopy, the application of deconvolution in bright field microscopy has been scarce. In transmitted optical microscopy, specimens can be ideal absorptive objects, ideal phase objects or more commonly, the specimen is formed by the concurrence of non-ideal phase and amplitude structures. Ideal absorptive objects completely absorb the light that passes through the sample, producing high contrast images. On the other side, ideal phase objects do not absorb light but they induce a phase shift in the light and, unless the phase shift is transformed to an amplitude output (as in phase-contrast microscopy), phase objects lack of contrast.

In transmitted optical microscopy, absorption structure and phase structure of the specimen determine the three-dimensional intensity distribution of the image and, unlike fluorescence, in BF microscopy the PSF is not unique, as it has absorptive and phase components[27]. In BF microscopy the image is formed by the convolution of each component of the PSF with the absorptive and phase structures of the object

$$\mathrm{image} = \mathrm{object_P} \otimes \mathrm{PSF_P} + \mathrm{object_A} \otimes \mathrm{PSF_A}\ , \qquad 5$$

where the image is the convolution of the absorptive structures of the sample ($\mathrm{object_A}$) with the corresponding PSF for ideal absorptive objects ($\mathrm{PSF_A}$), plus the convolution of the phase structures of the sample ($\mathrm{object_P}$) with the corresponding PSF for ideal phase objects ($\mathrm{PSF_P}$).

Standard fluorescence deconvolution algorithms cannot be applied in this case unless one of the components of the image could be neglected. Stained samples

have been used to obtain a purely absorptive object, so the phase component can be neglected and standard fluorescence deconvolution methodologies can be applied [28,29,30]. The opposite case, where only the phase contributions are taken into account, presents the limitation that an ideal phase object lacks contrast so the corresponding PSFp has not been obtained. For biological applications phase objects such as cells are usually observed via staining of the sample or by techniques different from BFM.

Herein we present CEBFM as a digital image process capable to overcome lack of contrast limitation in BFM, allowing the first experimental measurement of the PSFp, and the application of a standard fluorescence deconvolution process in unstained bacterial cells.

2.7 Results

This section summarizes the results published in: **Hernández Candia CN**, Gutiérrez-Medina B (2014) *Direct Imaging of Phase Objects Enables Conventional Deconvolution in Bright Field Light Microscopy*. PLoS ONE 9(2): e89106. doi:10.1371/journal.pone.0089106.

2.7.1 Abstract

Although deconvolution is a powerful method to improve image quality its application to bright field microscopy images has been limited, mainly for the difficulty in assessing the corresponding impulse responses of the microscope. In our lab we have built a bright field microscope fitted with a computer-enhanced bright field microscopy (CEBFM) that affords real-time sample visualization with reduced noise and enhanced contrast, allowing us to present the first direct measurements of the PSFp of a high-aperture microscope operating in bright field. Polystyrene nanoparticles of 100 nm in diameter serve as point objects to acquire the impulse response of the microscope. The measured point-spread function allows us to demonstrate conventional deconvolution in the bright field images of

living, unstained bacteria, showing improved definition of cell boundaries and sub-cellular features.

2.7.2 Motivation

Unlike in fluorescence, in BF microscopy the PSF is not unique, as it has absorptive and phase components[27]. However, standard deconvolution can be used to restore images of pure phase or pure absorptive objects. So if the phase PSF is obtained, a linear deconvolution algorithm could be applied to restore images of phase objects such as unstained cells, increasing image quality by a simple and accessible method to nearly all biological labs.

2.7.3 Main results

We built an inverted microscope, composed by an objective lens (100x, NA=1.3, oil immersion), a condenser lens (NA=0.1) and an illumination system in Koehler configuration with a blue light-emitting diode (LED) as the light source. The microscope was fitted with a *x-y-z* piezoelectric stage which allowed the movement of the sample with a nanometric resolution in a range of up to 100 μm, and images were acquired with a 8-bit charge-coupled device (CCD) camera and transferred to a computer to perform CEBFM processing[31].

To improve CEBFM during background acquisition a total of 250 frames were captured and averaged to produce the background frame that was subtracted from all incoming frames. Background subtraction was optimized by displacing the piezoelectric stage along non-closed paths covering distances of a few micrometers while background frames were taken. Once the background image was acquired 50 background-free frames were arithmetically averaged, increasing the SNR. Background removal and frame averaging were performed in real time allowing the direct visualization of the phase objects. However, frame averaging can be time consuming so final image refreshment presented a delay of tens of seconds. Image acquisition and digital processing was performed using LabView 8.5.

To get the PSFp the same method described for fluorescent microscopy was performed: a 100 nm polystyrene bead was immobilized on a cover slip and to get the PSFp a stack of 2D images was acquired. Each image on the stack corresponds to an average of 50 background-free frames. The stack corresponds to a 4 μm scanning along the *z* direction starting 2 μm below the focal plane and ending 2 μm above the focal plane, taking steps of 50 nm. In BFM images at the focal plane are characterized by a total lack of contrast[32], even with our improved CEBFM. We set the focal plane in our samples as the *z* position where objects became the least visible after being mainly bright and before being mainly dark (Figure 2-9A). The 3D image formed by the stack corresponds to the PSF_P of our bright field microscope (Figure 2-9B).

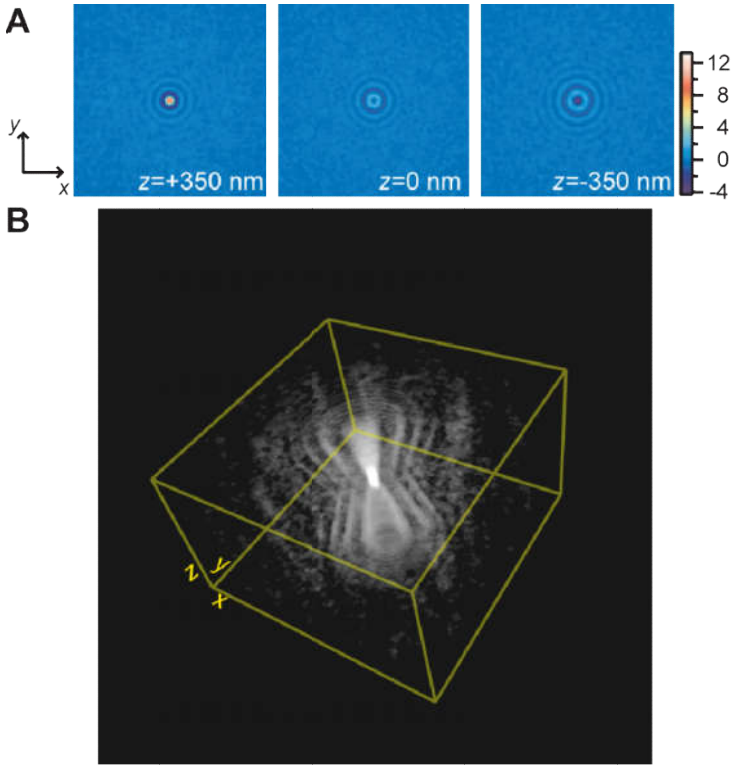

Figure 2-9. Experimental assessment of the PSF_P for a bright field microscope. A) False color, digitally-processed images of 100-nm beads at various axial positions. Color scale represents the pixels intensity after digital imaging processing. B**)** 3D view of the PSF constructed from bead images. Arbitrary transparency and threshold levels were applied for display purposes.

The Bright field PSFp presents important differences with respect to the Fluorescence PSF:

1. In fluorescence microscopy the PSF intensity values are always above the background signal, contrary to the bright field PSFp which presents both positive and negative intensity values (Figure 2-10 B). Even when intensity is a defined positive magnitude (intensity is the squared value of light electric field) here we have negative values due to the subtraction of the background image. In other words, herein having negative intensity values means that the intensity is lower than the background so a destructive interference, according to Abbe's theory of image formation, is taking place. Conversely, having a positive value of the intensity means that constructive interference is occurring.
2. The PSFp is symmetric along the *z* axis (Figure 2-10 C), presenting positive intensity values above the focal plane and negative intensity values below the focal plane, and becoming zero at the middle, which corresponds to the fact that thin phase objects are invisible at the focus[32].
3. The 2D lateral images of the PSFp do not fit an Airy function as in fluorescence microscopy (Figure 2-10 B). The Airy function is always positive, contrary to the plot profiles of the axial images of bright field PSFp.

To fit our experimental results we proposed a model for the PSFp based of Abbe's image formation theory (Equation 1). Since the intensity of the non-diffracted light (illumination light) is removed by background subtraction, and the intensity of the light diffracted by small thin objects is small, the most important contribution for the formation of CEBFM images is the interference term ($2Re[E_{diffracted}E_{non\text{-}diffracted}]$). This is important because interference translates changes in phase into changes in intensity, thus we can detect phase objects. Noticeable our proposed model for the PSFp was in a good agreement with our measured PSFp (Figure 2-10 D,E,F).

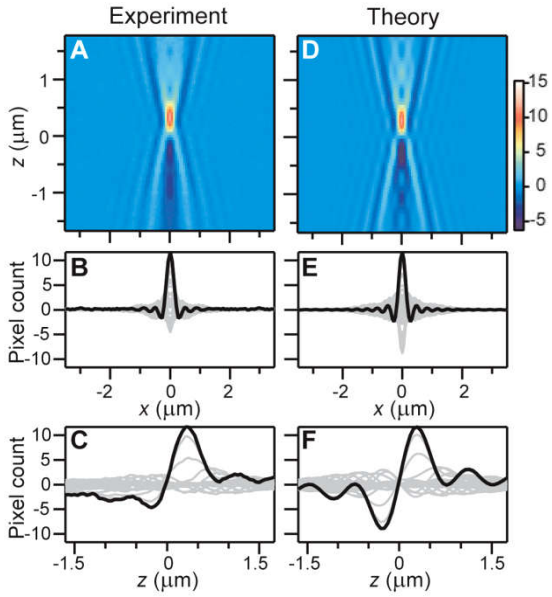

Figure 2-10. Main characteristics of the PSF and comparison with theory. (A) False-color, vertical slice (y=0) of the experimental PSF. (B) Superimposed lateral cross-section profiles (light gray). Color scale represents the pixels intensity after digital imaging processing. (C) Axial cross-section profiles. (D) Vertical slice (y=0) of the theoretical PSF. (E) Lateral cross-section profiles. (F) Axial cross-section profiles. The intensity of the theoretical model was multiplied by an arbitrary factor for comparison with experiment. Profiles highlighted in black correspond to the maximum positive intensity peak of the PSF, used to determine the PSF main spot size

Once the PSF of our microscope was obtained, the deconvolution process was performed on bright field images of *Escherichia coli* cells. First, *E. coli* cells were deposited on a coverslip and allowed for sedimentation. After that, bright field images at different axial positions were acquired resulting in a stack of 2D images. A 3D deconvolution algorithm that computes non-negative, iterative deconvolution was performed on the image stack using the ImageJ free plugin "Iterative Deconvolve 3D"[26].

The deconvolved frames show significant improvement in clarity (Figure 2-11 A and B), in particular, cell wall boundaries become well defined, displaying a striking resemblance to fluorescence microscopy images[33]. Likewise, intensity variations along the cell body that are only hinted in the original BF frames gains contrast after deconvolution. Some of these variations show a degree of spatial periodicity

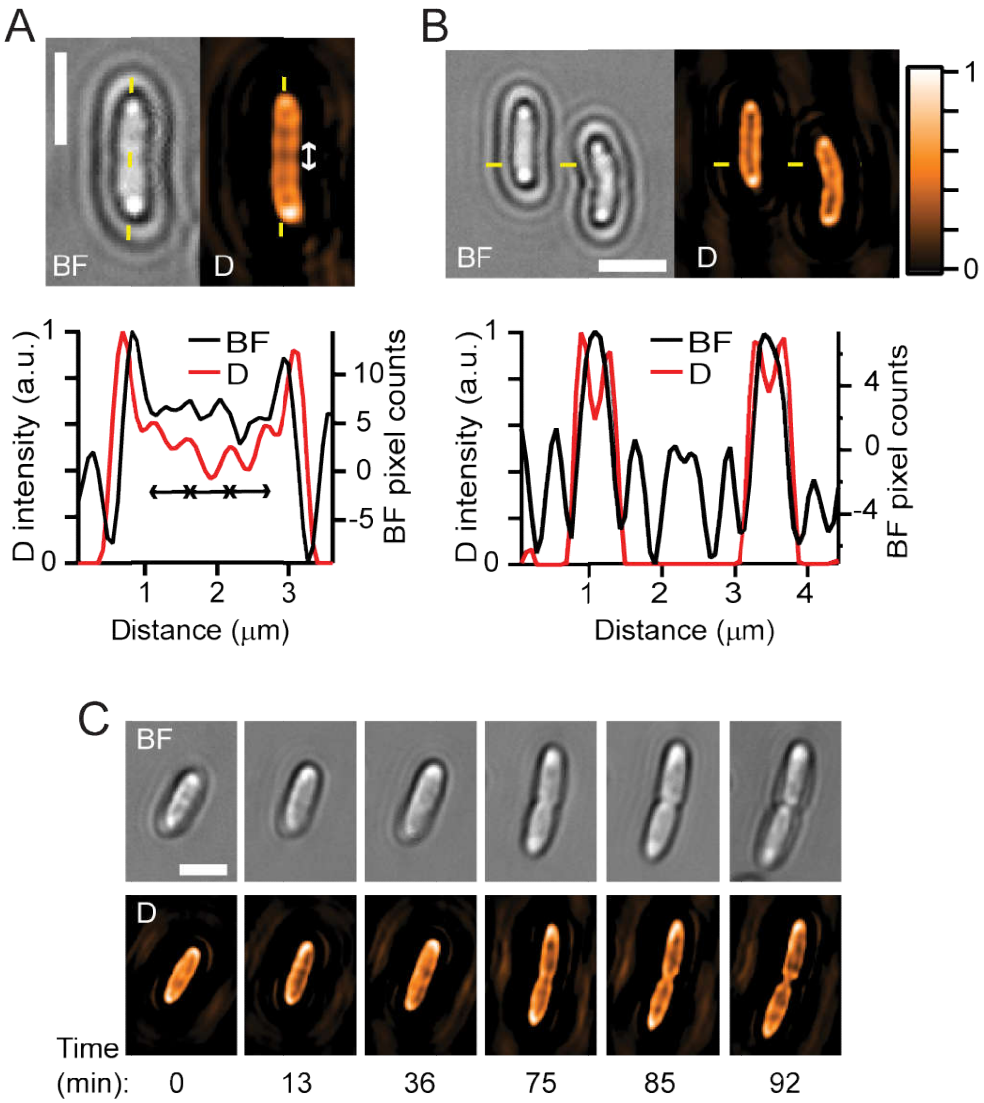

Figure 2-11. Demonstration of deconvolution in the BFM images of unstained, living E. coli cells. A-B) Bright field images of bacteria before (BF) and after deconvolution (D), together with their respective intensity profiles along the yellow dashed lines, show cell boundaries becoming better defined, with periodic variations in intensity revealed (A, double-arrow lines: 0:5 μm), C)Time-lapse frames of a bacterium undergoing cell division under continuous illumination. Scale bars: 2μm.

(~0.5 μm) and may correspond to the same structures observed recently in unstained bacteria using dSLIT, a microscopy technique capable of quantitative phase imaging[34]. It could be speculated that this periodic subcellular structure corresponds to the MreB proteins, which are homologous to actin proteins and as actin, polymerase to form filaments. The MreB filaments have been proposed to

work as a cytoskeleton in prokaryotic cells[35,36], and are required for the maintenance of the rod-shaped of the bacteria and has been shown to form spirals that travel along the longitudinal axis of *E. coli* cells.

One attractive feature of BFM deconvolution is the potential to observe unstained specimens over extended periods of time. We show this aspect by following changes in *E. coil* shape as cell division proceeds under continuous illumination (Figure 2-11 C).

2.7.1 Novel contribution

CEBFM was improved by acquiring a better background image. For this, the piezoelectric stage that supports the sample was moved meanwhile bright field frames used to set the background image were acquired. Improved CEBFM was used to perform the first experimental assessment of the phase point-spread function in BFM. The measured PSFp allows us to apply already developed deconvolution algorithms on the bright field images of living, unstained *Escherichia coli* cells, making possible the extension of standard deconvolution processing beyond fluorescence microscopy. In addition, we were able to integrate the same digital imaging processing technique to an optical tweezers setup designed to perform single-molecule experiments (see Chapter 3).

2.7.2 Conclusions

The results presented here introduce practical methodologies in BF microscopy to directly measure the corresponding phase point spread function, from where conventional deconvolution processing is demonstrated. Our procedures are applicable to the imaging of thin, transparent specimens such as living, unstained cells.

2.7.3 Unpublished data

The CEBFM capabilities proved to be effective to observe MTs (Figure 2-5) and 100 nm diameter beads (Figure 2-9). However, we asked ourselves if smaller object such as 40-nm diameter beads or viruses can be detected.

First, we tried to visualize 40 nm diameter beads and since a low SNR was expected, fluorescent polystyrene beads were used to assure that the bright field images correspond to the 40-nm beads and not to undetermined sub-diffraction particles in the sample. Scanning electron microscopy (SEM) images were used to measure the distribution size of the beads and to standardize the conditions to get a homogenous and disperse sample (Figure 2-12A and B). Fluorescence microscopy was coupled to our bright field microscope and the image fields of view for both microscopy methods were matched. Dispersed 40-nm beads were attached to a clean coverslip and the CEBFM image was compared with the fluorescent image. Preliminary results show that averaging 100 background-free images, the 40-nm diameter beads can be detected. However, its contrast was not good enough to acquire the PSF (Figure 2-12C). One important concern was the detection of a single bead instead of bead clusters that remained in a sub-diffraction size. Several attempts were made to correlate the field of view of the bright field microscope with an image acquired by electron microscopy. As a first try, beads of 1.8 μm in diameter and beads of 500 nm in diameter were mixed and light microscopy images were correlated with electron microscopy images using recognizable beads patterns (Figure 2-12D). However this procedure turns to be extremely inefficient and only once I succeed in matching light and electron microscopy images, so a more reproducible method is needed.

As an alternative, the fluorescence intensity of the spots produced by the sub-diffraction dispersed beads was plotted into a histogram. Fluorescence intensity was distributed in an approximated multimodal distribution (Figure 2-12E), and assuming that each bead presents the same fluorescence intensity then, it was

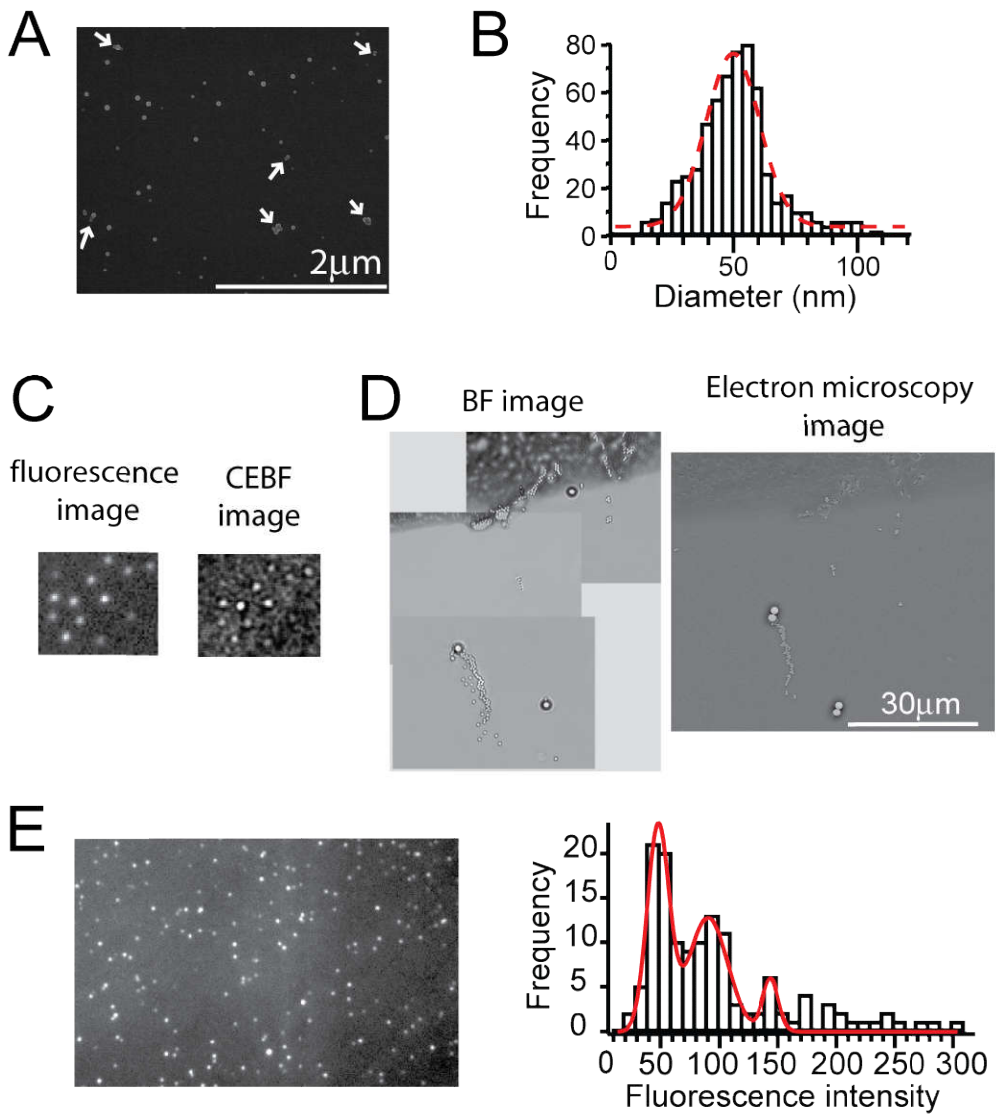

Figure 2-12. Visualization of 40-nm diameter beads. A) SEM images of 40 nm diameter beads covered with a thin gold layer. Beads were dispersed, and were mainly single beads. Dimers and trimers were also founded (white arrows). B) Bead size distribution was obtained from SEM images. Bead size was 47.9±15 nm, where the diameter increment due to the gold layer was included. C) Fluorescence microscopy images of the 40 nm beads were compared with the CEBFM images. In both images the same pattern of beads can be observed. D) The same fields of view in bright field microscopy were found in SEM. E) Measuring fluorescence intensity of each bead (left) on a large sample allowed us to obtain the intensity distribution (right) which was well fitted by a multimodal function that suggests that monomer, dimer and trimers of beads are formed in the sample.

concluded that the beads were distributed mainly as single beads, but dimers and trimers were also present in the sample. However, this has to be corroborated by an independent method.

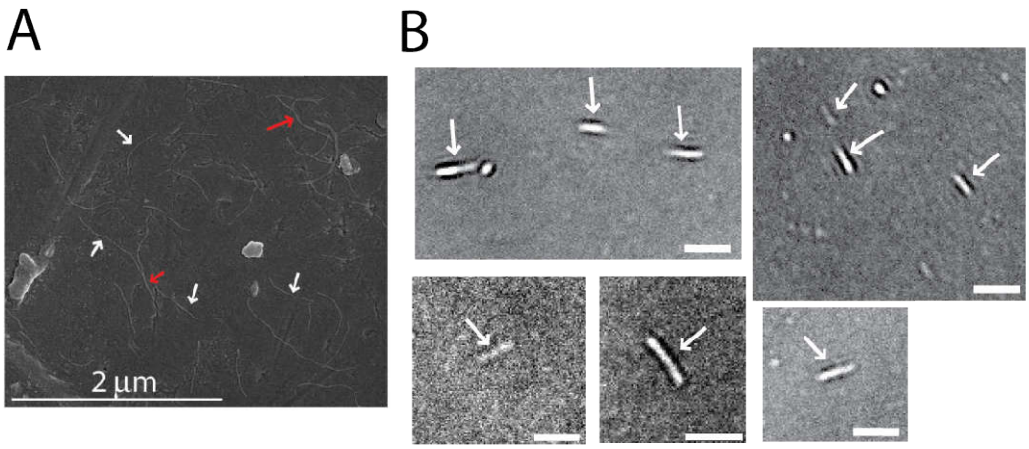

Figure 2-13. Visualization of PRSV by CEBFM and SEM. A) SEM of PRSV diluted in miliQ water and covered with a thin layer of gold. Single virus (white arrows) and bundles of virus (red arrows) were observed. B) Images of some possible virus observed with CEBFM (white arrows). Bars represent 2 μm.

We also tested if viruses can be observed with CEBFM. Usually viruses are detected through electron microscopy, implying expensive and time consuming experiments. We thought that CEBFM can be used as a first inexpensive and fast test to confirm virus presence. As a proof of concept, the Papaya ringspot virus (PRSV) (kindly provided by Dra. Selene Aguilera Aguirre from CINVESTAV-Guanajuato) was visualized with CEBFM. PRSV viruses are rod-shaped with 12 nm in diameter and between 760-800 nm long[37]. First, we tested different buffer compositions (PBS, $MgCl_2$ buffer 0.01M and 0.25M, MiliQ water) to obtain a disperse sample, and SEM was performed to verify virus presence, sizes and homogeneity in the sample. Water turns out to be the best buffer conditions to increase the amount of individual virus in the sample (Figure 2-13A). Once we confirmed the presence of dispersed PRSV into the sample, PRSV were observed with CEBFM. By averaging 100 background-free images a small but detectable signal was produced (Figure 2-13B). Further work to confirm that the observed signal corresponds to a single virus must be performed: first tagging the virus

capsid with a fluorescent probe and secondly by correlation of the bright field image with TEM to corroborate that we are detecting single virus, and not bundles of viral particles.

2.8 Future work

We proved that standard deconvolution of bright field images provide a define boundary of the cells, but it is not clear if this boundary matches the cell membrane. If we prove that BFM deconvolution actually presents the real boundary of the cell, then this simple method can be used to perform quantitative studies over cell shape and colony grow over extended periods of time without the toxic effects and photo bleaching effects of fluorescence probes. For this, the cell membrane has to be tagged with a specific florescence probe and fluorescence microscopy images have to be compared with bright field images after deconvolution.

CEFBM proved to be a simple and inexpensive method for the detection of small nanometric objects, but to determine if CEBFM can be used to detect the presence of single viruses or transparent particles below the 100 nm diameter further work has to be performed.

Chapter 3. Optical tweezers for single-molecule assays

Experimental biology relies on laboratory methods that allow having reproducible and quantitative measurements. The selected methods or instruments will depend on the questions that want to be answered. For us, an instrument that allows *in vitro* **single-molecule** measurements of forces and displacements in real time was required to follow the dynamics of molecular motors (which convert chemical energy into mechanical work), DNA-protein interactions, and the conformational change of proteins. From the wide number of single-molecule techniques, we decided to work with a laser-based methodology known as optical tweezers, this technique allows us to measure displacements and forces on the correct expected scales (10^{-9} m and 10^{-12} N, respectively) and can provide a direct mechanical characterization of molecular behavior.

3.1 Single-molecule Techniques

Single-molecule techniques are based on methods that allow studying one molecule at the time and have become a powerful complementary approach to standard bulk measurements. Single-molecule approach allows following the dynamic of molecules for periods of time larger than milliseconds which bulk methods cannot since it is not possible to keep an ensemble synchronized due to the stochastic nature of the system[3].

For bulk methods only the average trajectory of the population can be known, masking rare but potentially important molecular trajectories. On the other hand, single-molecule techniques can follow the real-time trajectories of individual molecules and, upon observing very many of them, a histogram of the dynamical properties over the population could be constructed avoiding the loss of less

represented trajectories[38]. Cases where molecules can populate more than one state can also get benefited from a single-molecule approach. In bulk methods the measured property correspond to the average of that property over the ensemble, meanwhile in single-molecule methods the multimodal nature of the distribution of states can be recovered from an histogram of any property measured one molecule at the time[3].

Single-molecule methods have directly measured important mechanism previously established by standard bulk methods[39] and have brought a way to elucidating reaction mechanisms[38]. Single-molecule experiments have become a key stone to understand molecular motors[40], the spatial and temporal distribution of molecules within a cell with an outstanding resolution[41,42], and the energy landscape during folding of macromolecules[43].

An inconvenience of single-molecule techniques is the technical challenge of measuring the signal produced by just one molecule with enough signal to noise ratio (SNR). Techniques developed for single-molecule experiments can be divided in force spectroscopy methods and fluorescence methods. Force spectroscopy methods include atomic force microscopy (AFM), **optical tweezers** and magnetic tweezers[44]. Single-molecule fluorescence methods include Förster resonance energy transfer (FRET)[45], photo-activated localization microscopy (PALM)[46], stochastic optical reconstruction microscopy (STORM)[47], and stimulated emission depletion (STED)[48]. Optical tweezers was our choice to perform force spectroscopy measurements due to the scale of forces (pN) and displacements (nm) that optical tweezers allows to measure.

3.2 Optical Tweezers

An optical tweezers (or optical trap) consists of a laser beam that is tightly focused by a high numerical aperture microscope objective, so all optical tweezers setups are basically an adapted standard bright field microscope. The focused laser beam is capable of trapping micrometer-sized objects in 3D, and can also be used for the transduction of displacements and forces.

The history of optical tweezers started in 1970 when Arthur Ashkin reported that micro-sized particles were accelerated and trapped using only the force of radiation pressure from a laser beam[49]. One year later, using the force of radiation pressure, Ashkin made glass spheres particle levitate, equilibrating the attractive gravitational force over the glass bead with the force of radiation pressure exerted in the opposite direction by the laser beam[50]. In 1986 Ashkin reported, for the first time, the trapping of dielectric beads suspended in water by a single tightly focused laser beam, in other words he reported the first optical tweezers[51].

The physical principle behind optical trapping is the conservation of total momentum. Light carries a linear momentum that is in the direction of the propagation of light and is proportional to light's energy. This is the reason why light can exert forces over microscopic objects. When light interacts with a non-absorbing object, it can be reflected or refracted, changing its linear momentum, and since total momentum is conserved, the object recoils in the opposite direction[52]. If a proper profile of light as a tightly laser beam is used, then the momentum transferred by the light will confine the microscopic object spatially.

When the trapping beam has a Gaussian profile, it turns out that the force exerted by optical tweezers over a trapped object is a restitution force proportional to displacements F_{trap}=-kx, where F_{trap} is force, k is known as the stiffness of the trap, and x is the displacement of the trapped object from its equilibrium position (x_0)[53] (Figure 3-1). This behavior is analogous to a spring characterized by Hooke's Law. In optical tweezers, displacement in any direction produces a restitution force in the opposite direction with its corresponding stiffness constant, performing stable trapping in 3D.

The laser propagating direction is referred to as the *z* coordinate and its orthogonal plane is formed by the *x,y* coordinates. The displacements along any direction (*x,y,z*) and the corresponding stiffness of the trap (k_x, k_y, k_z) can be measured by well-established methods summarized in next sections.

The capability to manipulate micron-sized objects and exert forces and measure displacements (in the order of 10^{-12} N and 10^{-9} m, respectively) opened the door to

new thrilling experimental possibilities. In the biological context, optical tweezers has been used to learn about central cellular processes such as transcription[54], translation[55], DNA wrapping at nucleosomes[56], and intracellular transport performed by molecular motors[57] among other important processes. Optical tweezers allows to measure directly the forces involved in these processes, or to directly apply an external force to alter them and underlay their molecular mechanisms[58].

3.3 General considerations for single-molecule assays using optical tweezers.

Direct use of optical tweezers to manipulate bio-molecules as proteins is not possible since the trapping efficiency drops off with the radius of the trapped object[59], so the small size of proteins becomes a limitation. To overcome this situation micro-beads (usually of 0.4-0.6 μm in diameter) are used as handles to manipulate the molecule under study, and the particular configuration will depend on the experimental needs. Figure 3-1 shows the most used experimental configurations for single-molecule measurements using optical tweezers.

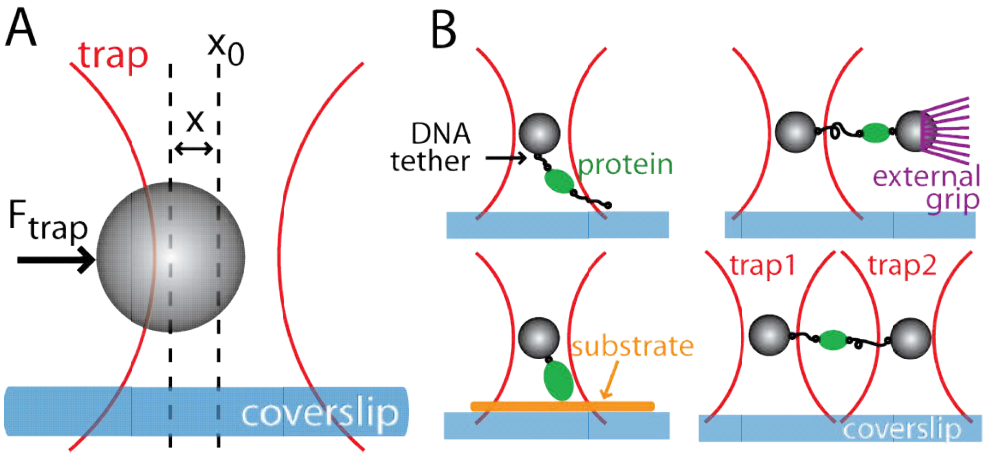

Figure 3-1. Optical tweezers trapping principle and common assay configurations. A tightly focus laser beam bring micrometric objects to an equilibrium position (x_0) at the center of the trap. Any displacement (x) induces a force (F_{trap}) that brings the object back to x_0. B) Four standard configurations to perform single-molecules assays. Hypothetical proteins are represented as ovals, fragments of DNA are used to tether proteins to the beads used as handles.

Regarding to the laser beam, it is important to have a laser that supplies a stable power to avoid force fluctuations, an excellent pointing stability to avoid unwanted displacements, a Gaussian mode to tightly focuses the beam and performs stable trapping along the *x,y* plane, and for biological applications, an infrared (IR) wavelength is preferred to diminish light toxicity[53,60].

To build a functional optical tweezers it is necessary to have an objective lens and a condenser lens with high numerical apertures (NA), the trapping laser beam, a method to visualize the sample, a method to detect the position of the trapped bead, and a piezoelectric stage to hold the sample. All these requirements are fulfilled by an inverted bright field microscope modified to couple the trapping laser beam and the position detection method.

A sensitive position detection method and its proper calibration are the most important differences between an optical tweezers that can be used to perform force and displacement measurements and those that can only be used to trap.

3.4 Trapped bead position detection

The position of a trapped bead can be determined by video microscopy, although this is a simple method, it is limited by the speed of the camera and depends on the efficiency to track the bead position. As an alternative, the trapping laser can also be used to track the bead position, since the bead acts as a lens inducing small deflections into the laser whenever the bead is moved apart from its equilibrium position (x_0). Those deflections can be detected by a position-sensitive detector (PSD) placed in a plane conjugated to the Back Focal Plane (BFP) of the condenser lens. This BFP detection method is only sensitive to relative displacements of the bead from its equilibrium position (x_0, y_0, z_0).

When the trap bead is displaced from the equilibrium position along the *x,y* plane, the laser is deflected, reaching a different place at the PSD. When the bead is displaced along *z,* the divergence of the laser beam is modified. A diaphragm (D1) placed in front of the PSD limits the size of the spot that reaches the detector, making the total intensity that reaches the PSD a function of the position of the trapped bead along *z* direction (Figure 3-2).

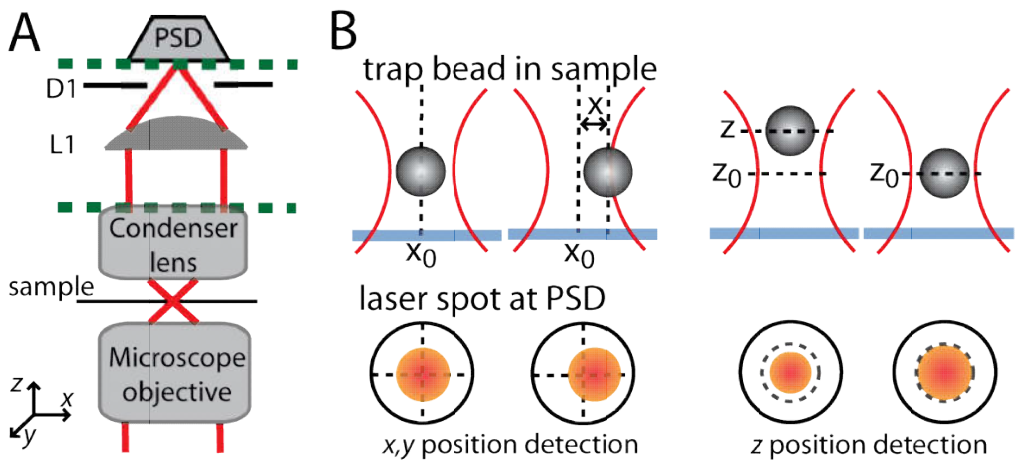

Figure 3-2. Basic elements of a BFP detection method. A) To make that the BFP of the condenser and the PSD become conjugated planes (dash line) the lens (L1) is used. A diaphragm (D1) is used to make the PSD sensitive to changes along the *z* coordinate. B) Displacements (x) of the bead along *x,y* coordinates produce a deflection in the laser that can be detected by the PSD. Displacements along the *z* direction modify the size of the spot that passes through D1 and reaches the PSD detector.

A calibration factor to convert the PSD output voltage signal into a displacement measurement can be obtained from additional information obtained during trap stiffness calibration or by using a piezoelectric stage with nanometric resolution as a standard pattern. To get the calibration factor using a piezoelectric stage, a bead attached to a coverslip is displaced by the stage meanwhile the PSD output signal is recorded. For displacements around the equilibrium position (x_0, y_0, z_0), the PSD output signal and the displacements of the bead follow a linear relation, where the slope is the calibration factor. For each coordinate *(x, y, z)* the specific calibration factor has to be obtained.

Once the PSD is calibrated and the displacements of a trapped bead can be measured, the stiffness of the trap (k) can be obtained and, therefore using Hooke's relation (F=-kx), the force exerted into the trapped object can be determined.

3.5 Methods to measure the stiffness of an optical tweezers

Important aspects to be considered to determine the stiffness of a trap (k) is that the stiffness value depends on the size of the bead, the intensity of the trapping beam, the temperature of the sample, and the viscosity of the sample buffer. Thus it is important to control the trapping laser power stability and perform the stiffness calibration under the same experimental conditions than the molecular assay. For single-molecule assay with macromolecules, the standard temperature condition is usually 25°C and the buffer composition is mainly water (with a viscosity at 25°C of 0.89 mPa s). In the following pages three standard methods to obtain the stiffness of an optical tweezers are summarized.

Navier Stokes

A spherical particle exposed to a constant laminar flow feels a drag force given by the Stokes' law. If a bead trapped by the optical tweezers is exposed to a constant flow then the bead will reach a new equilibrium position where the force of the trap equilibrates the drag force. At the equilibrium condition, both forces can be matched:

$$F_{stokes} = 6\pi\varphi r v = F_{trap} = k_{trap} x\,, \qquad 6$$

where r is the radius of the bead, φ the viscosity of the fluid, v the velocity of the flow, x the new equilibrium position of the trapped bead, and k_{trap} is the stiffness of the trap. The stiffness of the trap can be obtained as the slope of the linear relation between the final equilibrium positions of the trapped bead as a function of the velocities of the flow.

Power spectrum

For a bead trapped in an optical tweezers, its motion is not completely restricted. Even when the bead is confined to a certain volume, the bead presents a motion that depends on the force of the trap, the friction force given by the Stokes' law, and the thermal force due to the collisions of the surrounding particles with the trapped bead (Brownian motion). So the confined movement of the trapped bead depends on Stokes's constant, temperature, and the stiffness of the trap.

Given a set temperature, viscosity and bead size, the stiffness of the trap is the only parameter that determines which positions can be explored by the trapped bead. This relationship between the positions explored by the trapped bead and the stiffness of the trap is best appreciated by plotting the positions' Fourier power spectrum. As the stiffness increases, high frequency components start to dominate the movement of the object and the bead is confined to a smaller volume.

The positions power spectrum of a trapped bead can be fitted to a Lorentzian profile from where cut-off frequency (f_0) is obtained as a fitting parameter that is directly related to the stiffness of the trap

$$k_{trap} = 2\pi\gamma f_0, \qquad 7$$

where γ is the drag coefficient $\gamma = 6\pi\varphi r$. Typically, the characteristic frequencies of motion for atrapped bead go up to several kHz, so a detector bandwidth of at least 10-100 kHz is generally used.

Equipartition theorem

In general, for small displacements (x) from the equilibrium position (x_0), the optical trap is considered to be a harmonic potential, which means that trapped bead experiences a Hookean restoring force ($F = -k_{trap}x$) and its harmonic potential energy is given by:

$$U = \tfrac{1}{2} k_{trap} x^2 \qquad 8$$

The equipartition theorem establishes that the thermal bath provides the same energy to all the components of motion that present a quadratic dependence on its potential energy, for a trapped bead this means:

$$k_{trap}\langle x^2\rangle = k_B T \qquad 9$$

Where $\langle x^2\rangle$ is the variance of the position of a trapped bead and k_{trap} is the stiffness of the trap, k_B is the Boltzmann constant, and T is the temperature. It is important to note that this method does not depend explicitly on drag coefficient (γ), so the viscosity (φ) of the fluid and the size of the bead do not need to be known.

Once the stiffness of the trap and the displacements detection method is calibrated, optical tweezers can be used to perform single-molecule studies to

learn about mechanical properties of diverse macromolecules. Herein, stretching of a single DNA molecule and the measurement of the stepping of one kinesin molecular motor along a MT are performed to corroborate the correct functioning of our built optical tweezers system. These two standard single-molecule assays have also provided important information regarding the elastic properties of DNA and the functioning of kinesin proteins. Section 3.6 highlights the importance of the DNA elasticity properties and section 3.7 summarizes the current knowledge of kinesin mechanism functioning.

3.6 DNA stretching

In the last 25 years the elastic properties of DNA have been explored by force spectroscopy single-molecule techniques, allowing the direct measurement of the force/extension profile of a single DNA molecule. Single-molecule stretching of DNA (dsDNA) has been performed using magnetic beads[61], AFM[62], and also using optical tweezers[63,64].

DNA is a biopolymer composed by repeated subunits of nucleotides that presents unique polymer qualities. It is strongly charged due to its phosphate backbone and its characteristic base stacking provides DNA with an unusual stiffness, taking ~50 times more energy to bend a double-stranded DNA (dsDNA) molecule into a circle than to perform the same operation on single stranded DNA (ssDNA)[65]. Also, elasticity of DNA has been proved to depend on the nucleotide sequence[66,67] and on the buffer ionic strength[68].

These unusual elastic properties have diverse effects over the DNA-protein interactions. It has been proved that the bending of DNA can modify the affinity of a transcription factor for its DNA recognition sequence, making DNA elasticity an important factor in the control of transcription[69]. Also, DNA is often bent when complexed with proteins, and during cell division DNA gets tightly packed wrapping around histone proteins, arising one central question: How DNA stiffness and electrostatic repulsion effects are overcome by proteins? It was proved that proteins with cationic surfaces can induce substantial DNA bending toward the bound protein by neutralizing the phosphate groups on one face of the DNA

molecule[70]. These examples highlight the necessity of a profound understanding of the DNA physical properties to fully understand life molecular processes. In this regard DNA has been modeled as a polymer chain and different models have been proposed to fit DNA elastic properties.

Polymers can be described as a continuous line that bends smoothly, like a worm. The inextensible worm-like chain (WLC) model, characterizes polymer elasticity using a single parameter, the persistence length (L_p). Persistence length measures the tendency of a uniform, flexible polymer to point in the same direction under thermal fluctuations; the stiffer the chain, the longer the persistence length.

Also a polymer can be represented by a chain of inextensible fragments of length (*l*), where each fragment has an independent orientation. In this inextensible freely jointed chain (FJC) model the fragment length *l* is known as Kuhn length and it is a measure of the chain stiffness. Each fragment in the chain can freely be oriented at any direction, but the chain tends to be in a configuration with its ends closer. When the chain ends are forced into a configuration with its ends farther apart, an entropic force returns the chain into its initial configuration. The emergence of this entropic force can be understood as a thermodynamic consequence. For a flexible but inextensible polymer chain, there is only one configuration where the distance between its ends is equal to the total length or contour length (L_o) of the polymer (when all its fragments point in the same direction). Furthermore, the number of possible configurations increases as the distance between ends decreases (Figure 3-3A). The second law of thermodynamics establishes that in a closed system entropy increases, this means that the system tends to a macroscopic state where the maximum numbers of microscopic configurations are possible.

Thus for DNA a compact configuration instead of an extended configuration is favored and an external force has to be applied to beat the entropic force. If the external force equals the entropic force, then the DNA molecule can be totally aligned and its end-to-end distance is the contour length (L_o) of the molecule. For an inextensible molecule its L_o cannot be increased, no matter the amount of force applied, but DNA is not an inextensible molecule.

When an extensible polymer is pulled farther its L_o, the polymer resists the stretching with an enthalpic force characterized by its elastic modulus K_0. For dsDNA when stretching forces between 5-50 pN are applied, chemical bonds are slightly modified by the strong stretching, leading to a small linear increase in the length of the molecule[71]. dsDNA stretching assays have been performed by applying wide range forces, from 0.01 pN using magnetic tweezers[61] to forces up to 150 pN using AFM microscopy and two transitions have been reported. The first transition occurred at a longitudinal stress force of 65 pN, where the distance between per base pair (bp) increased from 3.8 Å to 5.8 Å, overstretching the dsDNA[64] (Figure 3-3B). The second transition occurred at forces of 150 pN where the dsDNA turns into single strand DNA (ssDNA)[72]. For forces below 65 pN, four models have been proposed to fit the dsDNA force/extension curves (Figure 3-3C). Each of these models is best fitted to experimental data under different regimes of applied forces, where the entropic and/or enthalpic contributions to dsDNA elasticity have to be considered.

Notably dsDNA is a charge polymer and its own electrostatic repulsion increases its stiffness. Ionic charges can screen DNA charge, making that the Lp depends on the ionic strength. The persistence lengths of a dsDNA molecule can go from 53 nm in a 10 mM Na^+ buffer[73] to 15 nm in a 80 mM Na^+ buffer[74]. At physiological conditions the dsDNA Lp is around 50 nm, implying that a fragment smaller than 50 nm, for example a fragment of 100 bp, will not bend by thermal fluctuation at room temperature. In other words, a 100 bp dsDNA fragment is rigid and to bend it, mechanical work has to be performed.

Elasticity of other important biopolymers as actin and MTs, have been measured. For actin the Lp is 17μm and for MTs the Lp is 5200 μm[75]. Even when MTs presents the highest Lp value, dsDNA is considered one of the most rigid polymers proportionally to its size.

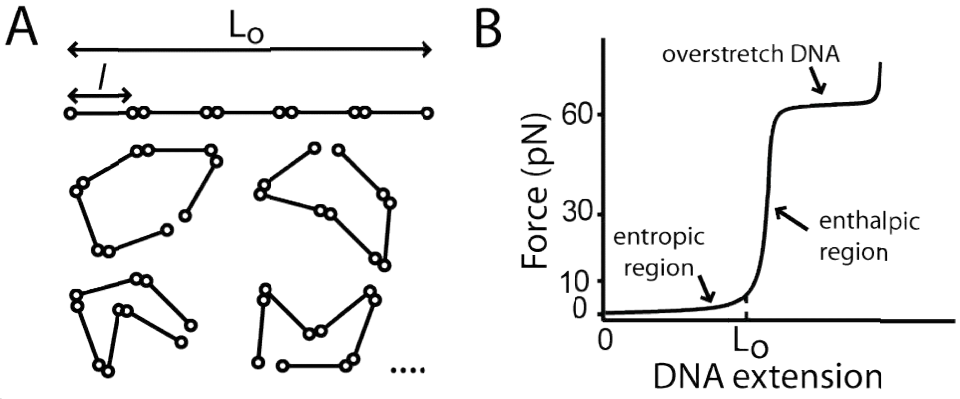

C

Model	Formula	Comments
Marko-Siggia (1995) WLC	$F = \left(\frac{k_B T}{L_p}\right)\left[\frac{1}{4(1 - x/L_o)^2} - \frac{1}{4} + \frac{x}{L_o}\right]$	Entropic theory. Interpolation formula of exact solution when [salt] ≥ 10 mM. Applicable when $F \ll$ ¼ $(k_B T K_o^2/L_p)^{1/3}$. Differs from exact solution by up to ~10% near $F \approx 0.1$ pN. Approaches exact solution at lower and higher forces.
Odijk (1995) WLC	$x = L_o\left[1 - \frac{1}{2}\left(\frac{k_B T}{F L_p}\right)^{1/2} + \frac{F}{K}\right]$	Entropic/enthalpic theory. Applicable for $\lvert x - L_o\rvert/L_o \ll 1$ (high-force regime).
Smith et al. (1995) FJC	$x = L_o\left[\coth\left(\frac{2FL_p}{k_B T}\right) - \frac{k_B T}{2FL_p}\right]\left(1 + \frac{F}{K_o}\right)$	Entropic/enthalpic theory. Applicable to polymers that approximate a FJC. Note that the Kuhn length = $2L_p$, and Langevin function $L(\alpha) = \coth(\alpha) - 1/\alpha$.
Modified Marko-Siggia WLC	$F = \left(\frac{k_B T}{L_p}\right)\left[\frac{1}{4(1 - x/L_o + F/K_o)^2} - \frac{1}{4} + \frac{x}{L_o} - \frac{F}{K_o}\right]$	Entropic/enthalpic theory. Modification of Marko-siggia formula to incorporate enthalpic stretching. Has limitations similar to Marko-Siggia near $F \approx 0.1$ pN.

WLC, Wormlike chain; FJC, freely jointed chain; F, force; x, extension (end-to-end distance); L_p, persistence length; L_o, contour length; K_o, elastic modulus; $k_B T$, Boltzmann's constant times absolute temperature.

Figure 3-3 DNA elasticity. A) Entropic force makes that dsDNA presents a compact configuration. A polymer of length Lo can be in more microscopic configurations when its ends are close to each other than when its ends are apart by a distance Lo. B) A representative force/extension curve of a dsDNA molecule is shown. For forces below 10 pN the main contribution to the elastic properties of DNA are entropic. For forces between 5-50 pN enthalpic contribution has to be considered. C) Four models have been proposed to fit the dsDNA force/extension curves. The best fitting model will depend on the forces applied to stretch the dsDNA. Table modified from reference[63].

3.7 Molecular motors and optical tweezers

Molecular motors are unusual machines that convert chemical energy to mechanical energy directly rather than via an intermediate such as heat or electrical energy. How much force does the motor generate? How fast it moves? How efficient is it? These are some of the central questions that have to be

answered to understand the molecular mechanism of force generation[76]. Single-molecule techniques have contributed to a fast progress in the understanding of how motor proteins work. In particular, optical tweezers has become a powerful tool to study the molecular mechanisms of molecular motors, via direct measurement of forces and displacements.

Within eukaryotic cells vesicles, chromosomes, and organelles are actively transported by molecular motors which translocate along cytoskeletal tracks of actin filaments or microtubules (MTs). Three different types of molecular motors for intracellular transport have been found: myosin, dynein and **kinesin**. All of them have a catalytic motor domain where ATP is hydrolyzed, providing the chemical energy to perform mechanical work. Each of these molecular motors comprises a superfamily of highly conserved ATP-dependent motor proteins[77,78,79]. Myosin proteins bind to actin filaments, while dynein and kinesin proteins bind to MTs. Detailed information about myosin and dynein can be found at references[80,81,82,83].

Kinesin was the last one of these three molecular motors to be discovered. In 1985, a series of studies of the fast axonal transport in giant squid neurons culminated with the identification of kinesin, a novel ATP-dependent molecular motor responsible for the anterograde transport of organelles along microtubules[84,85,86].

Currently kinesins form a superfamily composed by 15 kinesin families, which are termed kinesin1 to kinesin 14B and can be grouped into: N-kinesins that have a motor domain in the amino-terminal region, M-kinesins that have a motor domain in the middle, C-kinesins that have a motor domain in the carboxy-terminal region[79], and the bipolar kinesins with motor domains at each end of the protein. N-kinesins (e.g. kinesin-1) present anterograde transport, moving toward the plus end of MTs, unlike C-kinesins (e.g. kinesin-14) which transport their cargo toward the minus end of MTs. Meanwhile the M-kinesins. (e.g. kinesin-13) depolymerize microtubules and are associated to the mitotic spindle[87] as well as the bipolar kinesins (e.g. kinesin-5 or BimC) which are essential for the formation and functioning of a normal bipolar spindle[88] (Figure 3-4). Nowadays, the first kind of

kinesin discovered is classified as an N-kinesin that belongs to the kinesin-1 family, and is usually referred as conventional kinesin. From now on herein conventional kinesin will be referred to just as kinesin.

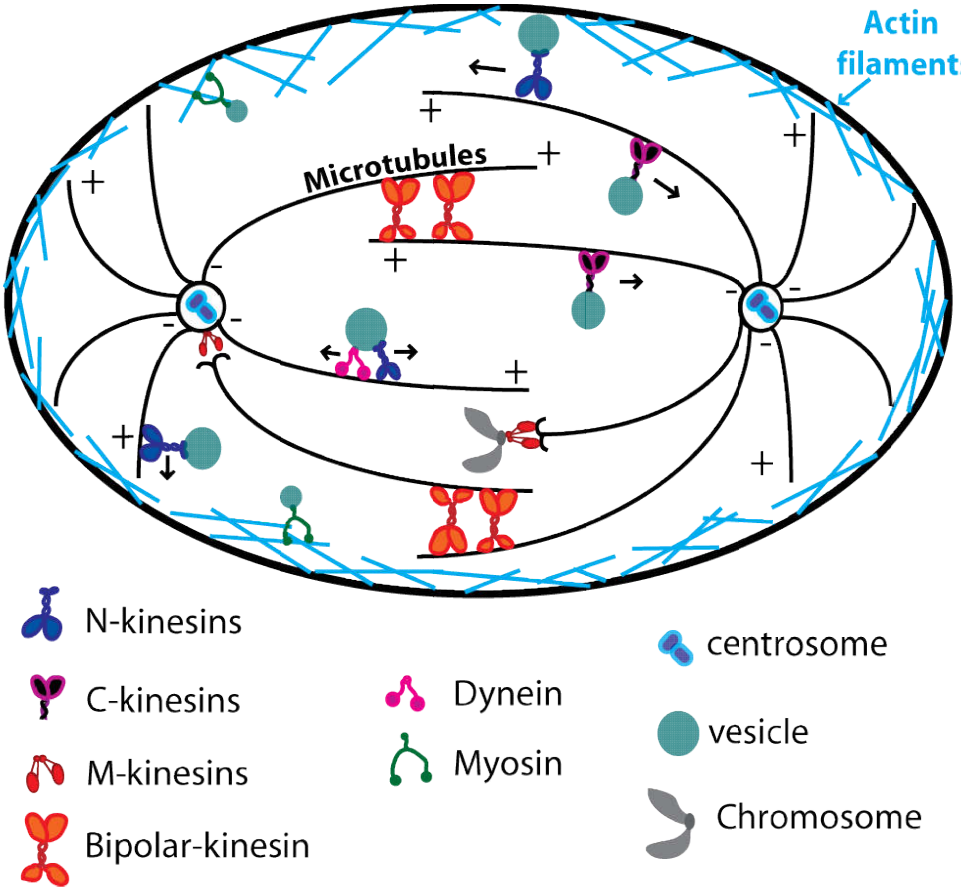

Figure 3-4. Molecular motors involved in intracellular transport. Intracellular transport of vesicles, organelles, and chromosomes is performed by the molecular motors kinesin, dynein, and myosin. Usually more than one motor is bound to the same cargo. Kinesin and dynein motors bind to microtubule filaments, meanwhile myosin binds to actin filaments.

Kinesin is a heterotetramer formed by two heavy chains, where the catalytic motor domain resides, and two light chains that are disposable for motor motility[89]. Instead, light chains are involved in the binding of kinesin to its cargo, in the selection of the cargo[90], and in the inhibition of the motor domains activity in the absence of a cargo[91]. The crystallographic structure of kinesin showed that heavy chains dimerize through a stalk region with coiled-coil motifs interrupted by two flexible hinges. Each heavy chain has a catalytic motor domain, usually referred to

as the head, and a tail motif where light chains can get bound (Figure 3-5). Each head has an ATP-binding pocket and a microtubule-binding domain and after dimerization of the heavy chains, an angle of 120° is formed between the heads[92].

The functioning of the motor domains is coordinated through a neck linker, a ~15 amino acids long motif that connects each head with the stalk and works as a mechanical amplifier of the motor activity of the head[93]. The neck linker is involved in head coordination[94] and is implicated in controlling the kinesin direction of movement along a MT[95]. The neck linker is essential for the force-generating mechanism of kinesin, connecting the chemical energy obtained from ATP hydrolysis with a conformational change that drives kinesin motility.

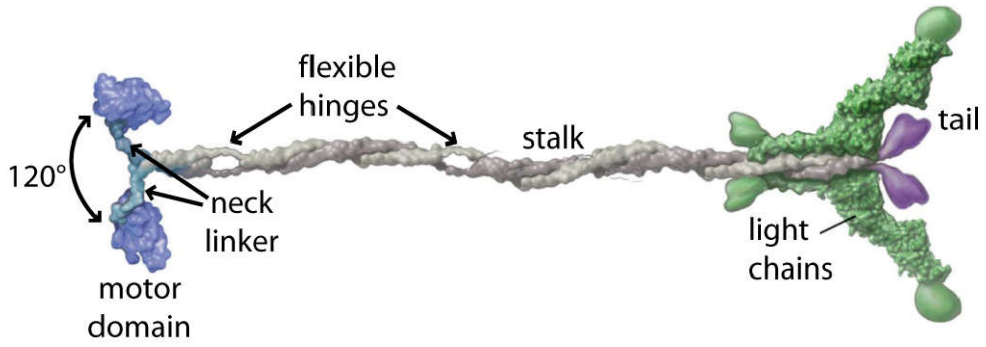

Figure 3-5. Structure of the heterotetramer kinesin-1. Kinesin-1 or standard kinesin is formed by two heavy chains, each one with one catalytic motor domain that hydrolyzes ATP and binds to a MT. Kinesin also has two light chains that are involved in the selection of the cargo and are not necessary for the motor translocation along the MT. Image modified from reference [97]

This region becomes immobilized and extended towards the microtubule plus end when kinesin binds to a microtubule and an ATP molecule. The neck linker reverts to a more mobile conformation when gamma-phosphate is released after nucleotide hydrolysis[96].

It was shown that a single kinesin is capable to displace MTs for several micrometers[98], thus kinesin is a processive motor that can translocate along MTs without getting detached. Diverse models were proposed to explain the high processivity of kinesin, but today the most accepted model is the hand-over-hand

mechanism[99,100]. In this model one head is detached from the MT meanwhile the other head remains bound to the MT. Once the rear head passed through the front and bounds to the MT, the other head can get detached and repeat the process, so heads are alternated one in front of the other along the same protofilament of the MT[101]. Notably, a single kinesin molecule can take on average 100 of steps before it dissociates from the MT. Behind this processivity, a tightly coordination between the two heads of kinesin is essential, thus when one head passed to the leading position the other remain attached to the MT. Otherwise both heads will remain attached without movement or both heads will be unattached to the MT and the motor will diffuse away from the MT[102]. Figure 3-6 presents the known kinesin processivity mechanochemical cycle.

Optical tweezers have been used to directly measure that the maximum load that a single kinesin motor supports before it dissociates from the MT is ~7 pN[103]; that kinesin translocates along MTs with steps of 8.2 nm[104]; and that for each kinesin step one molecule of ATP is hydrolyzed[105]. The 8.2 nm size step corresponds directly to the lattice spacing of tubulin dimers along the MT[101] and was an important piece of information to set the current model of kinesin stepping.

In this work kinesin single-molecule assays were performed to validate the fully functionality of our optical tweezers setup, measuring the step size and the maximum load supported by a single kinesin while it translocates along a MT.

3.1 Results

This section summarizes the results published in **Hernández Candia CN**, Tafoya Martínez S, Gutiérrez-Medina B (2013*) A Minimal Optical Trapping and Imaging Microscopy System.* PLoS ONE 8(2): e57383. doi:10.1371/journal.pone.0057383.

3.8.1 Abstract

We have constructed and tested a simple and versatile optical tweezers apparatus made from individual optical components, capable of visualizing individual microtubules (MTs, ~25 nm in diameter) and of studying macromolecules at the single-molecule level, using a minimal set of parts. Our design is based on a

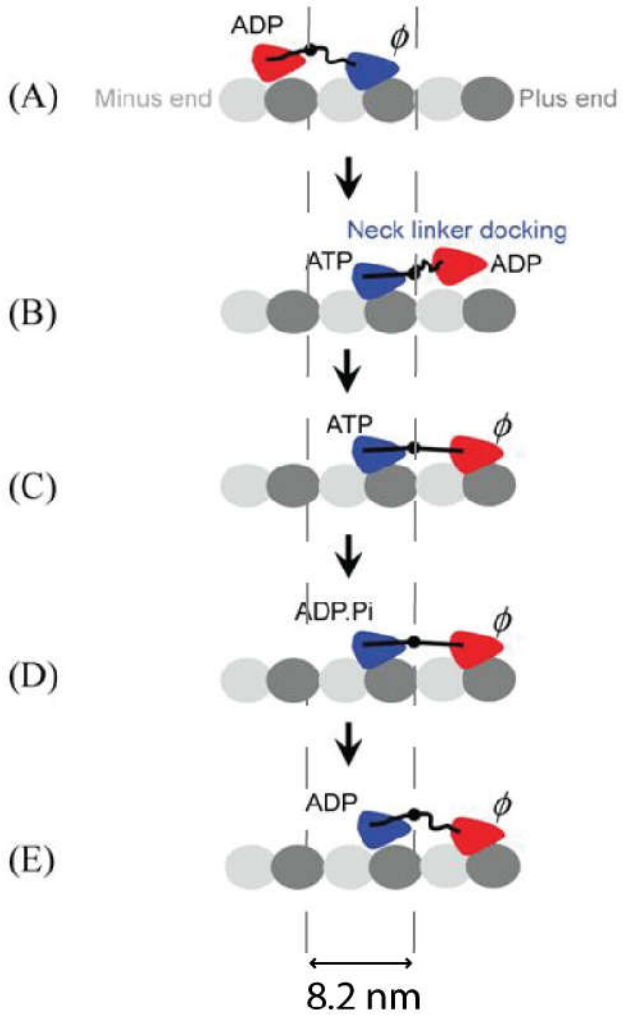

Figure 3-6. Mechanochemical coordination of kinesin. A) Initially the leading head (blue) in nucleotide-free state (ϕ)is strongly bounded to the MT and the trailing head (red) in ADP state is weakly bounded to the MT. B) The binding of ATP to the leading head induces the docking of its neck linker to the motor domain, delivering the trailing ADP-head to the leading position. C) Then, the tethered ADP-head diffuses to the nearest binding site on the MT, activating ADP release and the strong binding of the head to the MT. D) The strain between the two neck linkers induced by strong bindings of both heads to MT accelerates the hydrolysis of ATP to ADP.Pi in the trailing head (blue) but reduces the rate of ATP binding to the leading head (red). E) After Pi is released from the trailing head (blue), the state of dimeric kinesin becomes that of A) except that the motor has moved forwards by one step of 8.2 nm. Image modified from reference [106]

conventional, inverted microscope operating under plain bright field illumination. The illuminating system of the microscope is composed by a current-stabilized LED source, a collector lens system, a field diaphragm, a condenser iris diaphragm, a relay lens (LR) that images the condenser iris diaphragm onto the condenser back focal plane (BFP), and the condenser. All of these elements are adjusted for Koehler illumination. On the other hand, a single IR laser beam, coupled into the microscope, enables both standard optical trapping and BFP detection for the measurement of molecular displacements and forces. We are able to optimize imaging of the microscope by using computer-based digital image processing, effectively removing the background, reducing noise, and enhancing contrast. Altogether, our system yields excellent sample visualization in real-time, without the use of any specialized optics and without affecting the optical tweezers optical path. We have tested the optical trapping instrument by measuring the persistence length of dsDNA at high ionic strength and by following the stepping of the motor protein kinesin on clearly imaged MTs. Proving that our optical tweezers has spatial resolution of ~1 nm, maximum load of ~10 pN and time resolution of ~10 μs, and it is fully functional for single-molecule studies.

3.8.2 Motivation

Optical tweezers provides a unique approach to study at a single-molecule level the mechanical properties of macromolecules and also to follow its dynamic and conformational changes in real time. In particular we are interested in understanding how two or more molecular motor coordinate to allow efficient intracellular transportation, how DNA binding proteins recognize specific DNA sequences, and also we are interested in how blue light photoreceptors performed the conformational change that transduct the detected stimulus of light (see chapter 4). However, in Mexico or Latin America there was not an optical tweezers able to perform single-molecule assays, so we took on the task of building a fully functional instrument and at the same time we improved the imaging capabilities of the optical tweezers through CEBFM.

Regarding the optical tweezers setup, usually a bright field microscope is used to build it providing a way to get a highly focused laser beam and at the same time the microscope can be used to visualize the sample. This dual function of the microscope is limited by the visualization capabilities of bright field microscopy. If small or thin and transparent object is wanted to be observed then a different microscopy modality has to be implemented to overcome the lack of contrast in bright field. Differential interference contrast (DIC), dark field, and phase contrast microscopy allow visualization of transparent samples, however extra elements have to be added to the optical path, thus impairing constraints like polarization or phase into the optical trapping beam and increase the cost and complexity of the system. We propose that implementation of CEBFM to an optical tweezers will allow the visualization of transparent objects without modifying the optical path of the trapping beam.

3.8.3 Main results

An optical trapping system with exceptional visualization features at minimal cost and complexity was developed. Our optical tweezers system is based on a conventional inverted microscope that satisfies Koehler illumination and position detection of the trapped particle through BFP method[53]. High contrast imaging was implemented by CEBFM (see chapter 2)[14], where no extra optics are present in the trapping beam path. A convenient feature of our optical setup is that a relay lens LR effectively decouples the illuminating system from the optical tweezers detection stage (Figure 3-7). In practice, we can close the condenser iris diaphragm almost entirely (~90%) to maximize contrast for sample visualization, while simultaneously using the full numerical aperture of the condenser for BFP detection.

Stiffness of the trap was estimated by Equipartition method, Stokes' method and Power spectrum method, and to verify the functionality of our optical tweezers, two standard single-molecule assays were performed. First, we stretched single dsDNA molecules, and from the force/extension records, the persistence length and the contour length were obtained.

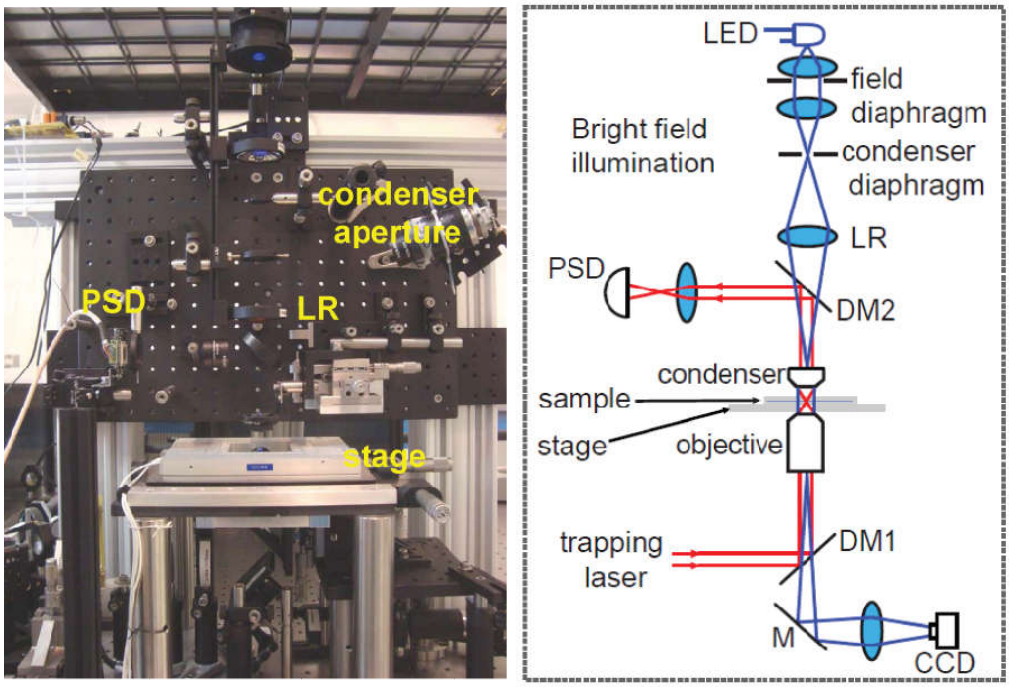

Figure 3-7. Our optical tweezers is based on an inverted bright field microscope. Trapping light is provided by a continuous wave laser λ=1064 nm. Position sensitive detector (PSD) and back focal plane configuration are used for position detection of trapped beads. Koehler illumination is decoupled from the trapping system through lens LR. Dichroic mirrors are used to couple (DM1) and decouple (DM2) the laser trapping light form the BF microscope optical train. Both condenser and objective lenses have a high NA and are oil immersion ($NA_{objective}$=1.3, $NA_{condenser}$=1.4). The illumination source is a blue LED (λ= 450 nm) and an 8-bit charge-couple device (CCD) camera is used for visualization of the sample.

A 3039 bp DNA fragment was amplified using 2 modified primers with tags at their 5' ends (biotin and digoxigenin, respectively). The biotin end of the dsDNA molecule was attached to a 0.7-μm diameter avidin-coated bead, while the other end was attached to the surface of the cover slip through a digoxigenin-antidigoxigenin linkage (Figure 3-8 A). The surface-tethered bead was optically trapped, and the surface was displaced using a piezoelectric stage. As the DNA molecule is unwrapped and stretched, the trapped bead is pulled from its equilibrium position, which we can measure. From this procedure a force vs. extension graph was obtained. Fitting the force/extension data to the worm-like chain model (Figure 3-8 B), the parameters Lp and Lo were obtained.

Statistic analysis of these parameters provided the following values for the contour length: Lo = 1103 ± 2 nm (mean ± sem) (Figure 3-8 C), and for the persistence length: Lp =49 ± 0.9 nm (mean± sem) (Figure 3-8 D). These values correlate well with the expected parameters. The expected value for Lo was ~1073 nm, estimating ~1053 nm for the 3039-bp chain, with 0.34 nm rise per bp, and ~20 nm for the biotin-streptavidin and digoxigenin-anti-digoxigenin linkages. Whereas the expected range of the persistence length value is between 43.8 nm and 56.2 nm at an ion concentration of [Na+] = 150 mM[68].

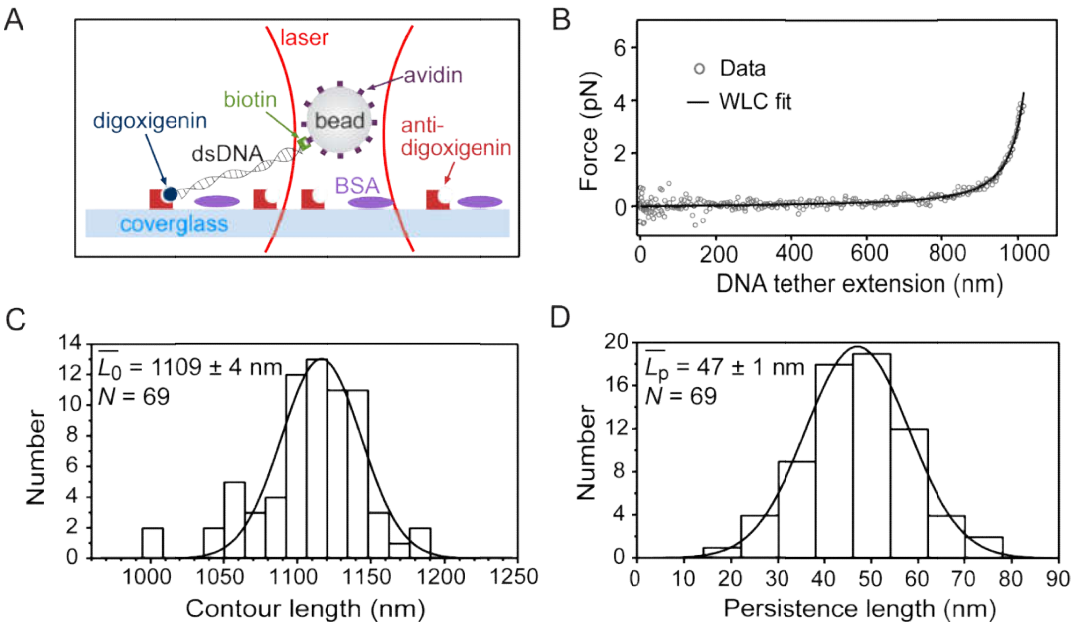

Figure 3-8. Stretching of a single-molecule of dsDNA. A) Schematic of the surface-based assay, not to scale. B) A typical force-extension record (black circles) together with a worm-like chain (WLC) polymer model fit (black line). C) Histogram of contour length values. Fit to a Gaussian (black line) yields: 1116 ± 2 nm ($\mu\pm \sigma_\mu$). D) Histogram of persistence length values. Fit to a Gaussian (black line) yields: 47.0 ± 0.2 nm ($\mu\pm \sigma_\mu$). Legends display data mean ±sem.

Second, we measured the step size and maximum sustainable load for the molecular motor kinesin. We expressed a truncated version (401 aa) of kinesin-1 (*Drosophila melanogaster*) with a 6His-tag, in Escherichia coli. Purified protein was incubated with 0.54-μm diameter anti-6His-coated beads, in a stoichiometry such

that only one kinesin gets attached per bead. The beads were flowed into a sample chamber with MTs fixed to the coverslip surface (Figure 3-9 A). Using optical tweezers, a kinesin-carrying bead in the sample was trapped and moved as close as possible to a MT visualized by CEBFM (Figure 3-9 B). When kinesin gets in contact with the MT, it starts to translocate, moving the bead along. The displacement of the bead was detected as a function of time. From the displacement data and the measured stiffness of the trap, the force exerted by the kinesin molecule was determined. We observed 8.2-nm steps, and maximal sustained forces by kinesin of ~7pN (Figure 3-9 C), in agreement with previous reports[103]. Our optical tweezers is fully controlled through diverse routines implemented in LabView 8.5 (National Instruments) software, simplifying the use of the instrument.

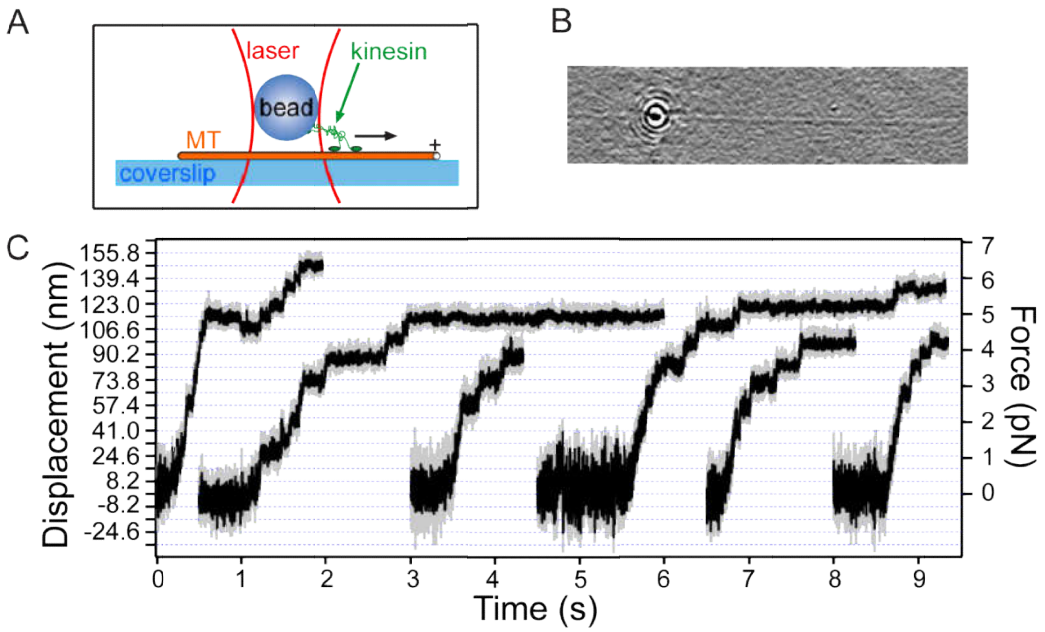

Figure 3-9. Optical tweezers plus CEBFM allow to follow kinesin stepping on clearly image microtubules. A) Schematic of the kinesin bead assay. B) A kinesin-carrying trapped bead is placed directly above an individual MT, visualized using digital image processing. C) Representative records of kinesin-driven bead motion displaying steps at 8.2 nm intervals and the development of forces up to ~7 pN. [ATP]=100 μM.

3.8.4 Novel contribution

To overcome bright field microscopy limitations we implemented a CEBFM during the acquisition of the images, which allowed us to visualize transparent objects as MTs without modifying the optical path of the trapping beam. Our optical tweezers configuration shows that the improvement of bright field imaging via digital image processing can benefit single-molecule techniques such as optical tweezers.

3.8.5 Conclusions

An optical trapping system has been developed with exceptional visualization features at minimal cost and complexity. The technique of CEBFM provides an alternative to elaborate microscopy techniques for high-contrast visualization, avoiding the inclusion of optical elements in the instrument (such as prisms, apertures or polarizers) that could compromise operation of optical trapping. Using our instrument, it is possible to achieve independent control of BFP detection (in optical trapping) and Koehler illumination (in sample visualization). The approach presented here is uniquely suited for single-molecule experiments and the setup can also be readily expanded to incorporate additional features, such as a second trapping beam (to perform off the surface, multiple-bead assays), or strategies to maintain a constant force during experiments (a ‘force clamp’).

3.2 Future work

Future work included studies to understand the coordination of kinesin motors between heads and between motors coupling more than one motor to the same cargo. Also the conformational change of a blue light photoreceptor named ENVOY (see chapter 4) and the interaction of the transcription factor Catabolite Activator Protein (CAP) with its consensus promoter region are planned.

Chapter 4. Fungal Blue-Light Photoreceptors: VIVID and ENVOY

Sunlight provides Earth with a constant flux of energy and it has been a factor for life evolution, leading to positive selection of organisms able to detect, harvest or respond to light. Organisms have developed structures capable of performing photosynthesis, harvesting the energy of light and transforming it into chemical energy, which can be stored and consumed later by the organism itself or by other organisms. A side effect of photosynthesis has been the production of **molecular oxygen (O_2)**, which transformed Earth's atmosphere composition and helped to rise an explosion and diversification of life organisms with metabolism dependent on O_2 chemical reactions[107] and with molecular strategies to avoid, regulate or repair collateral damage of **reactive oxygen species** (**ROS**). Also, photosynthetic and non-photosynthetic organisms must accurately sense and respond to their environment and have developed strategies to decode sunlight cues into information of their position, food availability, presence of danger and, in general, organisms have developed circadian rhythms due to lit-dark periods for Earth's rotation movement[108].

Filamentous fungi do not perform photosynthesis, but they present pigment synthesis[109], phototropism[110], photomorphogenesis[111], circadian rhythm of conidiation[112], among other responses as an adaptation to live under light conditions. These easily detectable phenotypes have made filamentous fungi like *Neurospora crassa* and *Trichoderma atroviride* model organisms to learn about perception, adaptation and response to light in eukaryotic cells.

For *N. crassa*, **blue light (BL)** induces membrane potential changes[113], induces circadian production of conidias[114], triggers protoperithecia formation[115], induces the expression of 5% of *N. crassa* genes [116], induces the entrainment and resetting of the circadian clock, and induced the synthesis of carotenoids[117,118]. In the fungus *Trichoderma atroviride* exposure to BL induces a photoconidation process[119] and the transcriptional activation and repression of diverse genes[120] (Figure 4-1).

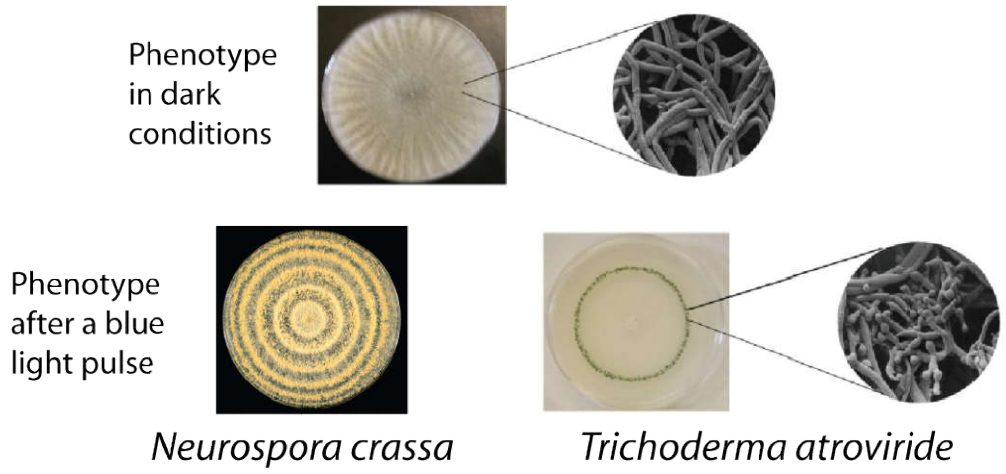

Figure 4-1. Blue light induced phenotypes in *N. crassa* and *T. atroviride.* Both fungi grow as mycelium under dark conditions. After a blue light pulse, *N. crassa* develops a ring of conidia at the growing periphery of the colony where the stimulus was given, along with the synthesis of β-carotenoids in mycelia, which provide the characteristic orange color to the fungus. Furthermore, the entrainment of circadian rhythm is triggered with rhythmic conidiation with a period of ~24h (left). For *T. atroviride*, a blue light pulse induces the formation of a green ring of conidia at colony perimeter at the time the stimulus was given (right). For *T. atroviride* even when circadian rhythm is expected, a clear phenotype as in *N. crassa* has not been reported. Image modified from reference [119]

At a molecular level light is perceived by photoreceptors, which are proteins that contain a light-sensing chromophore that modulate their biological activity after photoreception[121]. Light perception mechanisms involve chromophore absorption of light at a specific wavelength range and then a light driven reaction takes place, triggering a conformational change in the protein and transducing the light input information into a biological response. Photoreceptors can be divided in three main

classes: flavin-based UV/blue-light receptors, retinal-based green-light receptors, and linear tetrapyrrole-based red-light receptors[121].

Three different classes of flavin-based photoreceptors have been described: Proteins carrying a **Light Oxygen Voltage (LOV) domains**, Blue Light sensor Using FAD (BLUF) proteins, and Cryptochromes (CRYs)[122].

4.1 Fungal blue light photoreceptors

In *N. crassa* primary proteins for fungus response to light are the transcription factors White collar-1 (WC-1) and White collar-2 (WC-2), of which WC-1 is a LOV-domain photoreceptor[123]. WC-1 presents one LOV domain, two Per-Arnt-Sim (PAS) domains, a GATA Zinc finger domain, a nuclear localization signal (NLS), and two transcription activation domains (AD) each one at opposite sides of the protein[124]. Meanwhile the WC-2 protein presents one PAS domain, a transcription AD, a NLS, and a GATA Zinc finger[125].

The current model[126] for *N. crassa* light perception establishes that after a day/night entrainment of the circadian rhythm, under dark conditions WC-1 and WC-2 form a heterodimer complex named White Collar Complex (WCC). WCC activates transcription of the gene frequency (*frq*), necessary to keep the circadian timing in constant darkness, by binding to the Clock box (C-Box) within the gene promoter[127]. After a blue light pulse, the LOV domain in WC-1 proteins is activated, allowing the interaction between LOV domains and the assembly of the Large White Collar Complex (L-WCC)[124]. This L-WCC transiently activates the transcription of light regulated genes as albino genes (*al-1, al-2 al-3*) involved in the carotenoid pigments biosynthesis, the vivid gene (*vvd*) that encodes for a small photoreceptor with a LOV domain, and also increased the transcription of the *frq* gene to entrain the circadian rhythm. After a BL pulse, the L-WCC binds to the light response elements (LREs) in the promoter of light activated genes and unbind through a rapidly hyperphosphorylation of the WC proteins[128].The **VIVID (VVD)** LOV-domain protein interacts with the WCC inhibiting the formation of the L-WCC, thus repressing the expression of BL activated genes.

Besides working as a negative repressor of transcription, VVD is proposed to work as a positive regulator of transcription. Inhibiting the formation of the L-WCC, VVD also inhibits the phosphorylation and consequent degradation of the WC proteins, leaving them available for a second response to a higher blue-light stimulus[129]. Figure 4.2 summarizes a simplified model for the *N. crassa* light perception mechanism.

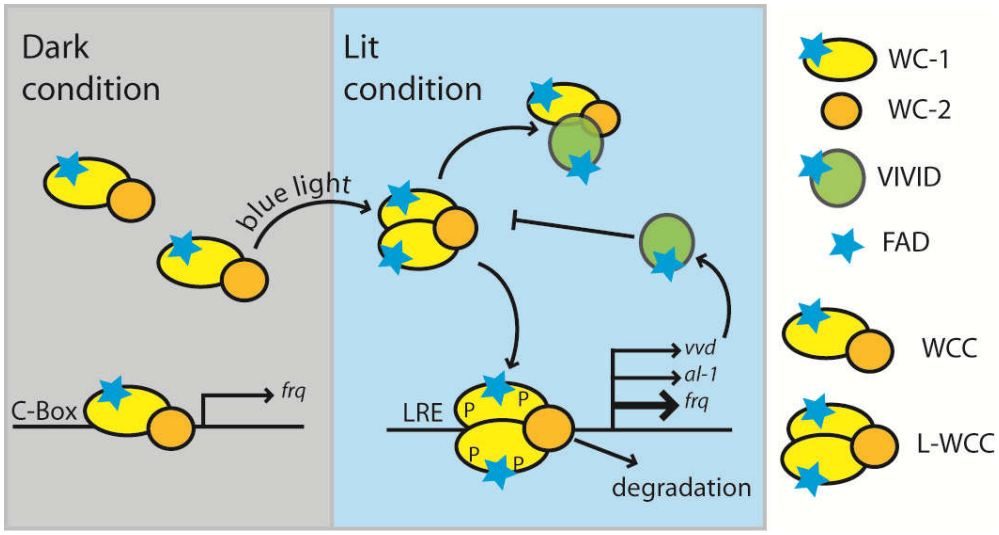

Figure 4-2. Simplified model of the *N. crassa* light perception mechanism. In *N. crassa* circadian rhythm is entrained by light stimulus. Under dark phase a White collar-1 (WC-1) and White collar-2 (WC-2) complex is formed activating the transcription of the *frq* gene. After a blue-light pulse the Large White Collar complex (L-WCC) is formed, activating the transcription of blue-light responsive genes.

In *T. atroviride* two WC homologous proteins have been found to be essential for the photoconidation as well as the regulation of some genes expression. These proteins have been called Blue Light Regulated proteins BLR-1 and BLR-2. Accordingly, *T. atroviride* strains that have a deletion of any of these two genes present a loss of the blue light-dependent responses[130]. The sequence of BLR-1 presents one LOV domain, two PAS domains, and one GATA Zinc finger domain. The BLR-2 protein has one PAS domain, a coiled-coil (C-C) structure, one histone deacetylase (HDAC) binding domain, and one GATA Zinc finger domain[119]. The presence of the GATA Zinc finger domain in both BLR-1 and BLR-2, the HDAC domain in BLR-2, and the missing genetic regulation in the mutant strains suggest

that the BLR-1/BLR-2 complex works as a transcription factor of blue light regulated genes[120] (Figure 4-3). The homologous protein of VVD in *T. atroviride* is the ENVOY protein **(ENV1)**, whose expression is regulated by the BLR proteins, and it is proposed that ENV1 acts in a mode that resembles VVD functioning, repressing the transcriptional activity of BLR proteins.

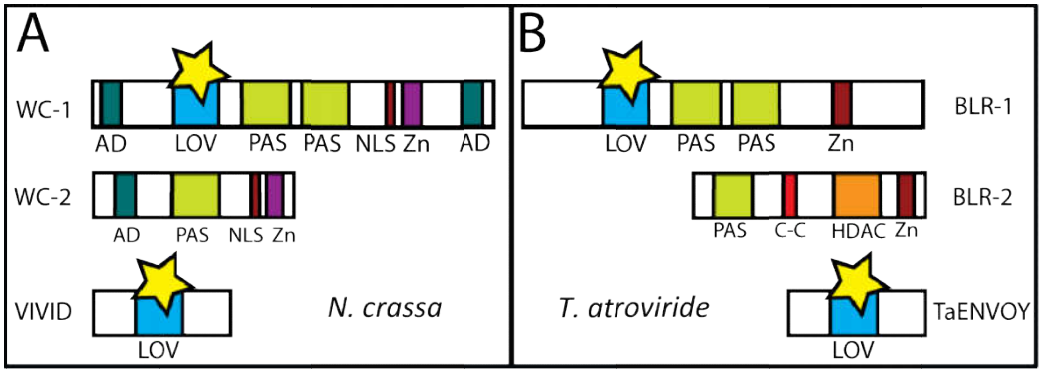

Figure 4-3. Domain composition of *N crassa* and *T atroviride* proteins involved on fungi responses to blue-light. A) For *N. crassa* WC-1 and VVD are BL receptors, and both carry a LOV-domain that binds a flavin cofactor (yellow star). B) The homologous proteins in *T. atroviride* present different domains, but conserve the LOV-domains for perception of BL.

Notably in *N.crassa* as in *T. atroviride* the main responses to light relapse on proteins carrying a LOV-domain, so it is imperative to fully understand LOV-domain functioning to understand fungal response to BL. LOV-domains belong to the broad family of flavoproteins and part of their characteristics are due to features of the flavin cofactor.

4.2 Flavins and Flavoproteins

Flavoproteins are ubiquitous proteins and their flavin cofactor catalyzes diverse oxidation–reduction processes and photochemical reactions. In the organism *Saccharomyces cerevisiae*, 68 genes have been identified to encode flavin-depending proteins to which 47 distinct biochemical functions were assigned[131]. In humans 90 genes have been identified to encode for flavoproteins, of which 2/3 are linked to human diseases[132], highlighting the importance and broad range of physiological activities where flavoproteins are involved. Some of the biological processes where flavoproteins are involved include mitochondrial respiration,

xenobiotic metabolisms, biosynthesis of metabolites, perception and signaling of BL stimulus[133], and magnetosensing[134],making flavoprotein one of the most studied family of proteins.

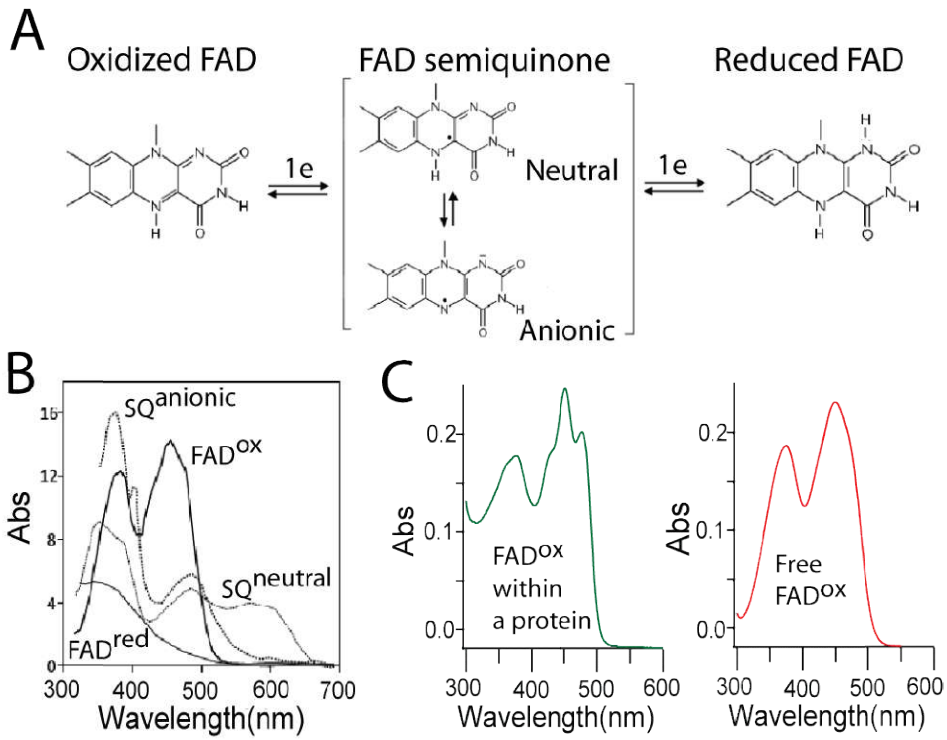

Figure 4-4. Flavin structure and absorption spectrum of its differentredox states. A) Different redox states of FAD. B) Characteristic absorption profile of FAD at its different redox states. Oxidized FAD (FAD^{ox}), Reduced FAD (FAD^{red}), Neutral Semiquinone ($SQ^{neutral}$), Anionic Semiquinone ($SQ^{anionic}$). C) Absorption profile of a flavin within a LOV-domain protein vs absorption profile of a free flavin in the same redox state (oxidized FAD, FAD^{ox}). Panel A and B were modified from reference [136].

Flavins are derived from rivoflavin (vitamin B_2) and as prosthetic group flavins are used as flavin mononucleotide (FMN) or as **flavin adenine dinucleotide (FAD)**. FMN and FAD possess a tricyclic heteroaromatic isoalloxazine ring that can reversibly accept and donate one or two electrons, thus flavins present up to three redox states: oxidized, semiquinone, and fully reduced state. Partially reduced flavin (semiquinone) has two possible states: neutral semiquinone and anionic semiquinone (Figure 4-4 A). Each of these four states presents a characteristic absorption spectrum (Figure 4-4 B). The resolution of flavin absorption spectrum

can increase presenting new peaks due to the polarity (hydrophobic/hydrophilic) of the solvents or the protein environment[135] (Figure 4-4 C). Therefore, flavoproteins present a characteristic absorption profile which is dependent on two properties: the redox state of the flavin and the presence of the cofactor in a protein context.

Flavin molecules are good electron donors and have been implicated in the production of ROS. ROS include the superoxide anion (O_2^-•) which is the product of a one-electron reduction of oxygen, the hydrogen peroxide (H_2O_2) which is the dismutation of O_2^-•, and the hydroxyl radical (OH•) which is partial reduction of H_2O_2. ROS also include **singlet oxygen ($^1O_2$)**, which is not a reduced state of O_2, instead the spin orientation of the two unpaired electrons in the outer shell is flipped, producing two electrons with opposing spins that are highly reactive.

Besides being good electron carriers, flavin molecules can work as photosensitizers, absorbing the light and producing a photochemical change in other molecules without affecting themselves. As a photosensitizer the absorbed BL sends the flavin molecule to a singlet state which decays to a highly reactive triplet state. The triplet state can react with other molecules via electron transfer reaction (Type 1 mechanism) or via the transfer of the triplet state energy from flavin to another molecule (Type 2 mechanism). When oxygen is involved, flavin triplet state reactions can produce ROS, either reduced oxygen species or singlet oxygen (Figure 4-5), both of which are highly reactive and can interact with macromolecules as proteins, DNA and lipids[137,138,139]. Proteins constitute ~68% of the dry weight of a cell and therefore represent potentially major targets for oxidative damage[140].

Since flavin molecules are very reactive, mainly due to their triplet state, they are usually buried within the protein to protect them from reacting with O_2 or with potential exogenous electron donors or distal redox amino acids which may deviate flavins reaction from their standard enzymatic activity. In fact, how flavoproteins regulate the flavin reactivity, how these proteins avoid the production of ROS, and how often an off-pathway ROS producing reaction occurs are current open questions[141].

Flavins are also fluorescent molecules, since the singlet state can decay through fluorescence (Figure 4-5). Lately, this fluorescent feature has been exploited using some flavoproteins as a new class of genetically encoded fluorescent probes characterized by their small size and oxygen-independent maturation of fluorescence[142].

In the last decade, the chemical reactions diversity of flavin-binding photoreceptors have been explored, studying and using these proteins as engineered transducers of light input, fluorescent proteins, and ROS producers.

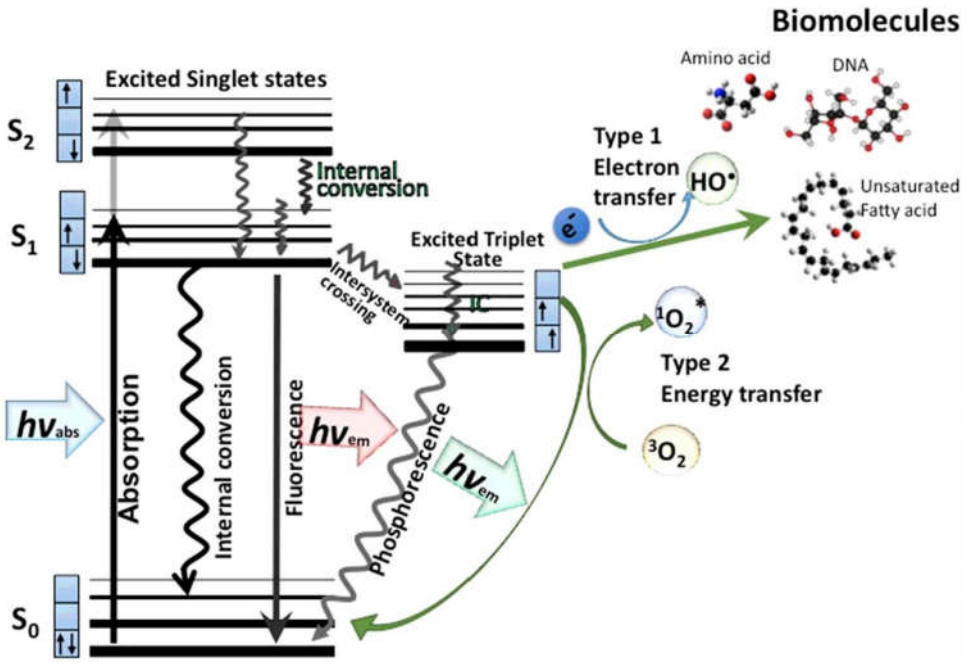

Figure 4-5. Photosensitizer scheme reaction. For photosensitizer molecules as flavins, absorbed light induces an excited singlet state that decays through fluorescence, or through an intermediate triplet state. Excited triplet state can decay emitting phosphorescence or reacting with $O_2$to produce ROS. Images reproduced from reference[143]

4.3 LOV domains

Photoreceptors with LOV domains are flavoproteins specialized on BL detection. LOV domains are widely distributed[144], present in plants[145], algae[146], fungi[147], and bacteria[148]. LOV domains are light allosteric regulators of a wide range of effector domains including kinases[149], DNA- binding domains[150] and transcription factors among others[151]. The biological activity of photoreceptors that contain only one

LOV domain (without a predicted effector domain) is performed *in trans*, interacting with other cellular proteins[152].

LOV domains form a subgroup of the PAS domain superfamily that bind as a cofactor a flavin molecule. LOV domain core structure resembles the Photoactive Yellow Protein (PYP) protein, which is define as the canonic structure of a PAS domain[153] (Figure 4-6 A). The core LOV domain structure is composed of a β-scaffold with 5 antiparallel β-strands (Aβ,Bβ,Gβ,Hβ,Iβ) and 4 α-helices that connect these elements (Cα,Dα,Eα,Fα)[122]. The flavin cofactor is bound noncovalently in the interior of the LOV domain by a network of hydrogen bonds, van der Waals and electrostatic interactions[154]. Variability between LOV domains is found in core flanking helices at N-and/or C-terminal ends[122] (Figure 4-6 B), in the bound flavin cofactor (FMN or FAD), and in an additional loop of 9-11 amino acids only present in FAD binding LOV domains[151], since it allows the accommodation of the large terminal adenine moiety of FAD (Figure 4-6 C).

As previously mentioned, the LOV domain flavin cofactor is a photosensitizer, so BL changes the electronic properties of the flavin isoalloxazine ring, sending the flavin to a transient singlet state that decays to a triplet state where flavin reacts with the thiol group of a highly conserved cysteine in the LOV domain, inducing the formation of a reversible covalent union between the carbon C4a of the flavin and a conserved cysteine[151] (Figure 4-7). The formation of this flavin-cysteine adduct propagates a conformational change that triggers the biological function of the protein. The standard photocycle of LOV domains implies a flavin transition from its oxidized redox state to its reduced state, although it has been reported that mutations of the adduct cysteine results in the one-electron neutral semiquinone form of the cofactor[155,156].

Flavin-cysteine adduct kinetics can be followed through UV-VIS spectroscopy, thanks to the characteristic absorption spectrum of the flavin cofactor which reflects the flavin redox state (Figure 4-4). Under dark conditions the flavin-cysteine adduct is not formed and the flavin cofactor is oxidized presenting a characteristic absorption profile with three main peaks between 400-500 nm. Upon BL

illumination, the reduction of the flavin and the formation of the flavin-cysteine adduct can be confirmed by absorption bleaching at 400 -500 nm and a single peak around 390 nm appears. The covalent adduct spontaneously decays to regenerate the dark state, and the reestablishment of the absorption at 400-500 nm reflects the adduct's decay kinetics[122].

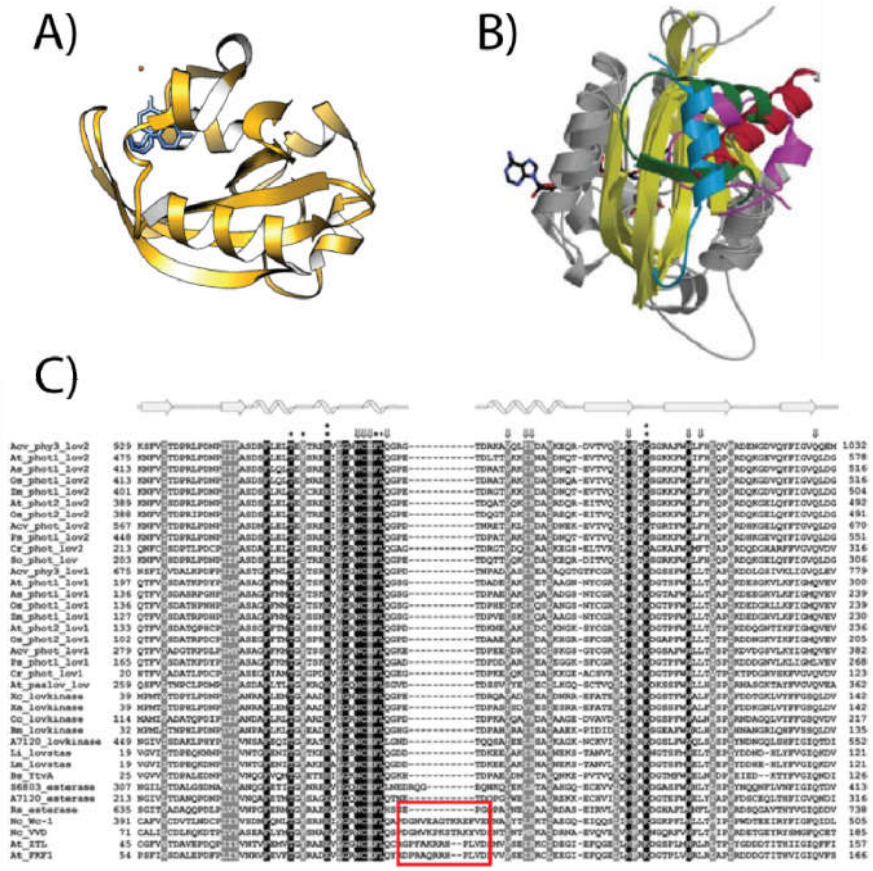

Figure 4-6. LOV domains present a PAS domain structure with variable flanking regions and an additional loop motif when FAD instead of FMN is bound. A) Photoreceptor Yellow Protein (PYP) is taken as the canonic structure of PAS domains (PDB ID 2PYP). PYP binds p-coumaric acid as cofactor (blue), being one of the few BL photoreceptors that do not bind a flavin as cofactor. B) The core LOV domain structure resembles a PAS domain. Superposition of the PAS domain of VVD(green), PYP (magenta), Drosophila PER (red) and AsLOV2 domain (blue). All proteins share a structurally conserved PAS domain (yellow) and variable helical regions at the N-or C-terminal region (gray). Image reproduced from reference [147]. C) Alignment of multiple LOV domains shows that an additional loop of 9 to 11 amino acids (red box) is required for FAD accommodation. Table modified from reference[151].

Flavin-cysteine adduct spontaneously decays with a rate that may vary by several orders of magnitude between different LOV proteins, so LOV domains can be broken down into two groups based on their lifetime adduct state: the fast cyclers with adduct lifetime of tens of seconds and the slow cyclers with a long-lived adduct state of thousands of seconds.

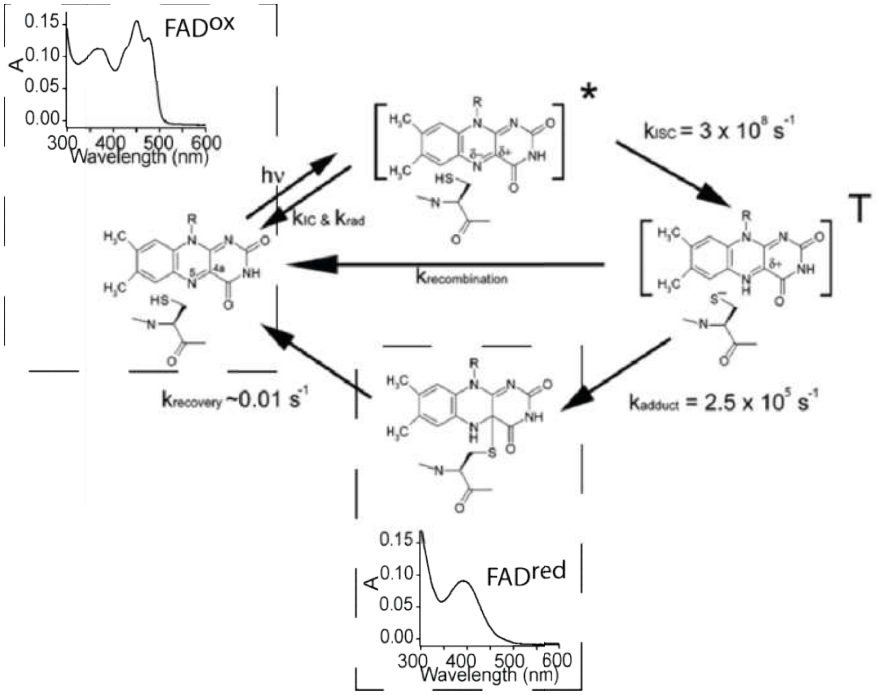

Figure 4-7 Blue-light triggered reaction that leads to flavin-cysteine adduct formation in LOV domains. Under dark conditions flavin is oxidized with a characteristic absorption profile center at 450 nm. Light induces a singlet state (denoted by an asterisk) which rapidly interconverts to a triplet state (denoted by $[\ ]^T$). The triplet state reacts with the thiol group of a highly conserved cysteine, forming a covalent bound (flavin-cysteine adduct). When flavin-cysteine adduct is formed, the absorption spectrum corresponds to a totally reduced flavin with a single peak around 390 nm. Flavin-cysteine adduct state spontaneously decays to the initial oxidized flavin state. Image modified from reference [151]

Since LOV domains have been reported to be involved in a variety of biological processes as phototropism[156], circadian clock regulation[127], photoconidiation[130] and photopigmentation[147] it has been proposed that the variability in the lifetime of the adduct state is important for the correct tuning of the biological function. Where the fast cycling could allow rapid attenuation and reversal of signaling, and the

slow cycling could be employed for a specific one-time event such as gating of the circadian clock[157]. Recently it was proved that the photocycle length of a LOV domain protein in *N. crassa* has biological implications, modifying fungal adaptation to light intensity changes[158].

The first LOV domain perception mechanism reported was for the phototropin-1 protein of *Avena sativa* (AsPhot), a multi-domain blue light receptor that induces the phototropism in plants[145]. AsPhot has two LOV domains named LOV1 and LOV2, which bind a FMN cofactor, and at the C-terminal AsPhot has a Ser/Thr kinase domain. Nuclear Magnetic Resonance (NMR) showed that after adduct formation an alpha helix situated at the C-terminus of the LOV2 domain (the Ccap Jα helix) presents a displacement. This conformational change of the LOV2 domain allosterically regulates the kinase activity of AsPhot, acting as a light regulated switch[159].

This result highlights the power of LOV domains as light regulated molecular switches and recently, this characteristic has been exploited in optogenetic experiments, where engineered fusion proteins can be regulated through the light activation of the LOV domains[160].

In this work we are interested in studying the case of two fungal LOV domains, VVD from *N. crassa* and TaENV1 from *T. atroviride*. Both are one-domain proteins and their biological function is related to the photoadaptation of the fungus, attenuating the light response on prolonged light exposure while remaining sensitive to increasing changes in light intensity[161,119].

4.4 The VIVID protein

VVD is a single LOV domain protein that has been shown to take part in the regulation of some circadian clock properties, most likely through its effects on the WCC transcriptional activation, including clock resetting and gating of light input to the clock[162], maintenance of the clock during the light phase[163], and temperature compensation of the circadian phase[164]. VVD also regulates the photoadaptation, keeping the fungus sensitive to a second blue light pulse with higher intensity, even under constant illumination conditions, by down-regulating the initial acute phase of

genes induction[161]. Furthermore, VVD can also have a role intercrossing light and osmotic stress responses pathways. In *N. crassa* glycerol accumulation is triggered as a response to hyperosmotic stress conditions by two pathways that involved the osmosensing proteins which are: the high osmolarity glycerol (HOG)-like mitogen-activated protein (MAP) kinase[165], and the putative phosphatase protein encoded by the *cut* gene[166] which expression is down-regulated by blue light through the WCC[167].

Under dark conditions VVD presents the characteristic absorption profile of oxidized flavin in a LOV domain context (Figure 4-4 C), with absorption peaks at 428, 450 and 478 nm. After BL illumination, adduct formation leads to a single peak at 390 nm that correspond to a reduced form of the flavin cofactor (Figure 4-8A). Size-exclusion chromatography (SEC), dynamic light scattering (DLS), small-angle X-ray scattering (SAXS)[168], and X-ray crystallography[147,169] indicate that adduct formation induces a conformational change in the VVD LOV domain, taking the protein from its inactive state (dark state) to its active state (lit state).

Regarding to the conformational change of VVD, X-ray crystallography studies have shown that after a BL pulse the adduct state is induced, the side chain carbonyl of glutamine 182 (Gln182) is flipped, and the cysteine 71 (Cys71) rotates into a more exposed position to interact with the asparagines 68 (Asp68). All these rearrangements, triggers the detachment of two motifs called aα–helix and bβ–strand, located at the N-terminus of VVD[147](Figure 4-8B). This conformational change exposes VVD regions that interact with the LOV domain in WC-1[152], allowing the *in trans* action of VVD as a regulator of the WCC. VVD conformational change contrasts with the reported conformational change of *Avena sativa* LOV2 that occurred at the C-terminus instead of at the N-terminus[170] (Figure 4-8C).

Two cysteines have been proposed to play a major role in the conformational change of the VVD LOV domain. The first cysteine (C108), located in the pocket core, forms the adduct with the FAD molecule, and the second cysteine (C71) acts as a hinge allowing the displacement of the aα–helix and bβ–strand motif.

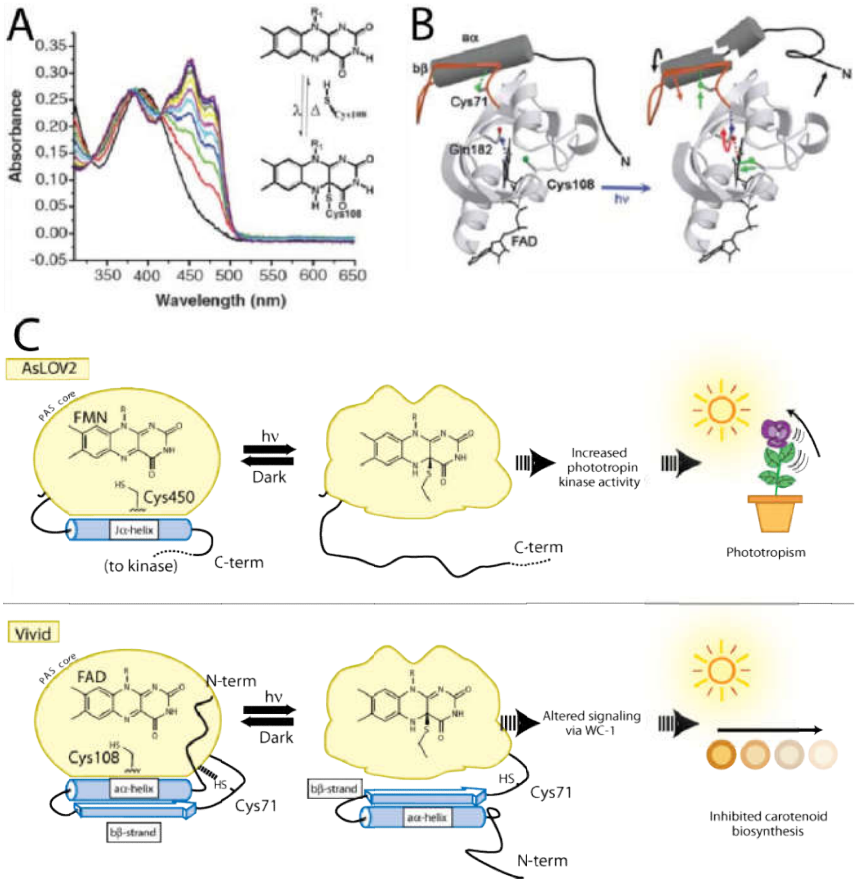

Figure 4-8. After a BL pulse VVD LOV domain performs a conformational changedisplacing its N-terminal aα-helix and bβ-strand. A) Absorption spectrum of VVD. Black line represents the lit state after illumination. Rainbow colors represent the profiles at different recovery times. Flavin-cysteine adduct decay kinetics can be followed through the recovery of the absorption peak at 450 nm. B) Crystallographic structure of lit and dark VVD state shows that after adduct formation glutamine 182 flips its lateral chain propagating a conformational change that ends with the displacement of the N-terminal aα-helix and bβ-strand motifs, and where cysteine 71 woks as hinge. Images in A) and B) were modified form reference[147]. C) The conformational change in the LOV domain of VIVID (VVD) differs from the conformational change of *Avena sativa* LOV2 (AsLOV2). On both LOV domains BL induces a flavin-cysteine adduct. For AsLOV2 after adduct formation the αJ helix (at the C-terminus) is extended activating the kinase activity of the protein which is involved in the phototropism of the plant. For VVD after adduct formation the aα-helix and the bβ-strand (at the N-terminus) are released allowing VVD to interact with the transcription factor With Collar-1 (WC-1), inhibiting the synthesis of β-carotenoids under constant illumination. Image modified from reference [170].

A mutation in any of these two cysteins looks like a knockout strain, leading to the loss of function of the protein and avoiding the VVD repression of BL genes expression[147]. VVD is a slow cycling LOV domain, with an adduct mean lifetime between 6,000-10,000 s[147].To elucidate the underlying reason of VVD slow cycling, several engineered mutant versions of VVD have been produced, proving that the electronic flavin environment and solvent accessibility to the flavin binding pocket are factors that regulate the adduct lifetime. Also it has been proved that the addition of small bases as imidazole reduces the adduct mean lifetime[157,158].

Currently, the crystallographic structure of the lit state and dark state of VVD are known[169,147].However, it seems that in solution VVD acquires a third state. This third state is a loose dark state conformation different from the crystallized dark state[168], so it is proposed that in solution and in dark conditions VVD alternates between a closed and open conformation[171].

Until now, it is not fully understood: how is VVD involved in the regulation of many biological processes?, how do the external factors modify the adduct stability?, how many intermediate states are visited by VVD?, how is the dynamic of the conformational change?, which is the redox potential of the flavin in the VVD context?, and as a general question for all flavoproteins, how does VVD regulate the reactivity of its flavin cofactor with molecular oxygen?. All these questions have to be answered to fully understand the light perception mechanism of VVD and also to improve biotechnological applications of VVD as part of the optogenetic toolkit.

4.5 The ENVOY protein

For the ENVOY protein in *T. atroviride* (TaENV1), reports of the protein purification and characterization of its photocycle are missing. Sequence comparison shows that TaENV1 does not present the Jαhelix motif as AsLOV2. Instead, it presents the sequences for the two motifs aα–helix and bβ–strand, which support the idea of a light activation mechanism similar to VVD (Figure 4-9).

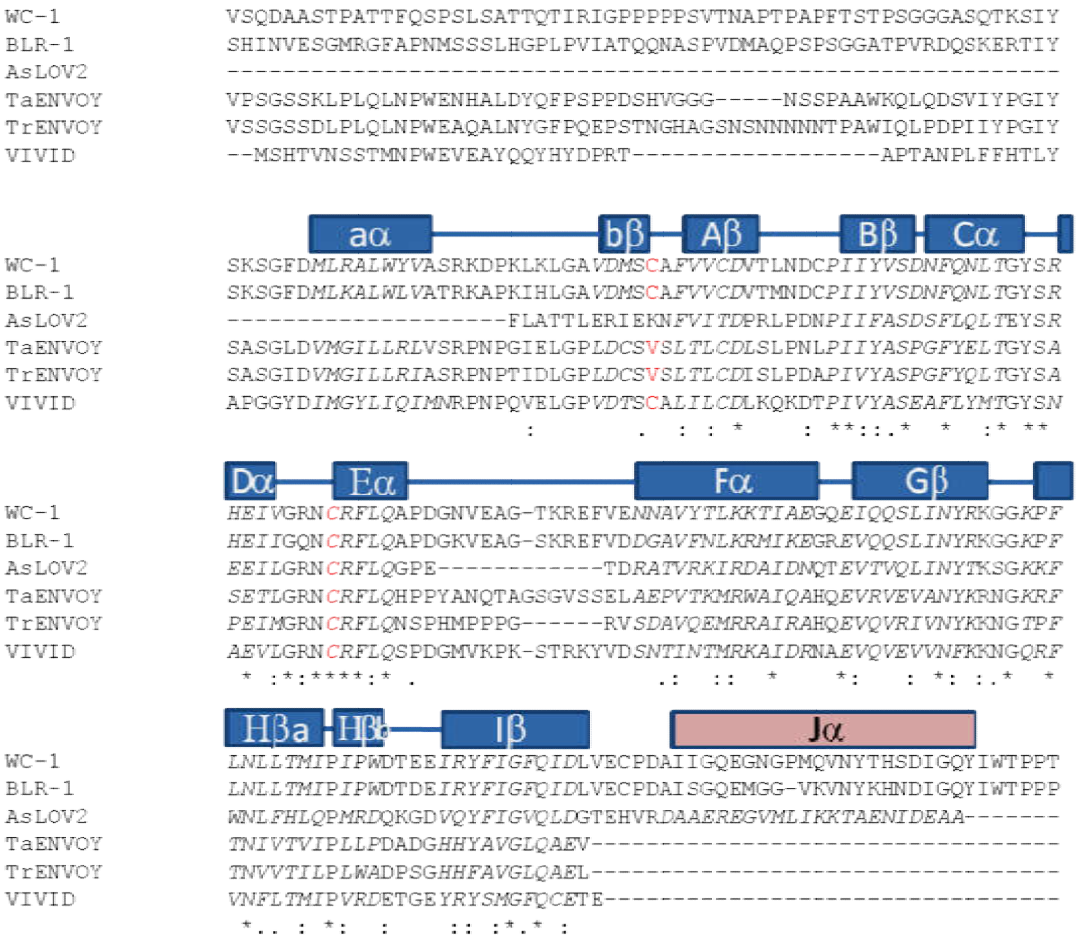

Figure 4-9. ENVOY alignment and motif identification. Alignment of LOV domains present in *N. crassa, T. atroviride*, *T. ressei* and *A.sativa*. Blue boxes correspond to domains reported for VIVID, the red box is the C-terminal Jα helix of AsLOV2. Amino acids in red are the highly conserved adduct cysteine (C108 in VVD), and the cysteine hinge (C71 in VVD). The additional amino acids necessary for accommodation of FAD moiety are between the Eα and Fα motifs

For the close related fungus *Trichoderma ressei*, the homologous protein ENV1 (TrENV1) has been recently studied and its activation mechanism and crystallographic structure have been reported[172,173]. TaENV1 presents a 62% identity with TrENV1 and a 59% identity with VVD. Meanwhile, TrENV1 presents a 57% identity with VVD (Figure 4-9), and even the high identity level TrENV1 gene could not compensate for the lack of VVD gene[174] in *N.crassa*, suggesting

significant differences in the photoperception mechanism between these LOV domains.

Recently, TrENV1 was expressed and purified using the Glutathione S-Transferase (GST) protein as a tag to increase TrENV1 solubility. Purified TrENV1 presents the characteristic absorption profile of a LOV domain, and its crystallographic structure resembles VVD structure more than the AsLOV2 structure (Figure 4-10). However, TrENV1 binds FMN instead of FAD which correlates with the shorter amino acids sequence between the Eα and Fα motifs, which are necessary for the accommodation of FAD moiety (Figure 4-9). Interestingly TrENV1 turns to be sensitive to oxidative conditions due to the oxidation of a thiol group of a cysteine (Cys96)[175]and is also sensitive to osmotic stress conditions through a threonine (Thr101) which is involved in recruiting water molecules in the LOV active site[172].

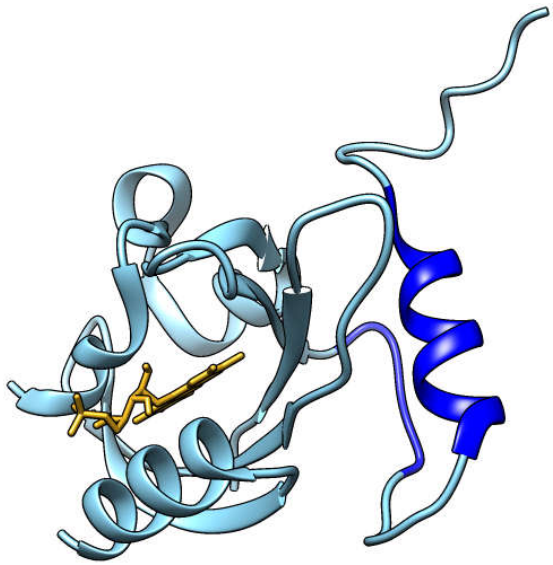

Figure 4-10. Crystallographic structure of TrENV1. As VVD, this protein presents the aα-helix and bβ-strand motifs (dark blue) at the N-terminus of the LOV domain (light blue), but unlike VVD, TrENV1binds as cofactor FMN (yellow) instead of FAD. PDBID: 4WUJ[175].

The natural sequence variations among different LOV domains can become a powerful resource to explore and fully understand the mechanism of light perception at a molecular level, and can also be used to identify additional functions of the LOV domains as C96 and T101 in TrENV1 which are not

conserved in VVD. Furthermore, it has been proved that some punctual key mutations can modify LOV domains functioning (for example the C71A mutation in VVD[147]) or can be tolerated by the LOV domains (C71V of VVD[147]). All of the above highlight the importance of studying diverse LOV domains. The LOV domain TaENV1 provides a natural sequence variation of LOV domains which can act together as a photoreceptor, and also provides an opportunity to learn about possible functionality of specific amino acid variations.

4.6 Protein aggregation

Even when the biological function of proteins is performed within their native state, this conformation is marginally stable, only 5-15 kcal/mol above the unfolded state[176], making proteins native state susceptible to disruption by external factor or even by intrinsic fluctuations under physiological conditions[177].

If a native protein is damaged, it generally turns to a misfolded conformation. *In vivo* such a misfolded protein may be subjected to (i) chaperone-mediated refolding back into the native conformation, (ii) ubiquitination and subsequent degradation by the proteasome, (iii) cleavage or (iv) **protein aggregation (PA)**[178,179]. *In vivo* PA is a trait of loss of protein homeostasis[180] and it has been linked to aging and human health problems as prion diseases, Alzheimer and Parkinson diseases [180,181]. I*n vitro* loss of protein stability can only lead to protein cleavage or aggregation which are common limiting steps for recombinant protein research and for the development of therapeutic proteins[182,183].

PA occurs due to the loss of the well-folded or native state, which induces the development of intermolecular interactions between non-native proteins and leads to the formation of stable aggregates where the biological function of proteins is impeded[184]. These intermolecular interactions are largely driven by hydrophobic forces that induce the formation of amorphous aggregates or can lead to the formation of highly ordered fibrillar aggregates called amyloid[185]. These aggregated states turned out to be more stable than the native conformation, thus proteins can barely be recovered from the aggregated state to their native and functional conformation (Figure 4-11). Recently, it has been proposed that PA is a common

cellular process and a generic feature of all the polypeptide chains[181], highlighting its central role in all protein related processes.

Current studies over protein aggregation are focused on the factors that trigger the aggregation, factors that can avoid or stop the aggregating process, and in the aggregation kinetics and underlying mechanism of aggregation. Lot of studies on PA are related to amyloid aggregation due to its clear role in health problems and its characteristic highly ordered structure of stack β-sheet. However, the main questions about protein aggregation are the same no matter if amorphous or amyloid aggregation takes place.

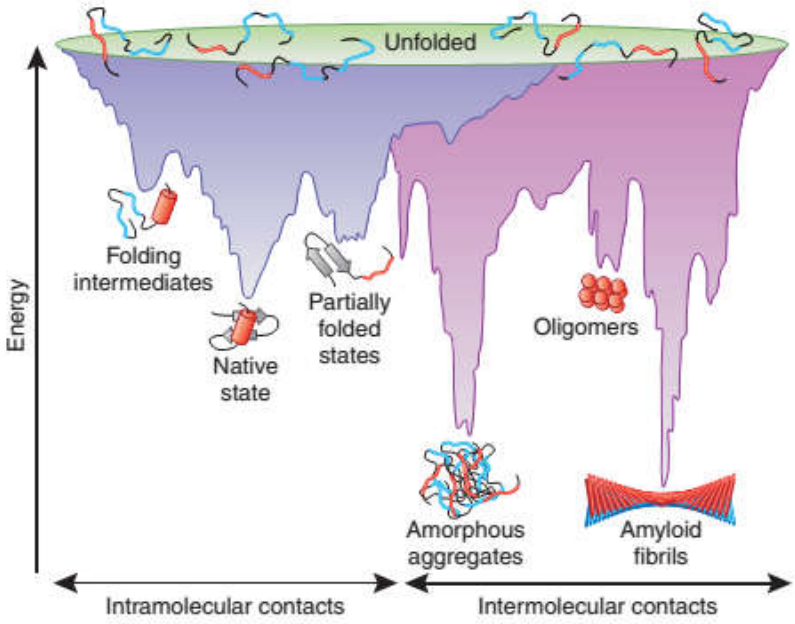

Figure 4-11. Protein energy landscape. Protein native state is only marginally stable and this state can be disrupted by external factors of fluctuations, sending the protein to a partially unfolded state from where other states as amyloid fibrils or amorphous aggregates are accessible. Image reproduced from reference [185]

PA kinetics is usually tracked by turbidity assays, ThioflavinT fluorescent probe (which bind to amyloid fibrils) or by Congo Red dye (which exhibits an absorbance shift when binds to amyloid aggregates)[186], but last two methods are ineffective when PA different from amyloid is being studied. For amyloid aggregation its

kinetics reflects a nucleated self-assembly reaction that displays a sigmoidal growth, with a lag phase, an elongation phase and a plateau phase, and several microscopic models have been proposed to fit the macroscopic aggregation kinetics measured parameters[187].

It is important to note that *in vitro* PA is usually triggered by disrupting the protein native conformation through the addition of denaturant molecules, addition of oxidizing agents, temperature or pH increments, which are external factors and do not reflect the physiological conditions tested by the protein. Since aggregation can also occur even under less harsh conditions lately aggregation of proteins under physiological conditions has become a more convenient model system to understand PA[188].

4.7 Protein oxidation

In vitro as *in vivo* osmotic stress, **oxidative stress**, and heat shock are factors that disrupt protein native state enhancing its unfolding and possible aggregation. Oxidative stress is defined as a disturbance in the balance between the production of ROS and antioxidant defenses[189], this loss of ROS homeostasis has toxic or even deadly effects for cells[190]. ROS can induce **protein oxidation** with the side effects of covalent modifications over the proteins, cleavage of the polypeptide chains or modifications of the amino acids lateral chains[191–193]. In any case, the stability of the protein is disrupted and protein degradation or PA can be expected.

In vivo, oxidative modifications of proteins are not repaired. Instead, mildly oxidized proteins are selectively recognized and degraded by the 20S proteasome complex. However, during oxidative stress the 20S proteasome is inhibited[194], and the protein degradation pathways get overloaded, leading to protein aggregation (PA). It is known that the level of oxidized proteins, as the level of aggregated proteins, increases with aging and in a number of human diseases. However, the accumulation of oxidized proteins is a complex function of the rates of ROS formation, antioxidant levels, and the ability to degrade oxidized forms of proteins[138,195,196]. Therefore, even when protein aggregation and protein oxidation seems to be part of the same biological process, it is unclear which part of the

process is the most toxic for the cell, the proteins aggregation or the proteins oxidation.

In vitro, intentional ROS oxidation of proteins is usually performed by metal ion-catalyzed reactions (Fenton's reaction), and it has been proved that oxidation leads to cleavage of the polypeptide chain of proteins, formation of cross-linked proteins, and can lead to an increase in hydrophobic surface exposure, enhancing intermolecular interactions and PA[196,195,197,191–193]. Metal ion-catalyzed reactions are not the only possible source of ROS, off-pathway reaction in flavoproteins can also lead to ROS production.

One of the most documented off-pathway reactions of flavoproteins occur in the mitochondrial respiratory chain, where the leaking of electrons is an important source of intracellular ROS[198]. However, it has been proved that the production of ROS is not substantially diminished in mutants lacking respiratory enzymes, which led to the conclusion that ROS can be produced by other non-respiratory flavoproteins [199,200], and flavin-binding photoreceptors are feasible producers of ROS, since they bind a photosensitizer molecule as a cofactor and its biological function implies exposition and absorption of BL.

4.8 Side effects of blue light and molecular oxygen

Although BL is used for photosynthesis and as a cue for the diverse biological responses, it has deleterious side effects and has been related to increasing intracellular ROS[201,202]. Unlike UV radiation, BL by its own is barely capable to producing cellular damage or ROS, but photosensitizer molecules as flavins are capable to absorb BL and react with molecular oxygen producing ROS (see Section 4.2).

Recently it has been proved that a CRY photoreceptor in plants is a source of ROS[203], and for LOV domains it has been proved that an engineered version of the AsLOV2 named miniSOG (mini Singlet Oxygen Generator) can react with molecular oxygen, producing $^1O_2$[204]. Other genetically encoded photosensitizer proteins that produce $^1O_2$ have been reported, as KillerRed, SuperNova and Pp2FbFP L30M proteins. Together they cover the spectral range from 430 to 590

nm that can be used for $^1O_2$ production[205,206].Genetically encoded photosensitizers, as miniSOG or KillerRed, have been used to induce local oxidative stress within a cell and to kill cell populations in photodynamic therapy[207], so it turns feasible that a self-oxidation of the photosensitizer proteins could take place. However, in any case, the deleterious effects of the ROS over the photosensitizer protein itself have been reported.

4.9 Results

This section presents the unpublished data of the photochemical characterization of the LOV domain TaENV1 and the preliminary results for recombinant expression of the LOV domain of BLR-1. Also, the submitted manuscript **Hernández Candia CN**, Casas-Flores S, Gutiérrez-Medina B (2017) "*An alternative light response of a LOV photoreceptor triggers self-induced aggregation"* The Journal of Biological Chemistry, is summarized.

4.9.1 Abstract

Blue light perception in the filamentous fungi *N.crassa* and *T. atroviride* is performed mainly by flavin-binding LOV domain photoreceptors. Herein the homologous single LOV domain proteins VVD and ENV1 (from *N.crassa* and *T. atroviride*, respectively) are studied. For VVD, its *in vitro* aggregation under physiological conditions was linked to the photosensitized functioning of its flavin cofactor. The underlying mechanism of *in vitro* VVD aggregation was established in a comprehensive way. Briefly, VVD has a probability to perform its standard flavin-cysteine adduct or to act as a photosensitizer, producing singlet oxygen that oxidizes diverse amino acids in the inside of the protein. Protein oxidation disrupts VVD conformation and triggers its partial unfolding, thus VVD hydrophobic regions get exposed and intermolecular interaction of partially unfolded VVD proteins leads to an amorphous aggregated state. VVD protein turns out to be sensitive to light, oxygen, and temperature (LOT) cues, integrating environmental information through modifications in the aggregation extent of the protein. We propose that this self-oxidation and aggregation mechanism is a possibility for other flavin-binding photoreceptors and it is feasible that VVD self-oxidation also occurs *in vivo*, directly

modifying the BL responses of *N. crassa*. Regarding to the TaENV1 protein, its recombinant expression and purification were achieved and its photocycle was measured for first time, showing that TaENV1 is a slow cycling LOV domain, which as other fungal LOV domains, is barely soluble. All these results contribute to understand the diverse molecular processes that take place in LOV domains.

4.9.2 Motivation

For the VVD studies presented herein, motivation emerged from a persistent observation of *in vitro* VVD aggregation. After proper control experiments we concluded that aggregation was part of the protein traits, thus we found an opportunity to explore PA under physiological conditions in a well characterized BL photoreceptor.

The study of TaENV1 protein and the LOV domain in BLR-1 presents an opportunity to increase the amount of functional characterized fungal LOV domains, increasing the known pool of functional amino acid variations that LOV domains tolerate.

4.9.3 VIVID aggregation

The VVD protein, a version N-terminally truncated by 36 residues and tagged at the N-terminal with a 6xHis tag (6xHis-VVD) (plasmid kindly provided by Dr. Brian R. Crane, Cornell University), was expressed under the same conditions reported on literature and the adduct formation was confirmed with the absorbance spectrum of the lit and dark states. Unexpectedly, a shift in the absorption spectrum was repeatedly observed. This shift was aggravated at high concentrations, so concentrations lower than 1 mg/ml were used, however the absorbance shift was still present (Figure 4-12A). Increased turbidity in the purified VVD sample was due to PA and Transmission Electron Microscopy (TEM) showed that under native conditions VVD presented amorphous aggregation (Figure 4-12B).

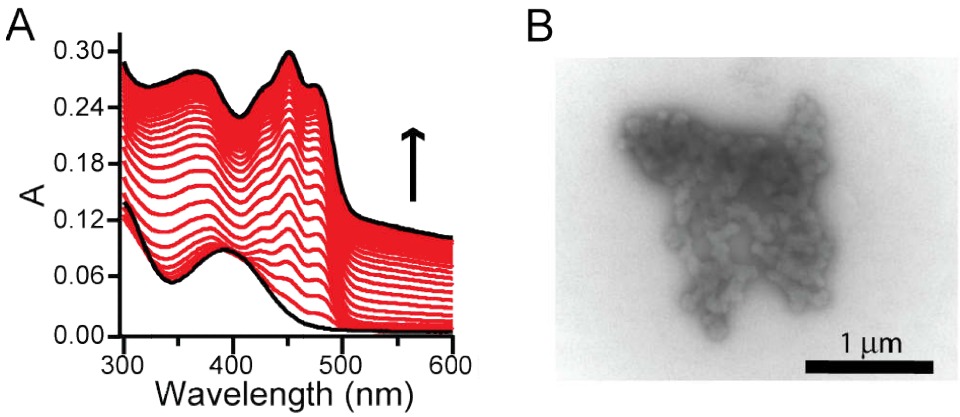

Figure 4-12. VVD absorption shift is due to formation of an amorphous aggregate. A) Absorbance (A) spectra of VVD at standard buffer conditions (25°C, 10% glycerol, 50 mM HEPES, 150 mM NaCl, 20 mM imidazole, pH 8) acquired every 30 minutes after a BL pulse. First and last spectra are shown in black. Arrow shows spectra changes with time. B) TEM of VVD sample with absorbance shift show amorphous aggregation.

We observed that on its aggregated state VVD losses its yellowish hue implying that the non-covalently bound flavin cofactor was released via a partial unfolding of the protein, which could be avoided by addition of the osmolite glycerol and by the chaperon like protein Bovine Serum Albumina (BSA) (Figure 4-13).

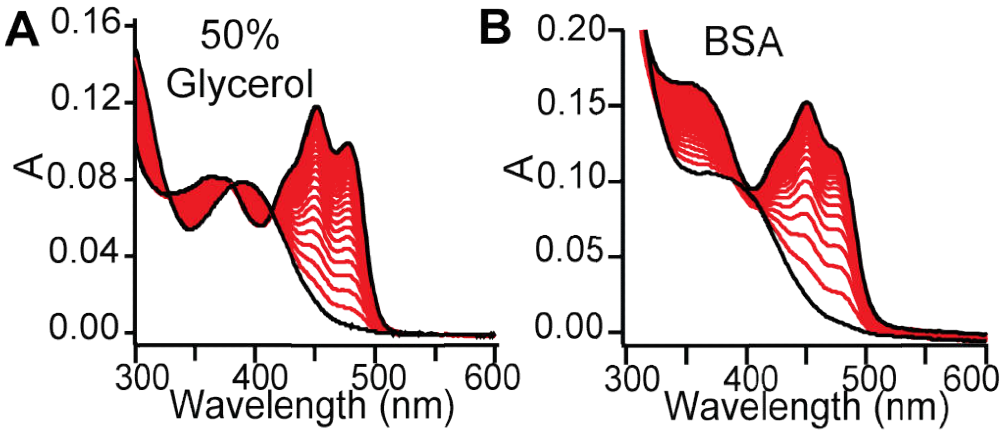

Figure 4-13. Partial unfolding and VVD aggregation are avoided by Glycerol and BSA. A) Addition of the osmolite glycerol fully avoids protein aggregation. B) Addition of BSA avoids VVD aggregation. First and last spectra are shown in black.

Aggregation occurred at native conditions, thus the VVD stability is disrupted by no extreme conditions. We tested the effect of repetitive BL pulses and the effect of

different temperatures. We observed that turbidity increased proportionally to the number of BL pulses applied (Figure 4-14A). Meanwhile, the final aggregation after 4 hours depended on the sample temperature, displaying a sigmoidal behavior with a half-temperature around 25°C (Figure 4-14B). Arrhenius plot of VVD adduct mean lifetime as a function of temperature confirmed that adduct decay is a thermally-driven process, with an activation energy of 18 ± 0.4 kcal/mol (Figure 4-14B).

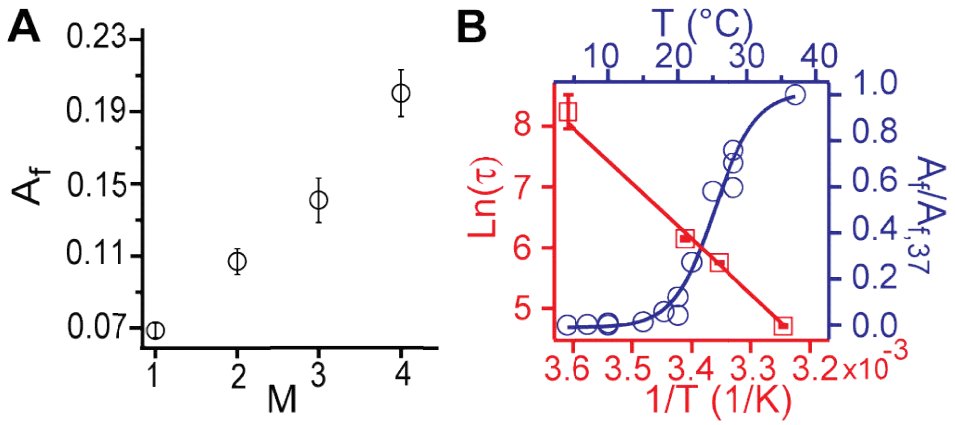

Figure 4-14. Light and temperature participate in the aggregation of VVD. A) The effect of light on aggregation. BL pulses were applied to VVD samples every 48 min. The final absorption at λ=550 nm (A*f*), measured after protein incubation over 800 min, as a function of the number of pulses (M) indicates that BL promotes aggregation (mean ± SD, N=3). B) (Blue) The amount of VVD aggregation as a function of temperature (T) was quantified by incubating VVD samples at different temperatures over 4 h and then measuring absorption at λ=550 nm (A*f*). The data point at 37°C(A*f*,37) was used to normalize all data. Data were fit to a sigmoid function (blue line), yielding a half-temperature $T_{1/2}$=25.3 ± 0.5°C.(Red) Arrhenius plot of VVD adduct mean lifetime.

Since VVD is a flavin-binding protein, photosensitizer activity and ROS production was a possible triggering event of PA. First we identified the presence of carbonyl groups, a standard marker of protein oxidation, in aggregated VVD samples (Figure 4-15A). Tandem mass spectroscopy (MS/MS) corroborated oxidation of at least 5 amino acids, two of which (F92 and N161) are not exposed to the solvent (Figure 4-15B), thus supporting an inside out production scheme for the oxidizing species. We concluded that VVD loss of stability and partial unfolding is due to protein oxidation. To avoid oxidation an O_2 scavenger system was tested, fully

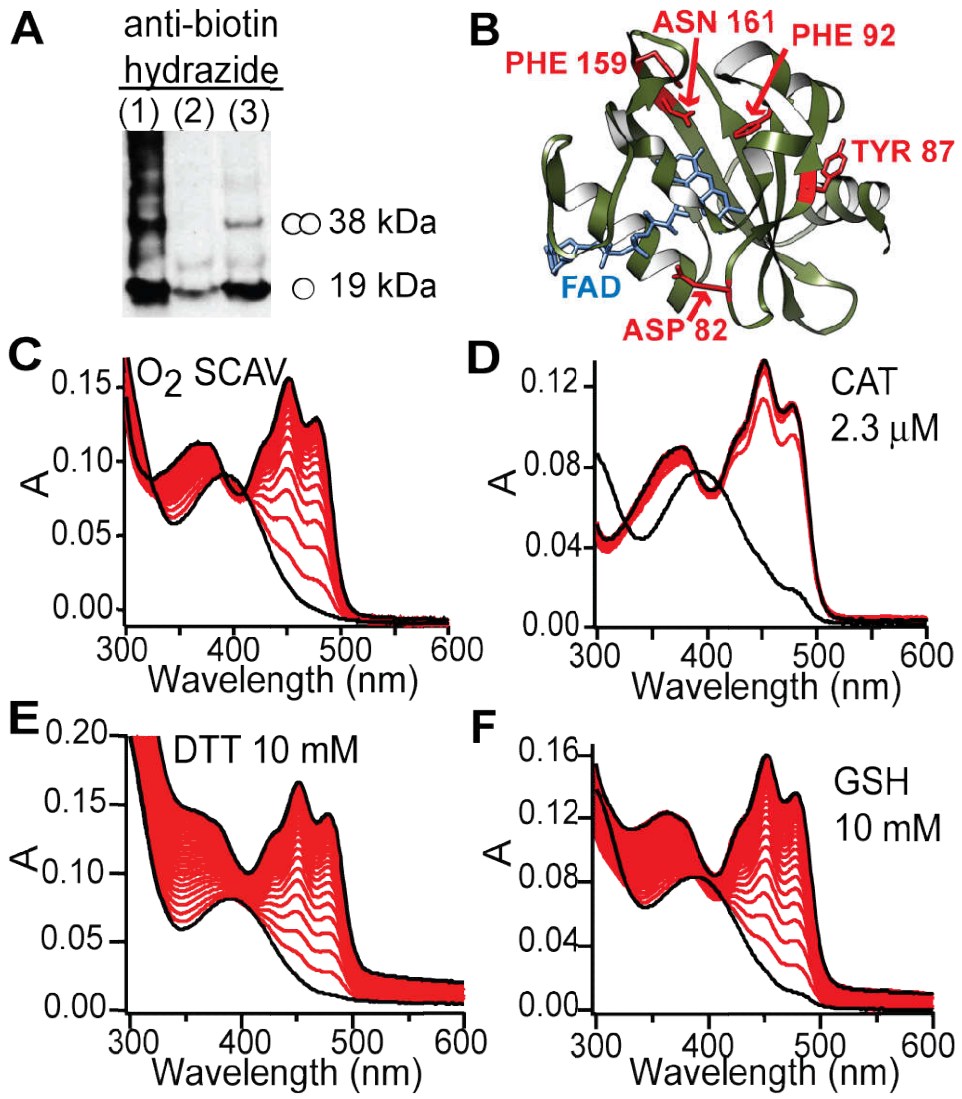

Figure 4-15. VVD gets oxidized by self-produced singlet oxygen. A) Detection of oxidized proteins by western blot against biotin-hydrazide in labeled samples. On each well 5.6 μg of protein were loaded. Lane1: VVD intentionally oxidized using 33 mM H_2O_2 and 1.5 mM $NiCl_2$. Lane 2: unaggregated VVD. Lane 3: aggregated VVD. B) The 3D structure of VVD in the dark state (Protein Data Bank 2PD7) shows various oxidized amino acids (red) as detected by mass spectrometry. C) Removal ofO_2 using an oxygen scavenger system (20.5 μM glucose oxidase, 70 nM catalase, 69mM glucose) fully avoided aggregation. The corresponding adduct mean lifetime was τ = 175 ± 2 min (τ± error from the fit). D) Addition of catalase (2.34 μM) avoided aggregation, and shortened the adduct mean lifetime to τ = 17.8 ± 0.6 min (τ± error from the fit). The addition of singlet oxygen scavengers DTT (E) and GSH (F) also avoided aggregation. In C-F first and last absorption spectra are shown in black, and data were acquired every 30 min.

avoiding VVD aggregation and supporting the hypothesis of VVD as a photosensitizer protein (Figure 4-15C). Diverse ROS scavengers were tested, but only singlet oxygen scavengers DTT and GSH proved to be effective avoiding aggregation (Figure 4-15E&F). Interestingly, catalase modifies VVD adduct mean lifetime and avoids VVD aggregation (Figure 4-15D).

To discard that the aggregation process in VVD was due to metal ion-catalyzed production of ROS a VVD protein truncated by the first 36 amino acids and tagged at the N-terminus with a 6xHis tag and at the C-terminus with a 15 amino acid sequence, named Biotin-tag[208], was expressed. The Biotin-tag binds a biotin molecule, allowing the purification of the protein 6HIS-VVD-Biotin through an Avidin resin, fully avoiding the exposition of the protein to nickel ions during the purification step. The absorption spectrum of the purified 6HIS-VVD36-Biotin protein was obtained, showing the flavin-cysteine adduct formation and the thermal recovery of the protein to the dark state. Also, the same absorbance shift observed for the VVD protein purified through Ni affinity chromatography was observed. Furthermore, VVD protein was passed through a chelex resin which binds metal ions and also desferal, which binds to free iron, was tested. None of these cautions avoid VVD aggregation supporting the idea of ROS produced by VVD and not by external factors.

Based on our data we proposed a model for VVD aggregation pathway (Figure 4-16). Exposure of functional VVD in the dark state to BL induces formation of a flavin triplet state, from where two possibilities follow: a flavin-cysteine adduct is formed (standard photocycle) or $^1O_2$ is produced in the presence of O_2 (ROS path). In the ROS path $^1O_2$ oxidizes VVD and triggers the aggregation route. Oxidation of VVD leads to an intermediate state characterized by partial unfolding that releases the flavin cofactor and exposes buried hydrophobic regions. In this partially unfolded state, hydrophobic and covalent inter-molecular interactions help produce oligomers which act as nucleation centers that initiate production of a macroscopic aggregated state. Addition of glycerol or BSA avoids loss of protein structure, preventing exposition of hydrophobic regions and stopping the path to aggregation. The presence of O_2 scavenger or $^1O_2$ scavenger avoids aggregation by preventing

production of $^1O_2$ or by removing already produced $^1O_2$, respectively. Every time VVD is exposed to BL (a trial), it has probability to follow the off-pathway ROS cycle or to produced the flavin-cysteine adduct. Therefore, light affects the probability of aggregation by influencing the number of trials or the time between trials. Even when $^1O_2$ was already produced, in a second trial adduct can occur stabilizing the protein conformation until thermal adduct decay happens. Thus low temperatures diminish adduct decay rate and retain VVD conformation longer, even if the VVD protein was already oxidized.

Regarding catalase effect, unexpected modification of the VVD adduct decay rate suggests that catalase did not act as a conventional hydrogen peroxide scavenger to prevent the aggregation of VVD. However, the VVD-catalase interaction mechanism remains as an open question.

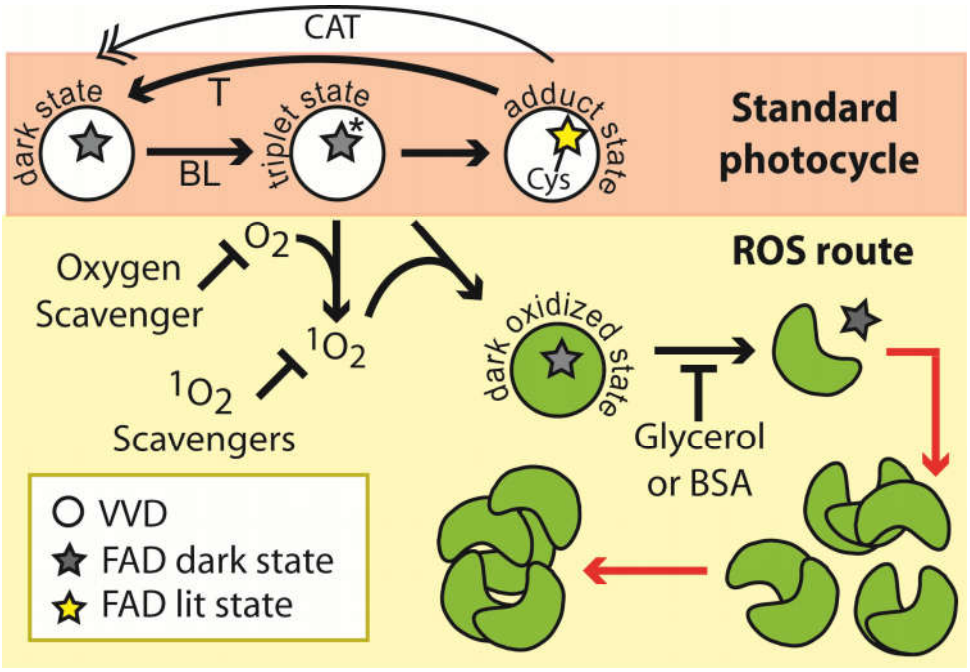

Figure 4-16. In response to blue-light VIVID follows an alternative pathway that triggers its self-induced aggregation. Photosensitizer activity of VVD leads to an unconventional pathway where singlet oxygen ($^1O_2$) is produced, oxidizing the protein and inducing its partial unfolding which leads to protein aggregation.

4.9.4 Conclusions

We propose that PA, instead of just being an end-point for misfolded and damaged proteins, could work as a molecular mechanism for simultaneous integration of diverse environmental cues regulating protein availability, thus regulating its biological function. In this regard, multi-factorial nature of PA could be useful in complex processes as circadian rhythms, where integration of several environmental cues is required to maintain stable rhythmicity.

In *N. crassa*, as in other fungi, circadian rhythm is entrained by light, temperature, and cellular redox states[209,210]. However it is not clear how all these factors are simultaneously integrated. On the other hand, VVD has been shown to take part in regulating various circadian clock properties, most likely through its effects on the WCC. In *N. crassa* VVD aggregation could work as an integrative node for multiple cues, diminishing VVD effective concentration and limiting VVD repression of the transcription factor WCC.

Surprisingly, catalase avoids the aggregation of VVD with concomitant shortening of adduct mean lifetime. One possibility is that as $^1O_2$ is produced catalase acts as a $^1O_2$ scavenger by getting oxidized[211], thus sparing VVD. However, this mechanism does not explain changes in the adduct lifetime. Another possibility is that catalase interacts directly with the photoadduct, avoiding the production of damaging $^1O_2$. Here, a redox reaction between the lit-reduced flavin cofactor and catalase could return the flavin to its dark-oxidized state with the accompanying reduction of the heme group in catalase. Supporting this idea, when H_2O_2 concentrations are low, catalase two-step catalytic cycle can stall with the heme in its oxidizing form, and can abstract electrons from the surrounding[200].

Our results show that self-oxidation and consequent PA occurred in VVD, and both are feasible processes for other LOV domains or photosensitizer proteins. Self-oxidation of photosensitizer proteins can account for its disposal either by degradation or by PA and it is a process that has to be considered for recombinant protein purification, optogenetic application, and should be considered in the functioning scheme of the photosensitizer proteins.

4.9.5 Unpublished Data

VVD size-exclusion chromatography

To test if in our hands the purified VVD protein presents the reported light triggered conformational change[147] Size Exclusion Chromatography (SEC) assays were performed. Purified protein was injected to a 75 superdex column (resolution range 3,000 Da to 70,000 KDa) in a buffer of high ionic strength (20 % glycerol, 300mM NaCl, 50mM HEPES, pH8) and a flow condition of 0.5 ml/min. VVD was injected in two different conditions: 1) dark condition, where care was taken to avoid as much as possible sample illumination and 2) lit conditions where the sample was illuminated for 15 min with blue light prior to injection (Figure 4-17B). The elution profile showed two peaks and the presence of the protein around the 14 ml elution fraction was confirmed by SDS-PAGE electrophoresis. For the dark state VVD is expected to elute as a protein of ~19 kDa, and in its open conformation the expected apparent molecular weight is ~33 kDa[147].Also SEC was performed for the 6HIS-VVD-BIOT protein (Figure 4-17 C).

Both elution profiles presented a clear change in response to BL, but the differences we observed among the lit and dark elution profiles do not correspond to the expected change. For the lit condition the main peak eluted in fraction ~14 ml corresponding to the expected molecular weight of ~19 kDa.

Under dark conditions SEC shows a main peak that corresponds to a molecular weight of 1.35 kDa or lower (around elution volume 18 ml), but protein was not observed in SDS-PAGE. We concluded that flavin cofactor released from the LOV domain elutes in this fraction since flavin presents a high absorption around 280 nm, its molecular size is 785 Da and no protein signal was observed in this elution fraction by SDS-PAGE. SEC results are in agreement with our proposed model for VVD aggregation where the flavin cofactor is only released after the flavin-cysteine adduct decay, thus in the lit conformation the native conformation is retained and the flavin cannot be lost.

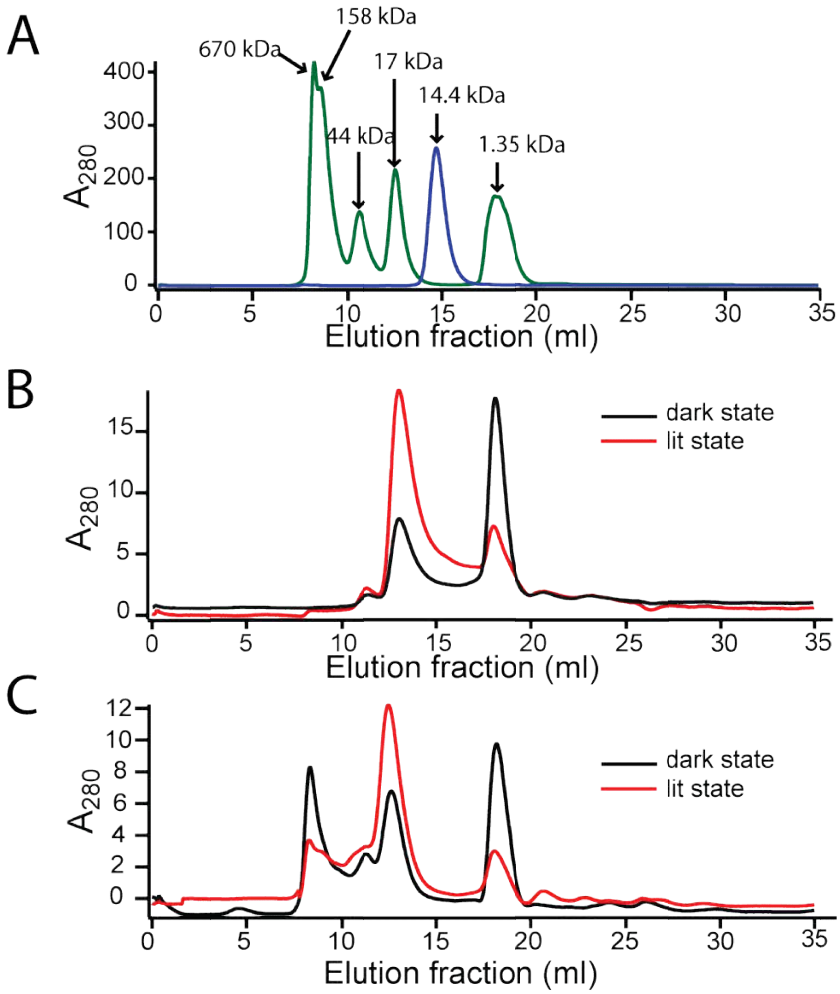

Figure 4-17. Elution profile of a SEC in dark and lit conditions for the VVD protein. Elution profiles of the dark and lit states obtained with the Superdex75 column at a constant flow of 0.5 ml/min. A) Calibration of the Elution profile. In green line is the elution profile of the gel standard filtration marker of BioRad. In blue line is the elution profiled of purified lisozima. B) SEC elution profile of VVD protein in dark and lit conditions. C) SEC elution profile of 6HIS-VVD36-Biot protein in dark and lit conditions

TaENV1 and BLR-1 LOV domains

We designed two molecular constructs: the LOV domain of BLR-1 and TaENV1, both of them were tagged with a GST domain at the N-terminus and with a 6xHis tag at the C-terminus. The selected sequences of the corresponding LOV domains in BLR-1 and ENV1 were chosen after an alignment of the LOV domains present in AsLOV2, BLR-1, ENV1, WC-1, and VVD, taking into account that a truncated version of VVD has shown to be more stable. For TaENV1 the first 49 amino acids

were deleted and for the LOV domain in BLR-1 the selected sequence starts in the amino acid I320 and ends in the amino acid I473.Doubled tagged TaENV1 protein was named GST-ENVOY-6HIS and the double tagged BLR-1 protein was named GST-BLR1LOV-6HIS. Both proteins were expressed in BL21(DE3) strain in the same conditions than VVD (Optical density 0.6, 18°C, 100 μM IPTG, over 22 h).

First purification was performed by Ni affinity chromatography. However, PAGE-SDS showed a strong induction for both constructions and low recovery of purified proteins at the elution step (Figure 4-18).Two problems were noticed, first for both constructions most of the protein remained in the pellet fraction restricting the amount of purified protein available. Secondly, the LOV domain protein was not retained by the Ni resin during the washing steps and a protein of ~25kDa was co-purified with both LOV domain proteins.

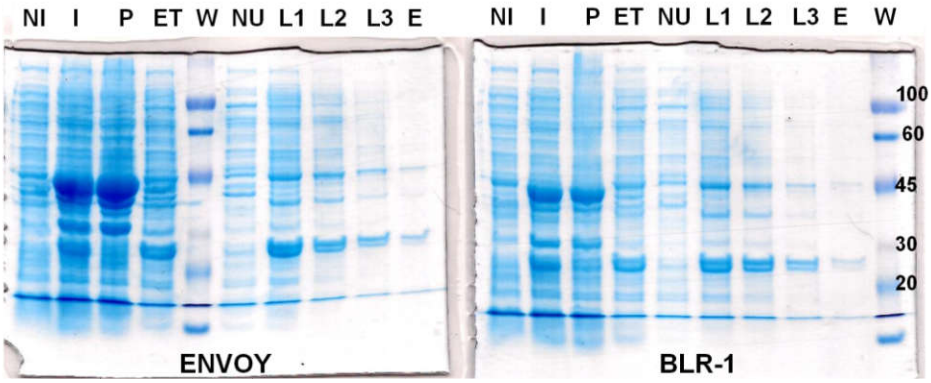

Figure 4-18. Expression and purification of GST-ENVOY-6HIS and GST-BLR1LOV-6HIS.SDS-PAGE for the purification of both proteins through their 6xHis tag. (NI) Not induced, (I)Induced, (P)Pellet, (ET) Total Extract,(W)Molecular weight, (NU) Not bound to the Ni-agarose resin after 1 hr of incubation, (L1) First wash, (L2) Second wash, (L3)Third wash, (E) Elution. For the double tagged TaENV1 protein the expected molecular weight is 43.8 kDa, and for the double tagged LOV domain in BLR-1 the expected molecular weight is 44.6 kDa.

To increase the amount of soluble protein, different expression and purification conditions were tested. Purification through the GST tag allows a higher yield of purified GST-ENVOY-6HIS protein (Figure 4-19A). None further work has been done with the LOV domain BLR-1 construction.

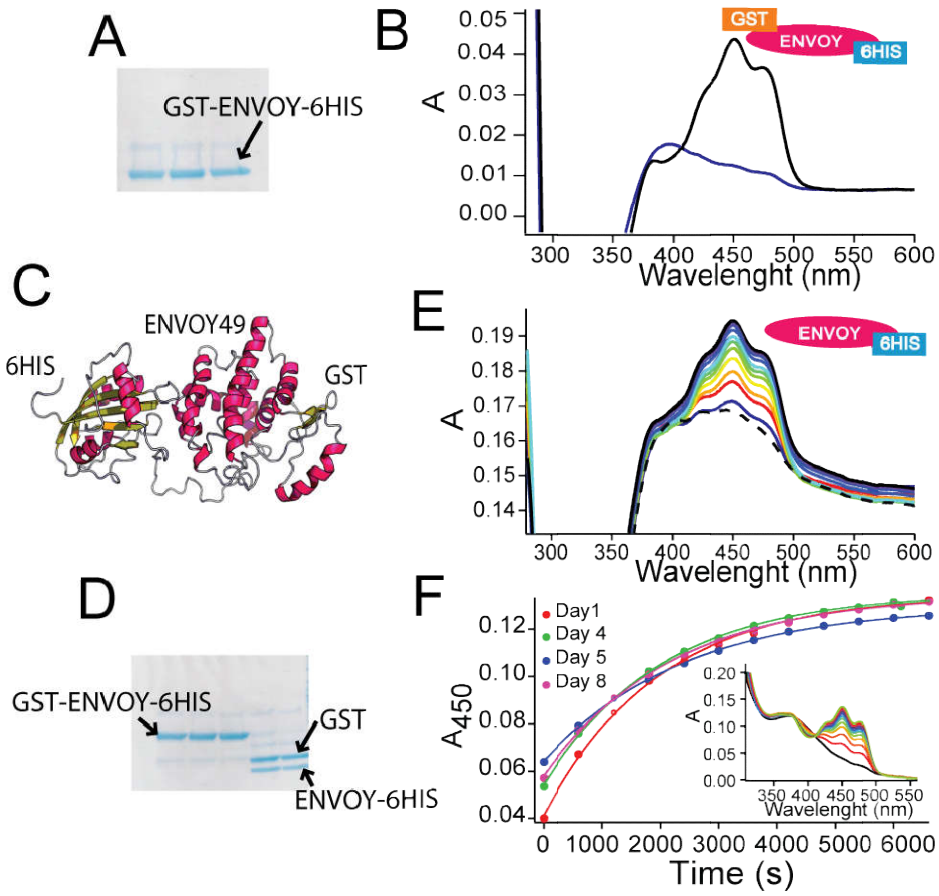

Figure 4-19. GST-ENVOY-6HIS protein is a partially soluble, and a slow cycling LOV domain that oligomerize in response to BL.A) PAGE-SDS of the elution fraction of the GST-ENVOY-6HIS protein purified via a Glutathione resin. B) Absorption spectrum of GST-ENVOY-6HIS. Black line represents the dark state and blue line represents the lit state after 10 minutes illumination. C) GST-ENVOY-6HIS protein predicted structure using RaptorX server. D) The GST tag was cleavage with thrombin. PAGE-SDS gel shows that digestion was complete. E) Absorption spectrum of ENVOY-6HIS. Blue lines represent the lit state after 10 minutes illumination. Rainbow colors represent the profiles at different recovery times. F) Adduct recovery kinetics of diverse samples measured as the recovery absorbance at 450 nm after a BL pulse. Exponential flavin-cysteine adduct decay are shown. (Insert) Characteristic absorption spectrum, in dark the adduct state and in colors the recovery traces taken every 10 minutes.

To prove the flavin-cysteine adduct formation in the GST-ENVOY-6HIS protein the absorbance spectrum of the lit and dark states were measured, getting an absorption profile that corresponds to a fully oxidized flavin under dark conditions and fully reduced flavin after BL illumination (Figure 4-19B).

Since the size of the GST protein is comparable to the size of the TaENV1 LOV domain (Figure 4-19 C), we were worried about some possible effects of the GST tag over the light response of the LOV domain. The GST tag from the purified GST-ENVOY-6HIS protein was cleavaged with thrombin (Figure 4-19 D) and the spectrum from this GST-free protein was obtained. It is noticeable that 10 minutes of illumination with BL was not enough to bring all of the sample to the lit state, since the peaks between 400 -500 nm were not completely gone (Figure 4-19 E).

To prove that TaENV1 photocycling was a reproducible result, several purifications of the GST-ENVOY-6HIS protein were performed and their absorbance spectrum were recorded, showing always the expected bleaching at 400-500 nm after a BL pulse and the exponential adduct decay. The adduct mean lifetime of TaENV1 was estimated from the absorbance at 450 nm (Figure 4-19 F) for different protein purified batches. In all the cases, adduct mean lifetime was in a range between 1362 s and 1690 s, making TaENV1 protein a member of the slow cycling LOV domain subclass.

Size-exclusion chromatography (SEC) was performed with the purified GST-ENVOY-6HIS protein to know if the protein was a homogeneous monomeric sample and to get evidence of the ENVOY's conformational change as it has been reported for VVD LOV domain[147]. The protein was injected to a 200 superdex column (resolution range: 10,000 Da to 600,000 Da) in dark condition and lit conditions where the sample was illuminated for 15 min with BL prior to injection. The dark condition sample showed mainly a single peak, compatible with the idea of a homogeneous population. In contrast, when the sample was illuminated more than one peak appeared, indicating a lit-response oligomerization and maybe an implicit conformational change (Figure 4-20).

Attempting to get a smaller soluble tagged version of TaENV1, instead of using a GST tag, a Biotin-tag was fused at the C-terminus of the truncated version of TaENV1 (first 49 amino acids deleted) and at the N-terminus a 6xHis tag was fused. The double tagged protein was named 6HIS-ENVOY-Biot. Also a complete version of the TaENV1 protein was tagged at the N-terminus with a 6xHis tag and

was named 6HIS-ENVOY. Unfortunately, none of these new constructions gave detectable soluble protein under the induction conditions and extraction buffer tested until now.

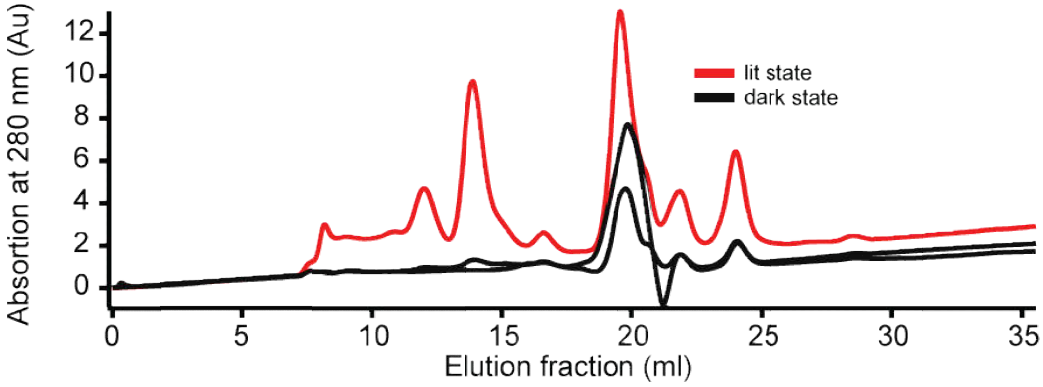

Figure 4-20SEC of GST-ENVOY-6HIS protein. Elution profiles of the dark and lit states obtained with the Superdex 200 column at a constant flow of 0.7 ml/min. Samples were run at 10% glycerol, 300mM NaCl, 50mM HEPES, pH8 and flow rate of 0.7 ml/min.

4.9.6 Novel contributions

For the first time, the side effects of the flavin photosensitizer reactions over a flavin-binding photoreceptor were comprehensively explored, showing that self-oxidation and aggregation are a possibility for these proteins. It was shown that VVD is sensitive to Light, Oxygen, and Temperature, extending the previously known capabilities of this LOV domain and presenting the multi-factorial nature of PA as a possible mechanism to integrate information of diverse environmental conditions into a single outcome. Finally, reduction of the adduct mean lifetime of VVD due to the presence of the catalase protein represents the first report of a protein able to tune a LOV domain photocycle.

Regarding the TaENV1 protein, solubility problems were partially overcame by tagging the LOV domain with a GST protein, and the adduct decay kinetics shows that this protein is a slow-cycling LOV domain.

4.10 Future work

Our data of VVD photosensitizer activity showed that the internal amino acids F92 and N161 get oxidized by the flavin production of $^1O_2$. Currently we are performing

point mutations in these two amino acids, trying to understand how oxidation disturbance propagates from inside out of the protein. Notably TaENV1 and LOV domain in BLR-1 also present solubility problems as it has been reported for TrENV1 and in a lower extent for VVD, suggesting that slow cycling fungal LOV domains have a higher tendency of aggregation. Further studies must be performed to understand if this aggregation propensity correlates with self-oxidation processes similar to what we report for VVD.

Also in a near future single-molecule experiments are proposed. Using our built optical tweezers and the double tagged LOV domains, the dynamic of the light triggered conformational change will be explored. Besides, optical tweezers offers the possibility to explore our proposed VVD self-oxidation unfolding process.

We plan to perform experiments based on the geometry represented in Figure 4-21. The double tagged LOV domain protein will be attached to a micron-sized probe bead, which will be trapped with the laser beam, while the other end is going to be tethered to a dsDNA molecule which in turn will be attached to the surface of the coverslip. While in the dark, controlled mechanical tension will straighten the complex. Then, exposure of the complex to a short pulse of blue light will induce the lit state of the LOV domain. Any conformational changes of the LOV protein will be measured, as they will have the effect of inducing a change in the total length of the ensemble, which can be recorded with high temporal (~1 μs) and spatial (~1 nm) resolution. This proposed experiment is supposed to be the first direct measurement at single-molecule level of a conformational change regulated by light.

To know if the spatial resolution of our instrument will be enough to detect the conformational change some gross estimations were computed letting us to conclude that 1 nm of spatial resolution will be enough. Based on SEC and crystallographic reported data it is possible to estimate an upper and lower limit for the magnitude of the conformational change expected for the VIVID LOV domain. For the lower limit, it has been reported that in a SEC the lit and dark states elute at different fractions, where the lit-state shift corresponds to a 14.2 KDa increment

respect to dark state[147]. Since all proteins have approximately the same density, about 1.36 g/cm3, and assuming that the protein has an spherical shape the radius for the dark state protein is R_{min}=1.7 nm (18.2 kDa) and the radius for the lit state

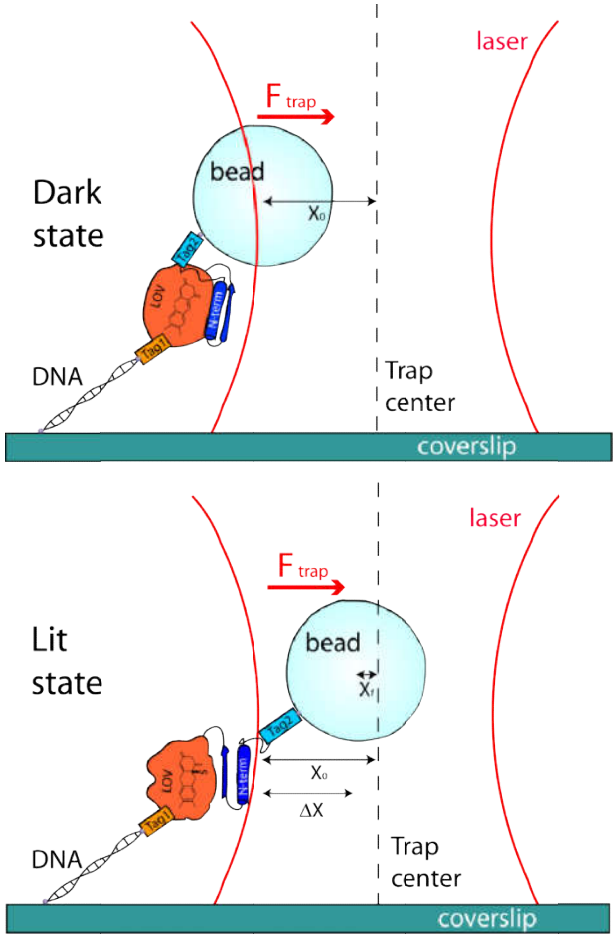

Figure 4-21. Molecular assay to measure conformational changes in the LOV domain. The LOV domain is tagged in both ends to be attached to a micro sphere and to the cover glass of the sample. The microsphere can be manipulated by the optical tweezers and detection of the position of the bead in its initial dark state (X_0) and its final lit state (X_f) is possible, thus the change in the total length (ΔX) of the molecular construction (DNA-LOV domain) can be measured. Figure not to scale.

R_{min}=2.1 nm (32.4 kDa)[212]. Then the total length of the molecular tether shown in Figure 4-21 will increase at least Δx_{min}= 0.8 nm. For the upper limit, the crystallographic structure of VVD dark state monomer[147] and the homodimeric lit state[169] were compared and assuming that the protein would conserve the same orientation and structure as in the crystal, then the extension increment will

correspond to Δx_{max} ~3 nm (Figure 4-22), but even bigger increments can be expected, since in these two cases the structural mobility are restricted by the crystal lattice.

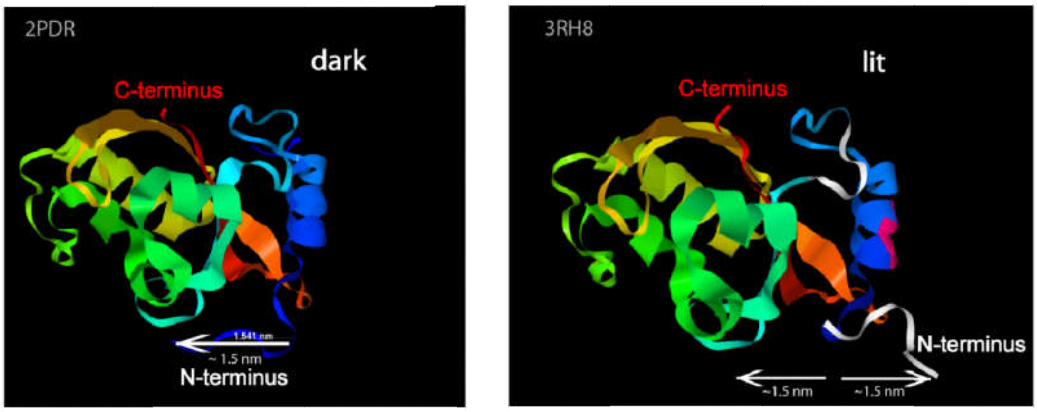

Figure 4-22. Magnitude of the conformational change in VVD. The protein is going to be attached at the N- and C- terminus to a DNA or a bead, so in the dark condition the tether points will be aligned (dashed white line), but in the lit condition the tether points will move away for approximately 3 nm. (Gray letters) Protein data bank code.

In addition, the conformational change that we are interested to measure will be triggered by a blue light pulse we will be able to perform an ensemble averaging which increases spatial and temporal resolution decreasing thermal noise. In ensemble averaging N independent events are synchronized (at the beginning or at the end of the conformational change) and averaged point by point instead of time-averaging the position data of a single event to reduce thermal noise. Temporal resolution for this kind of average is determined by the accuracy in detecting beginning or ending of the conformational change[213]. In our case, the conformational change of LOV domains are triggered by blue light setting a clear moment for events synchronization, making this experiment the ideal case to apply this method.

Chapter 5. Final comments

Altogether, our studies showed that few modifications to a standard BF microscope configuration plus digital image processing allow performing experiments in a wide range of biological scales, from visualization of transparent thin objects as microtubules and standard deconvolution of unstained cells through single-molecule force and displacements measurements with optical tweezers.

Regarding the role of light as an environmental cue, particularly blue light can induce biological responses and oxidative stress, and our results show that blue light photoreceptors can be involved in both effects. Our studies highlight the dual possibility of photoreceptor proteins as blue light sensors and photosensitizers, which can react with O_2 producing ROS. In particular for the LOV domain VVD, our data showed that besides its molecular role as photoreceptors, VVD must be considered for its function as $^1O_2$ producer and also the side effects of $^1O_2$ over VVD itself must be taken into account in the future.

In general protein native conformation is barely stable and this instability could be an advantage for the protein, making them more sensitive to small changes around critical values and afforded proteins with optional states to adapt to changing environmental conditions. Our studies over VVD aggregation pathway showed that VVD stability is sensitive to oxygen presence, temperature, and light stimulus, highlighting how proteins elapse in the edge between two or more states and how multiple external factors can tune protein dynamic along its folding energy landscape.

Current interest in studying the functioning of LOV domains, besides understanding how organisms respond to light stimulus at a molecular level, relapse in the role of LOV domains as part of the tool kit of optogenetic techniques. In 2010 optogenetics was named by Nature magazine the method of the year due to its

potential applications to accurately regulate cellular processes, thus future engineered proteins will require a full understanding of this domain. Also cancer treatments with photodynamic therapy appear as a possible application for LOV domains due to its photosensitizer capabilities, however until now it is not clear how flavin-binding domains regulate its reactivity with O_2. Our results are a step in that direction, showing that LOV domains can perform different photocycles that include light standard perception or off-pathway reactions that produce singlet oxygen.

Bibliography

1. Audesirk, T. & Audesirk, G. *Biology : life on earth*. (Prentice Hall, 1996).
2. Koshland, D. E. The Seven Pillars of Life. *Science.* **295,** (2002).
3. Bustamante, C. *In singulo* Biochemistry: When Less Is More. *Annu. Rev. Biochem.* **77,** 45–50 (2008).
4. Gross, M. *Light and Life*. (Oxford University Press, 2003).
5. A complete microscope history - Who invented the microscope? Available at: http://www.history-of-the-microscope.org/history-of-the-microscope-who-invented-the-microscope.php.
6. Kourkoutis, L. F., Plitzko, J. M. & Baumeister, W. Electron Microscopy of Biological Materials at the Nanometer Scale. *Annu. Rev. Mater. Res.* **42,** 33–58 (2012).
7. Chalfie, M., Tu, Y., Euskirchen, G., Ward, W. & Prasher, D. Green fluorescent protein as a marker for gene expression. *Science.* **263,** (1994).
8. Tsien, R. Y. THE GREEN FLUORESCENT PROTEIN. *Annu. Rev. Biochem.* **67,** 509–544 (1998).
9. Sydor, A. M., Czymmek, K. J., Puchner, E. M. & Mennella, V. Super-Resolution Microscopy: From Single Molecules to Supramolecular Assemblies. *Trends Cell Biol.* **25,** 730–748 (2015).
10. Davidson, M. W. & Fellers, T. J. UNDERSTANDING CONJUGATE PLANES AND KÖHLER ILLUMINATION.
11. Illumination | vade mecum microscope. Available at: https://vademecummicroscope.com/category/illumination/.
12. Olympus Microscopy Resource Center. Available at: http://www.olympusmicro.com/index.html.
13. Hecht, E. *Optics*. (Addison-Wesley, 2002).
14. Gutiérrez-Medina, B. & Block, S. M. Visualizing individual microtubules by bright field microscopy. *Am. J. Phys.* **78,** 1152–1159 (2010).
15. Lyons, E. C. Digital Image Processing: An Overview.Computer
16. Jabnoun, H., Benzarti, F. & Amiri, H. Object recognition for blind people based on features extraction. in *International Image Processing, Applications and Systems Conference* 1–6 (IEEE, 2014). doi:10.1109/IPAS.2014.7043293
17. Carl Zeiss Microscopy Online Campus | Education in Microscopy and Digital Imaging. Available at: http://zeiss-campus.magnet.fsu.edu/index.html. (Accessed: 22nd February 2017)
18. Agard, D. A. & Sedat, J. W. Three-dimensional architecture of a polytene

nucleus. *Nature* **302,** 676–681 (1983).

19. Swedlow, J. R. & Platani, M. Live cell imaging using wide-field microscopy and deconvolution. *Cell Struct. Funct.* **27,** 335–41 (2002).

20. Shaw, P. J. in *Handbook Of Biological Confocal Microscopy* 453–467 (Springer US, 2006). doi:10.1007/978-0-387-45524-2_23

21. Sibarita, J.-B. Deconvolution microscopy. *Adv. Biochem. Eng. Biotechnol.* **95,** 201–43 (2005).

22. Huygens - Weatherall Institute of Molecular Medicine. Available at: https://www.imm.ox.ac.uk/huygens. (Accessed: 22nd February 2017)

23. Mcnally, J. G., Karpova, T., Cooper, J. & Conchello, J. A. Three-Dimensional Imaging by Deconvolution Microscopy.

24. Markham, J. & Conchello, J. A. Parametric blind deconvolution: a robust method for the simultaneous estimation of image and blur. *J. Opt. Soc. Am. A. Opt. Image Sci. Vis.* **16,** 2377–91 (1999).

25. Sarder, P. & Nehorai, A. Deconvolution methods for 3-D fluorescence microscopy images. *IEEE Signal Process. Mag.* **23,** 32–45 (2006).

26. Dougherty, R. Extensions of DAMAS and Benefits and Limitations of Deconvolution in Beamforming. in *11th AIAA/CEAS Aeroacoustics Conference* (American Institute of Aeronautics and Astronautics, 2005). doi:10.2514/6.2005-2961

27. Streibl, N. Three-dimensional imaging by a microscope. *J. Opt. Soc. Am. A* **2,** 121 (1985).

28. Holmes, T. J. & O'Connor, N. J. Blind deconvolution of 3D transmitted light brightfield micrographs. *J. Microsc.* **200,** 114–27 (2000).

29. Patire, A. D. (Anthony D. Measuring the point spread function of a light microscope. (Massachusetts Institute of Technology, 1997).

30. TADROUS, P. J. A method of PSF generation for 3D brightfield deconvolution. *J. Microsc.* **237,** 192–199 (2010).

31. Gutiérrez-Medina, B. & Block, S. M. Visualizing individual microtubules by bright field microscopy. *Am. J. Phys.* **78,** 1152–1159 (2010).

32. Agero, U., Mesquita, L. G., Neves, B. R. A., Gazzinelli, R. T. & Mesquita, O. N. Defocusing microscopy. *Microsc. Res. Tech.* **65,** 159–165 (2004).

33. Reshes, G., Vanounou, S., Fishov, I. & Feingold, M. Cell Shape Dynamics in Escherichia coli. *Biophys. J.* **94,** 251–264 (2008).

34. Mir, M. *et al.* Visualizing Escherichia coli Sub-Cellular Structure Using Sparse Deconvolution Spatial Light Interference Tomography. *PLoS One* **7,** e39816 (2012).

35. Carballido-López, R. The bacterial actin-like cytoskeleton. *Microbiol. Mol. Biol. Rev.* **70,** 888–909 (2006).

36. Figge, R. M., Divakaruni, A. V. & Gober, J. W. MreB, the cell shape-determining bacterial actin homologue, co-ordinates cell wall morphogenesis in Caulobacter crescentus. *Mol. Microbiol.* **51,** 1321–1332 (2004).

37. TRIPATHI, S., SUZUKI, J. Y., FERREIRA, S. A. & GONSALVES, D. Papaya ringspot virus-P: characteristics, pathogenicity, sequence variability and control. *Mol. Plant Pathol.* **9,** 269–280 (2008).

38. Xie, S. Single-Molecule Approach to Enzymology. *Single Mol* **2,** 229–236 (2001).

39. Bustamante, C., Cheng, W., Mejia, Y. X. & Meija, Y. X. Revisiting the central dogma one molecule at a time. *Cell* **144,** 480–97 (2011).

40. Simmons, R. Molecular motors: Single-molecule mechanics. *Curr. Biol.* **6,** 392–394 (1996).

41. Xia, T., Li, N. & Fang, X. Single-Molecule Fluorescence Imaging in Living Cells. *Annu. Rev. Phys. Chem.* **64,** 459–480 (2013).

42. Sahl, S. J. & Moerner, W. E. Super-resolution fluorescence imaging with single molecules. *Curr. Opin. Struct. Biol.* **23,** 778–87 (2013).

43. Woodside, M. T. & Block, S. M. Reconstructing folding energy landscapes by single-molecule force spectroscopy. *Annu. Rev. Biophys.* **43,** 19–39 (2014).

44. Neuman, K. C. & Nagy, A. Single-molecule force spectroscopy: optical tweezers, magnetic tweezers and atomic force microscopy. *Nat. Methods* **5,** 491–505 (2008).

45. PIETRASZEWSKA-BOGIEL, A. & GADELLA, T. W. J. FRET microscopy: from principle to routine technology in cell biology. *J. Microsc.* **241,** 111–118 (2011).

46. Betzig, E. *et al.* Imaging Intracellular Fluorescent Proteins at Nanometer Resolution. *Science.* **313,** (2006).

47. Rust, M. J., Bates, M. & Zhuang, X. Sub-diffraction-limit imaging by stochastic optical reconstruction microscopy (STORM). *Nat. Methods* **3,** 793–796 (2006).

48. Hell, S. W. & Wichmann, J. Breaking the diffraction resolution limit by stimulated emission: stimulated-emission-depletion fluorescence microscopy. *Opt. Lett.* **19,** 780 (1994).

49. Ashkin, A. Acceleration and Trapping of Particles by Radiation Pressure. *Phys. Rev. Lett.* **24,** 156–159 (1970).

50. Ashkin, A. & Dziedzic, J. M. Optical Levitation by Radiation Pressure. *Appl. Phys. Lett.* **19,** 283–285 (1971).

51. Ashkin, A., Dziedzic, J. M., Bjorkholm, J. E. & Chu, S. Observation of a single-beam gradient force optical trap for dielectric particles. *Opt. Lett.* **11,** (1986).

52. Lewalle, A. The Smallest Tweezers in the World. *Phys. Teach.* **46,** 467–472

(2008).

53. Neuman, K. C. & Block, S. M. Optical trapping. *Rev. Sci. Instrum.* **75,** 2787–2809 (2004).

54. Wang, M. D. *et al.* Force and Velocity Measured for Single Molecules of RNA Polymerase. *Science.* **282,** (1998).

55. Wen, J.-D. *et al.* Following translation by single ribosomes one codon at a time. *Nature* **452,** 598–603 (2008).

56. Bennink, M. L. *et al.* Unfolding individual nucleosomes by stretching single chromatin fibers with optical tweezers. *Nat. Struct. Biol.* **8,** 606–610 (2001).

57. Spudich, J. A., Rice, S. E., Rock, R. S., Purcell, T. J. & Warrick, H. M. Optical traps to study properties of molecular motors. *Cold Spring Harb. Protoc.* **2011,** 1305–18 (2011).

58. Bustamante, C., Chemla, Y. R., Forde, N. R. & Izhaky, D. Mechanical Processes in Biochemistry. *Annu. Rev. Biochem.* **73,** 705–748 (2004).

59. Wright, W. H., Sonek, G. J. & Berns, M. W. Parametric study of the forces on microspheres held by optical tweezers. *Appl. Opt.* **33,** 1735 (1994).

60. Neuman, K. C., Chadd, E. H., Liou, G. F., Bergman, K. & Block, S. M. Characterization of Photodamage to Escherichia coli in Optical Traps. *Biophys. J.* **77,** 2856–2863 (1999).

61. Smith, S. B., Finzi, L. & Bustamante, C. Direct mechanical measurements of the elasticity of single DNA molecules by using magnetic beads. *Science* **258,** 1122–6 (1992).

62. Bustamante, C., Smith, S. B., Liphardt, J. & Smith, D. Single-molecule studies of DNA mechanics. *Curr. Opin. Struct. Biol.* **10,** 279–285 (2000).

63. Wang, M. D., Yin, H., Landick, R., Gelles, J. & Block, S. M. Stretching DNA with optical tweezers. *Biophys. J.* **72,** 1335–1346 (1997).

64. Smith, S. B., Cui, Y. & Bustamante, C. Overstretching B-DNA: the elastic response of individual double-stranded and single-stranded DNA molecules. *Science* **271,** 795–9 (1996).

65. Bustamante, C., Bryant, Z. & Smith, S. B. Ten years of tension: single-molecule DNA mechanics. *Nature* **421,** 423–427 (2003).

66. Geggier, S. & Vologodskii, A. Sequence dependence of DNA bending rigidity. *Proc. Natl. Acad. Sci. U. S. A.* **107,** 15421–6 (2010).

67. Boedicker, J. Q., Garcia, H. G., Johnson, S. & Phillips, R. DNA sequence-dependent mechanics and protein-assisted bending in repressor-mediated loop formation. *Phys. Biol.* **10,** 66005 (2013).

68. Baumann, C. G., Smith, S. B., Bloomfield, V. A. & Bustamante, C. Ionic effects on the elasticity of single DNA molecules. *Proc. Natl. Acad. Sci. U. S. A.* **94,** 6185–90 (1997).

69. Parvin, J. D., McCormick, R. J., Sharp, P. A. & Fisher, D. E. Pre-bending of a promoter sequence enhances affinity for the TATA-binding factor. *Nature* **373,** 724–727 (1995).

70. Strauss, J. K. & Maher, L. J. DNA bending by asymmetric phosphate neutralization. *Science* **266,** 1829–34 (1994).

71. Bouchiat, C. *et al.* Estimating the Persistence Length of a Worm-Like Chain Molecule from Force-Extension Measurements.

72. Gaub, H. E., Rief, M. & Clausen-Schaumann, H. Sequence-dependent mechanics of single DNA molecules. *Nat. Struct. Biol.* **6,** 346–349 (1999).

73. Bustamante, C., Marko, J., Siggia, E. & Smith, S. Entropic elasticity of lambda-phage DNA. *Science.* **265,** (1994).

74. Cluzel, P. *et al.* DNA: An Extensible Molecule. *Science.* **271,** (1996).

75. Gittes, F., Mickey, B., Nettleton, J. & Howard, J. Flexural Rigidity of Microtubules and Actin Filaments Measured from Thermal Fluctuations in Shape.

76. Howard, J. The Movement of Kinesin Along Microtubules. *Annu. Rev. Physiol.* **58,** 703–729 (1996).

77. Sowdhamini, D. P., Divya P. Syamaladevi, J. A., James A. Spudich, R. & Sowdhamini. Structural and Functional Insights on the Myosin Superfamily. *Bioinform. Biol. Insights* **6,** 11 (2012).

78. Hirokawa, N., Noda, Y. & Okada, Y. Kinesin and dynein superfamily proteins in organelle transport and cell division. *Curr. Opin. Cell Biol.* **10,** 60–73 (1998).

79. Hirokawa, N., Noda, Y., Tanaka, Y. & Niwa, S. Kinesin superfamily motor proteins and intracellular transport. *Nat. Rev. Mol. Cell Biol.* **10,** 682–696 (2009).

80. Sweeney, H. L. & Houdusse, A. Structural and Functional Insights into the Myosin Motor Mechanism. *Annu. Rev. Biophys.* **39,** 539–557 (2010).

81. Roberts, A. J., Kon, T., Knight, P. J., Sutoh, K. & Burgess, S. A. Functions and mechanics of dynein motor proteins. *Nat. Rev. Mol. Cell Biol.* **14,** 713–726 (2013).

82. Cianfrocco, M. A., DeSantis, M. E., Leschziner, A. E. & Reck-Peterson, S. L. Mechanism and Regulation of Cytoplasmic Dynein. *Annu. Rev. Cell Dev. Biol.* **31,** 83–108 (2015).

83. Schmidt, H. & Carter, A. P. Review: Structure and mechanism of the dynein motor ATPase. *Biopolymers* **105,** 557–567 (2016).

84. Vale, R. D., Reese, T. S. & Sheetz, M. P. Identification of a novel force-generating protein, kinesin, involved in microtubule-based motility. *Cell* **42,** 39–50 (1985).

85. Lasek, R. J. & Brady, S. T. Attachment of transported vesicles to

microtubules in axoplasm is facilitated by AMP-PNP. *Nature* **316,** 645–7

86. Brady, S. T. A novel brain ATPase with properties expected for the fast axonal transport motor. *Nature* **317,** 73–5

87. Wordeman, L. How kinesin motor proteins drive mitotic spindle function: Lessons from molecular assays. *Semin. Cell Dev. Biol.* **21,** 260–8 (2010).

88. Kashina, A. S. *et al.* A bipolar kinesin. *Nature* **379,** 270–2 (1996).

89. Bloom, G. S., Wagner, M. C., Pfister, K. K. & Brady, S. T. Native structure and physical properties of bovine brain kinesin and identification of the ATP-binding subunit polypeptide. *Biochemistry* **27,** 3409–3416 (1988).

90. Woźniak, M. J. & Allan, V. J. Cargo selection by specific kinesin light chain 1 isoforms. *EMBO J.* **25,** 5457–68 (2006).

91. Wong, Y. L. & Rice, S. E. Kinesin's light chains inhibit the head- and microtubule-binding activity of its tail. *Proc. Natl. Acad. Sci. U. S. A.* **107,** 11781–6 (2010).

92. Kozielski, F. *et al.* The Crystal Structure of Dimeric Kinesin and Implications for Microtubule-Dependent Motility. *Cell* **91,** 985–994 (1997).

93. Case, R. B. *et al.* Role of the kinesin neck linker and catalytic core in microtubule-based motility. *Curr. Biol.* **10,** 157–60 (2000).

94. Gennerich, A. & Vale, R. D. Walking the walk: how kinesin and dynein coordinate their steps. doi:10.1016/j.ceb.2008.12.002

95. Case, R. B., Pierce, D. W., Hom-Booher, N., Hart, C. L. & Vale, R. D. The directional preference of kinesin motors is specified by an element outside of the motor catalytic domain. *Cell* **90,** 959–66 (1997).

96. Rice, S. *et al.* A structural change in the kinesin motor protein that drives motility. *Nature* **402,** 778–784 (1999).

97. MotorToolBoxKinesin.jpg (3008×2183). Available at: https://valelab4.ucsf.edu/external/images/res-kinesin-new/MotorToolBoxKinesin.jpg. (Accessed: 10th March 2017)

98. Howard, J., Hudspeth, A. J. & Vale, R. D. Movement of microtubules by single kinesin molecules. *Nature* **342,** 154–158 (1989).

99. Yildiz, A., Tomishige, M., Vale, R. D. & Selvin, P. R. Kinesin Walks Hand-Over-Hand. *Science.* **303,** 676–678 (2004).

100. Asbury, C. L., Fehr, A. N. & Block, S. M. Kinesin Moves by an Asymmetric Hand-Over-Hand Mechanism. *Science.* **302,** (2003).

101. Ray, S., Meyhöfer, E., Milligan, R. A. & Howard, J. Kinesin follows the microtubule's protofilament axis. *J. Cell Biol.* **121,** 1083–93 (1993).

102. Asbury, C. L. Kinesin: world's tiniest biped. *Curr. Opin. Cell Biol.* **17,** 89–97 (2005).

103. Block, S. M. Kinesin: what gives? *Cell* **93,** 5–8 (1998).

104. Svoboda, K., Schmidt, C. F., Schnapp, B. J. & Block, S. M. Direct observation of kinesin stepping by optical trapping interferometry. *Nature* **365,** 721–727 (1993).

105. Coy, D. L., Wagenbach, M. & Howard, J. Kinesin takes one 8-nm step for each ATP that it hydrolyzes. *J. Biol. Chem.* **274,** 3667–71 (1999).

106. Xie, P. Mechanism of Processive Movement of Monomeric and Dimeric Kinesin Molecules. *Int. J. Biol. Sci.* 665–674 (2010). doi:10.7150/ijbs.6.665

107. Fox, D. What sparked the Cambrian explosion? *Nature* **530,** 268–270 (2016).

108. Smith, H. B. Photoreceptors in signal transduction. Pathways of enlightenment. *Plant Cell* **12,** 1–3 (2000).

109. Schrott, E. L. Fluence response relationship of carotenogenesis inNeurospora crassa. *Planta* **150,** 174–179 (1980).

110. Banbury, D. G. H. Phototropism and Light -growth Responses of the Tall Conidiophores of Aspergillus giganteus. *J . gen. Microbiol* **54,** 427–438 (1969).

111. Ambra, R. *et al.* Photomorphogenesis in the hypogeous fungus Tuber borchii: isolation and characterization of Tbwc-1, the homologue of the blue-light photoreceptor of Neurospora crassa. *Fungal Genet. Biol.* **41,** 688–697 (2004).

112. Berliner, M. D. & Neurath, P. W. The band forming rhythm ofNeurospora mutants. *J. Cell. Comp. Physiol.* **65,** 183–193 (1965).

113. Potapova, T. V., Levina, N. N., Belozerskaya, T. A., Kritsky, M. S. & Chailakhian, L. M. Investigation of electrophysiological responses of Neurospora crassa to blue light. *Arch. Microbiol.* **137,** 262–265 (1984).

114. Sargent, M. L., Briggs, W. R. & Woodward, D. O. Circadian nature of a rhythm expressed by an invertaseless strain of Neurospora crassa. *Plant Physiol.* **41,** 1343–9 (1966).

115. Degli-Innocenti, F. & Russo, V. E. Isolation of new white collar mutants of Neurospora crassa and studies on their behavior in the blue light-induced formation of protoperithecia. *J. Bacteriol.* **159,** 757–61 (1984).

116. Chen, C.-H. & Loros, J. J. Neurospora sees the light: light signaling components in a model system. *Commun. Integr. Biol.* **2,** 448–51 (2009).

117. Herrera-Estrella, A. & Horwitz, B. A. Looking through the eyes of fungi: molecular genetics of photoreception. *Mol. Microbiol.* **64,** 5–15 (2007).

118. Chen, C.-H., Dunlap, J. C. & Loros, J. J. Neurospora illuminates fungal photoreception. *Fungal Genet. Biol.* **47,** 922–9 (2010).

119. Schmoll, M., Esquivel-Naranjo, E. U. & Herrera-Estrella, A. Trichoderma in the light of day--physiology and development. *Fungal Genet. Biol.* **47,** 909–16 (2010).

120. Rosales-Saavedra, T. *et al.* Novel light-regulated genes in Trichoderma

atroviride: a dissection by cDNA microarrays. *Microbiology* **152,** 3305–3317 (2006).

121. Fischer, R., Aguirre, J., Herrera-Estrella, A. & Corrochano, L. M. The Complexity of Fungal Vision. *Microbiol. Spectr.* **4,** (2016).

122. Conrad, K. S., Manahan, C. C. & Crane, B. R. Photochemistry of Flavoprotein Light Sensors. doi:10.1038/nchembio.1633

123. Linden, H., Ballario, P. & Macino, G. Blue Light Regulation inNeurospora crassa. *Fungal Genet. Biol.* **22,** 141–150 (1997).

124. Cheng, P., Yang, Y., Wang, L., He, Q. & Liu, Y. WHITE COLLAR-1, a multifunctional neurospora protein involved in the circadian feedback loops, light sensing, and transcription repression of wc-2. *J. Biol. Chem.* **278,** 3801–8 (2003).

125. Linden, H. & Macino, G. White collar 2, a partner in blue-light signal transduction, controlling expression of light-regulated genes in Neurospora crassa. *EMBO J.* **16,** 98–109 (1997).

126. Hurley, J., Loros, J. J. & Dunlap, J. C. Dissecting the mechanisms of the clock in Neurospora. *Methods Enzymol.* **551,** 29–52 (2015).

127. Froehlich, A. C., Liu, Y., Loros, J. J. & Dunlap, J. C. White Collar-1, a Circadian Blue Light Photoreceptor, Binding to the frequency Promoter. *Science.* **297,** (2002).

128. He, Q. & Liu, Y. Molecular mechanism of light responses in Neurospora: from light-induced transcription to photoadaptation. doi:10.1101/gad.1369605

129. Gin, E., Diernfellner, A. C., Brunner, M. & Hö Fer, T. The Neurospora photoreceptor VIVID exerts negative and positive control on light sensing to achieve adaptation. *Mol. Syst. Biol.* **9,** (2013).

130. Casas-Flores, S. BLR-1 and BLR-2, key regulatory elements of photoconidiation and mycelial growth in Trichoderma atroviride. *Microbiology* **150,** 3561–3569 (2004).

131. Gudipati, V., Koch, K., Lienhart, W.-D. & Macheroux, P. The flavoproteome of the yeast Saccharomyces cerevisiae. *Biochim. Biophys. Acta - Proteins Proteomics* **1844,** 535–544 (2014).

132. Lienhart, W.-D., Gudipati, V. & Macheroux, P. The human flavoproteome. *Arch. Biochem. Biophys.* **535,** 150–62 (2013).

133. Chaiyen, P. & Scrutton, N. S. Special Issue: Flavins and Flavoproteins. *FEBS J.* **282,** 3001–3002 (2015).

134. Bialas, C. *et al.* Engineering an Artificial Flavoprotein Magnetosensor. *J. Am. Chem. Soc.* **138,** 16584–16587 (2016).

135. Ghisla, S. & Massey, V. REVIEW ARTICLE New flavins for old: artificial flavins as active site probes of flavoproteins. *Biochem. J* **239,** 1–12 (1986).

136. Henriques, B. J., Olsen, R. K., Bross, P. & Gomes, C. M. Emerging roles for

riboflavin in functional rescue of mitochondrial β-oxidation flavoenzymes. *Curr. Med. Chem.* **17,** 3842–54 (2010).

137. Choe, E. & Min, D. B. Chemistry and Reactions of Reactive Oxygen Species in Foods. *Crit. Rev. Food Sci. Nutr.* **46,** 1–22 (2006).

138. Stadtman, E. R. & Levine, R. L. Protein oxidation. *Ann. N. Y. Acad. Sci.* **899,** 191–208 (2000).

139. Jena, N. R. DNA damage by reactive species: Mechanisms, mutation and repair. *J. Biosci.* **37,** 503–17 (2012).

140. Davies, M. J. Singlet oxygen-mediated damage to proteins and its consequences. *Biochem. Biophys. Res. Commun.* **305,** 761–770 (2003).

141. Chaiyen, P. *et al.* The enigmatic reaction of flavins with oxygen. *Trends Biochem. Sci.* **37,** 373–80 (2012).

142. Mukherjee, A., Walker, J., Weyant, K. B., Schroeder, C. M. & Stahl, U. Characterization of Flavin-Based Fluorescent Proteins: An Emerging Class of Fluorescent Reporters. *PLoS One* **8,** e64753 (2013).

143. Abrahamse, H. & Hamblin, M. R. New photosensitizers for photodynamic therapy. *Biochem. J.* **473,** 347–364 (2016).

144. Krauss, U. *et al.* Distribution and phylogeny of light-oxygen-voltage-blue-light-signaling proteins in the three kingdoms of life. *J. Bacteriol.* **191,** 7234–42 (2009).

145. Christie, J. M., Salomon, M., Nozue, K., Wada, M. & Briggs, W. R. LOV (light, oxygen, or voltage) domains of the blue-light photoreceptor phototropin (nph1): binding sites for the chromophore flavin mononucleotide. *Proc. Natl. Acad. Sci. U. S. A.* **96,** 8779–83 (1999).

146. Suetsugu, N. & Wada, M. Evolution of Three LOV Blue Light Receptor Families in Green Plants and Photosynthetic Stramenopiles: Phototropin, ZTL/FKF1/LKP2 and Aureochrome. doi:10.1093/pcp/pcs165

147. Zoltowski, B. D. *et al.* Conformational Switching in the Fungal Light Sensor Vivid. *Science.* **316,** 1054–1057 (2007).

148. Herrou, J. & Crosson, S. Function, structure and mechanism of bacterial photosensory LOV proteins. *Nat. Rev. Microbiol.* **9,** 713–723 (2011).

149. Huala, E. *et al.* Arabidopsis NPH1: a protein kinase with a putative redox-sensing domain. *Science* **278,** 2120–3 (1997).

150. Zoltowski, B. D., Motta-Mena, L. B. & Gardner, K. H. Blue light-induced dimerization of a bacterial LOV-HTH DNA-binding protein. *Biochemistry* **52,** 6653–61 (2013).

151. Sean Crosson, ‡, Sudarshan Rajagopal, ‡ and & Keith Moffat*, ‡,§. The LOV Domain Family: Photoresponsive Signaling Modules Coupled to Diverse Output Domains†. (2002). doi:10.1021/BI026978L

152. Chen, C.-H., DeMay, B. S., Gladfelter, A. S., Dunlap, J. C. & Loros, J. J.

Physical interaction between VIVID and white collar complex regulates photoadaptation in Neurospora. *Proc. Natl. Acad. Sci. U. S. A.* **107,** 16715–20 (2010).

153. Pellequer, J. L., Wager-Smith, K. A., Kay, S. A. & Getzoff, E. D. Photoactive yellow protein: a structural prototype for the three-dimensional fold of the PAS domain superfamily. *Proc. Natl. Acad. Sci. U. S. A.* **95,** 5884–90 (1998).

154. Crosson, S. & Moffat, K. Structure of a flavin-binding plant photoreceptor domain: insights into light-mediated signal transduction. *Proc. Natl. Acad. Sci. U. S. A.* **98,** 2995–3000 (2001).

155. Yee, E. F. *et al.* Signal transduction in light-oxygen-voltage receptors lacking the adduct-forming cysteine residue. *Nat. Commun.* **6,** 10079 (2015).

156. Kay, C. W. M. *et al.* Blue light perception in plants. Detection and characterization of a light-induced neutral flavin radical in a C450A mutant of phototropin. *J. Biol. Chem.* **278,** 10973–82 (2003).

157. Zoltowski, B. D., Vaccaro, B. & Crane, B. R. Mechanism-based tuning of a LOV domain photoreceptor. *Nat. Chem. Biol.* **5,** 827–834 (2009).

158. Dasgupta, A. *et al.* Biological Significance of Photoreceptor Photocycle Length: VIVID Photocycle Governs the Dynamic VIVID-White Collar Complex Pool Mediating Photo-adaptation and Response to Changes in Light Intensity. *PLOS Genet.* **11,** e1005215 (2015).

159. Salomon, M. *et al.* An optomechanical transducer in the blue light receptor phototropin from Avena sativa. *Proc. Natl. Acad. Sci. U. S. A.* **98,** 12357–61 (2001).

160. Pudasaini, A., El-Arab, K. K. & Zoltowski, B. D. LOV-based optogenetic devices: light-driven modules to impart photoregulated control of cellular signaling. *Front. Mol. Biosci.* **2,** 18 (2015).

161. Schwerdtfeger, C. & Linden, H. VIVID is a flavoprotein and serves as a fungal blue light photoreceptor for photoadaptation. *EMBO J.* **22,** 4846–55 (2003).

162. Heintzen, C., Loros, J. J. & Dunlap, J. C. The PAS Protein VIVID Defines a Clock-Associated Feedback Loop that Represses Light Input, Modulates Gating, and Regulates Clock Resetting. *Cell* **104,** 453–464 (2001).

163. Elvin, M., Loros, J. J., Dunlap, J. C. & Heintzen, C. The PAS/LOV protein VIVID supports a rapidly dampened daytime oscillator that facilitates entrainment of the Neurospora circadian clock. *Genes Dev.* **19,** 2593–605 (2005).

164. Hunt, S. M., Elvin, M., Crosthwaite, S. K. & Heintzen, C. The PAS/LOV protein VIVID controls temperature compensation of circadian clock phase and development in Neurospora crassa. *Genes Dev.* **21,** 1964–74 (2007).

165. Zhang, Y., Lamm, R., Pillonel, C., Lam, S. & Xu, J.-R. Osmoregulation and fungicide resistance: the Neurospora crassa os-2 gene encodes a HOG1

mitogen-activated protein kinase homologue. *Appl. Environ. Microbiol.* **68,** 532–8 (2002).

166. Lew, R. R. & Levina, N. N. Turgor regulation in the osmosensitive cut mutant of Neurospora crassa. *Microbiology* **153,** 1530–1537 (2007).

167. Youssar, L. & Avalos, J. Light-dependent regulation of the gene cut-1 of Neurospora, involved in the osmotic stress response. *Fungal Genet. Biol.* **43,** 752–763 (2006).

168. Lamb, J. S. *et al.* Illuminating Solution Responses of a LOV Domain Protein with Photocoupled Small-Angle X-Ray Scattering. *J. Mol. Biol.* **393,** 909–919 (2009).

169. Vaidya, A. T., Chen, C.-H., Dunlap, J. C., Loros, J. J. & Crane, B. R. Structure of a light-activated LOV protein dimer that regulates transcription. *Sci. Signal.* **4,** ra50 (2011).

170. Ko, W.-H., Nash, A. I. & Gardner, K. H. A LOVely view of blue light photosensing. *Nat. Chem. Biol.* **3,** 372–374 (2007).

171. Lee, C.-T., Malzahn, E., Brunner, M. & Mayer, M. P. Light-Induced Differences in Conformational Dynamics of the Circadian Clock Regulator VIVID. *J. Mol. Biol.* **426,** 601–610 (2014).

172. Lokhandwala, J. *et al.* A Native Threonine Coordinates Ordered Water to Tune Light-Oxygen-Voltage (LOV) Domain Photocycle Kinetics and Osmotic Stress Signaling in Trichoderma reesei ENVOY. *J. Biol. Chem.* **291,** 14839–50 (2016).

173. Lokhandwala, J. *et al.* Structural Biochemistry of a Fungal LOV Domain Photoreceptor Reveals an Evolutionarily Conserved Pathway Integrating Light and Oxidative Stress. *Structure* **23,** 116–125 (2015).

174. Schmoll, M., Franchi, L. & Kubicek, C. P. Envoy, a PAS/LOV Domain Protein of Hypocrea jecorina (Anamorph Trichoderma reesei), Modulates Cellulase Gene Transcription in Response to Light. *Eukaryot. Cell* **4,** 1998–2007 (2005).

175. Lokhandwala, J. *et al.* Structural biochemistry of a fungal LOV domain photoreceptor reveals an evolutionarily conserved pathway integrating light and oxidative stress. *Structure* **23,** 116–25 (2015).

176. Pace, C. N. Conformational stability of globular proteins. *Trends Biochem. Sci.* **15,** 14–17 (1990).

177. Chiti, F. & Dobson, C. M. Amyloid formation by globular proteins under native conditions. *Nat. Chem. Biol.* **5,** 15–22 (2009).

178. Tyedmers, J., Mogk, A. & Bukau, B. Cellular strategies for controlling protein aggregation. *Nat. Rev. Mol. Cell Biol.* **11,** 777–788 (2010).

179. Von Mikecz, A. Protein Aggregation in the Cell Nucleus: Structure, Function and Topology THE CELL NUCLEUS: DYNAMIC MACROMOLE- CULE CLUSTERING PROVIDES FUNCTION. *Open Biol. J.* **2,** 193–199 (2009).

180. López-Otín, C. *et al.* The Hallmarks of Aging. *Cell* **153,** 1194–1217 (2013).

181. Stefani, M. Protein misfolding and aggregation: new examples in medicine and biology of the dark side of the protein world for Molecular and Clinical Studies on chronic, inflammatory, degenerative and tumoural diseases for the development of new therapies. *Biochim. Biophys. Acta* **5,** (2004).

182. Wang, W. Protein aggregation and its inhibition in biopharmaceutics. *Int. J. Pharm.* **289,** 1–30 (2005).

183. Frokjaer, S. & Otzen, D. E. Protein drug stability: a formulation challenge. *Nat. Rev. Drug Discov.* **4,** 298–306 (2005).

184. Winklhofer, K. F., Rg Tatzelt, J. & Haass, C. Focus Quality Control The two faces of protein misfolding: gain-and loss-of-function in neurodegenerative diseases Oligomeric protein assemblies in a deadly cascade. *EMBO J.* **27,** 336–349 (2008).

185. Hartl, F. U. & Hayer-Hartl, M. Converging concepts of protein folding in vitro and in vivo. *Nat. Struct. Mol. Biol.* **16,** 574–581 (2009).

186. Zhao, R. *et al.* Measurement of amyloid formation by turbidity assay-seeing through the cloud. *Biophys. Rev.* **8,** 445–471 (2016).

187. Cohen, S. I. A., Vendruscolo, M., Dobson, C. M. & Knowles, T. P. J. From Macroscopic Measurements to Microscopic Mechanisms of Protein Aggregation. *J. Mol. Biol.* **421,** 160–171 (2012).

188. Chi, E. Y., Krishnan, S., Randolph, T. W. & Carpenter, J. F. Physical Stability of Proteins in Aqueous Solution: Mechanism and Driving Forces in Nonnative Protein Aggregation. *Pharm. Res.* **20,** 1325–1336 (2003).

189. Betteridge, D. J. What is oxidative stress? *Metabolism.* **49,** 3–8 (2000).

190. Auten, R. L. & Davis, J. M. Oxygen Toxicity and Reactive Oxygen Species: The Devil Is in the Details. *Pediatr. Res.* **66,** 121–127 (2009).

191. Davies, K. J. Protein damage and degradation by oxygen radicals. I. general aspects. *J. Biol. Chem.* **262,** 9895–901 (1987).

192. Davies, K. J. & Delsignore, M. E. Protein damage and degradation by oxygen radicals. III. Modification of secondary and tertiary structure. *J. Biol. Chem.* **262,** 9908–13 (1987).

193. Davies, K. J., Delsignore, M. E. & Lin, S. W. Protein damage and degradation by oxygen radicals. II. Modification of amino acids. *J. Biol. Chem.* **262,** 9902–7 (1987).

194. Davies, K. J. Degradation of oxidized proteins by the 20S proteasome. *Biochimie* **83,** 301–10 (2001).

195. Chao, C. C., Ma, Y. S. & Stadtman, E. R. Modification of protein surface hydrophobicity and methionine oxidation by oxidative systems. *Proc. Natl. Acad. Sci. U. S. A.* **94,** 2969–74 (1997).

196. Stadtman, E. R. & Levine, R. L. Free radical-mediated oxidation of free

amino acids and amino acid residues in proteins. *Amino Acids* **25,** 207–218 (2003).

197. Stadtman, E. R. Oxidation of Free Amino Acids and Amino Acid Residues in Proteins by Radiolysis and by Metal-Catalyzed Reactions. *Annu. Rev. Biochem.* **62,** 797–821 (1993).

198. Turrens, J. F. Mitochondrial formation of reactive oxygen species. *J. Physiol.* **552,** 335–44 (2003).

199. Seaver, L. C. & Imlay, J. A. Are Respiratory Enzymes the Primary Sources of Intracellular Hydrogen Peroxide? *J. Biol. Chem.* **279,** 48742–48750 (2004).

200. Imlay, J. A. The molecular mechanisms and physiological consequences of oxidative stress: lessons from a model bacterium. doi:10.1038/nrmicro3032

201. Eichler, M., Lavi, R., Shainberg, A. & Lubart, R. Flavins are source of visible-light-induced free radical formation in cells. *Lasers Surg. Med.* **37,** 314–319 (2005).

202. Liang, J.-Y., Cheng, C.-W., Yu, C.-H. & Chen, L.-Y. Investigations of blue light-induced reactive oxygen species from flavin mononucleotide on inactivation of E. coli. *J. Photochem. Photobiol. B.* **143,** 82–8 (2015).

203. Consentino, L. *et al.* Blue-light dependent reactive oxygen species formation by Arabidopsis cryptochrome may define a novel evolutionarily conserved signaling mechanism. *New Phytol.* **206,** 1450–62 (2015).

204. Shu, X. *et al.* A genetically encoded tag for correlated light and electron microscopy of intact cells, tissues, and organisms. *PLoS Biol.* **9,** e1001041 (2011).

205. Sarkisyan, K. S. *et al.* KillerOrange, a Genetically Encoded Photosensitizer Activated by Blue and Green Light. *PLoS One* **10,** e0145287 (2015).

206. Takemoto, K. *et al.* SuperNova, a monomeric photosensitizing fluorescent protein for chromophore-assisted light inactivation. *Sci. Rep.* **3,** 2629 (2013).

207. McCaughan, J. S. Photodynamic therapy: a review. *Drugs Aging* **15,** 49–68 (1999).

208. Beckett, D., Kovaleva, E. & Schatz, P. J. A minimal peptide substrate in biotin holoenzyme synthetase-catalyzed biotinylation. *Protein Sci.* **8,** 921–9 (1999).

209. Liu, Y. & Bell-Pedersen, D. Circadian rhythms in Neurospora crassa and other filamentous fungi. *Eukaryot. Cell* **5,** 1184–93 (2006).

210. Yoshida, Y., Iigusa, H., Wang, N. & Hasunuma, K. Cross-Talk between the Cellular Redox State and the Circadian System in Neurospora. *PLoS One* **6,** e28227 (2011).

211. Lledías, F., Rangel, P. & Hansberg, W. Oxidation of Catalase by Singlet Oxygen. *J. Biol. Chem.* **273,** 10630–10637 (1998).

212. Erickson, H. P. Size and Shape of Protein Molecules at the Nanometer Level

Determined by Sedimentation, Gel Filtration, and Electron Microscopy. *Biol. Proced. Online* **11,** 32–51 (2009).

213. Tinoco, I. & Gonzalez, R. L. Biological mechanisms, one molecule at a time. *Genes Dev.* **25,** 1205–1231 (2011).

Appendix A

Materials and Methods

All reagents were purchased from SIGMA unless otherwise specified. Data were analyzed using the statistical analysis software IGOR. And automation of the optical tweezers and the BF image acquisition and image processing were performed with Labview software.

Coverslip cleaning and poly-L-lysine cover

Microscope slides and coverslips were cleaned prior to use for 5 min in a plasma cleaner (Harrick Plasma) at 1 Torr (ambient air). A rack of plasma-cleaned coverslips was submerged in a solution of 600 µL of poly-L-lysine diluted with 300 mL of ethanol, incubated for 15 min, dried in an oven at 40°C, and stored in a closed container.

In vitro microtubules polymerization and visualization

Lyophilized tubulin (TL238-C, Cytoskeleton) was resuspended to a final concentration of 10 mg/ml by adding 100 µl of PEMGTP buffer (1 µl of GTP 100 mM 99 ml PEM). PEM buffer was 80 mM Pipes, pH 6.9, 1 mM EGTA, 4 mM $MgCl_2$.

To polymerized the tubulin, in a clean eppendorf tube 60.8 µl PEMGTP, 2.2 µl DMSO, and 4.8 µl tubulin 10mg/ml were mixed and incubated at 37°C for 30 min.

In the meantime, STAB buffer (83.6 µl PEM, 1 µl of GTP 100 mM, 9.4 µl 65 g/l NaN_3, and 6.0 µl Taxol (TXD01, Cytoskeleton) 2mM)was prepared. After the incubation time, 8 µl of STAB buffer were added to the polymerized tubulin.

To view under the microscope, stabilized MTs were diluted 1:100 in PEMTAX buffer (0.02 mM Taxol, 80 mM PIPES, 1 mM EDTA, 4 mM $MgCl_2$, pH 6.9), introduced into the flow channel and incubated for 10 min. Unbound MTs were removed by washing the channel with 40 µL of PEMTAX. To immobilize MTs on coverslips, flow channels were prepared using coverslips coated with poly-L-lysine.

DNA stretching

Double tagged dsDNA

A 3039-bp dsDNA coding for a fragment of the*blr-1*gene of*Trichoderma atroviride*was amplified by standard polymerase chain reaction (PCR). To allow attachment of the dsDNA to a polystyrene bead and to the coverslip, two functionalized PCR primers (Integrated DNA Technologies) were used: a forward primer (biotin-5′-GGGCTTCTACCAGACAAACCA-3′), and a reverse primer (digoxigenin-5′-CGCTCTTCTCGTATTGAAGCC-3′). The reaction tube contained: 5.0 µL of the 5XPCR buffer (Promega), 2.5 µL of 25-mM $MgCl_2$(Promega), 0.5 µL of 100-mM dNTPs, 0.5 µL of 10-µM reverse primer, 0.5 µL of 10-µM forward primer, 1.0 µL of cDNA from the*blr-1*gene (generous gift of Sergio Casas Flores, IPICYT, Mexico), 0.5 µL of Taq Polimerase (GoTaq, Promega), diluted in 15 µL of Milli-Q water. The PCR ran for 25 cycles with an alignment temperature of 58°C and 1 min for extension. The amplified fragment was purified using a QIAQuick PCR purification kit (Qiagen). The expected length of the dsDNA molecule is ∼1053 nm, computed by taking into account a 3039-bp chain with 0.34 nm rise per bp, together with ∼20 nm for the biotin-streptavidin and digoxigenin-anti-digoxigenin linkages.

Stretching of a single dsDNA assay

A solution of 0.05 mg/mL of antidigoxigenin (3210–0488, Spherotech) in phosphate buffer saline (137 mM NaCl, 2.7 mM KCl, 10 mM Na_2HPO_4, 2 mM KH_2PO_4) was introduced in a flow channel, and incubated for 10 min. After washing with 200 µL of washing buffer (5 mg/mL BSA, 77.4 mM Na_2HPO_4, 0.1% Tween), the channel was filled with a sample of 0.25 nM dsDNA diluted in phosphate buffer (77.4 mM Na_2HPO_4), and incubated for 10 min. Unbound DNA was removed by flowing 200 µL of washing buffer through the channel. Finally, 30 µL of 730-nm diameter, avidin-coated beads (generous gift of Steven Block, Stanford University), diluted in phosphate buffer to a final concentration of ∼1 pM, were introduced into the channel, and the flow cell was sealed using nail polish.

Single molecule kinesin stepping assay

Kinesin expression

We expressed the homodimeric, recombinant kinesin construct DmK401, a His-tagged derivative of *Drosophila melanogaster* kinesin heavy chain, that includes the first 401 N-terminal residues. Briefly, BL21(DE3) cells transformed with plasmid pCA1 (generous gift of Steven Block, Stanford University) were grown to logarithmic phase in Luria Broth medium (10 g/L tryotone, 5 g/L yeast extract, 10 g/L NaCl) supplemented with 0.1 mg/mL ampicillin (GIBCO). Kinesin expression was chemically induced with 1 mM IPTG (Invitrogen) at 27°C during 12 h. Cells were lysed by sonication in extraction buffer (200 mM Na_2HPO_4, 50 mM NaCl, 2 mM imidazole, 20 uM ATP, 2 mM $MgCl_2$, 1 mM DTT, 1 mM phenylmethylsulfonyl fluoride (PMSF), and protease inhibitor cocktail (P8465, Sigma); 1% Tween was added after sonication). Cellular lysate was clarified by centrifugation (30 min, 15,000 rpm, 4°C). Clarified lysate was stored at −20°C in 10% glycerol, and used in motility assays.

Polystyrene bead coating with purified kinesin protein

Briefly, 10 µL of the stock solution of 540-nm diameter, streptavidin-coated beads (Spherotech, SVP-05–10) were diluted in 70 µL of PEMBSA buffer (4 mg/mL BSA, 80 mM PIPES, 1 mM EDTA, 4 mM $MgCl_2$, pH 6.9), and sonicated for 10 min., after which 20 µL of penta-His biotin conjugate antibody (34440, Qiagen) were added. After incubating for 1 hour at room temperature, beads were washed 5 times by centrifugation, and stored at 4°C. To prepare the kinesin-bead complex, antibody-coated beads were diluted in assay buffer (3 mg/mL BSA, 0.05 M potassium acetate, 100 µM ATP, 1 µM DTT, 80 mM PIPES, 1 mM EDTA, 4 mM $MgCl_2$, 0.02 mM Taxol (TXD01, Cytoskeleton), pH 6.9), sonicated, and incubated for 12 h at 4°C with clarified lysate diluted in assay buffer at various concentrations.

Kinesin motility assay

Flow channels were prepared using coverslips coated with poly-L-lysine. Stabilized MTs were diluted 1:100 in PEMTAX buffer (0.02 mM Taxol, 80 mM PIPES, 1 mM

EDTA, 4 mM $MgCl_2$, pH 6.9), and were introduced into the flow channel and incubated for 10 min. Unbound MTs were removed by washing the channel with 40 µL of PEMTAX. Then the channel was washed first with 60 µL of 20 mg/mL BSA diluted in PEMTAX (to minimize the sticking of beads to the coverslip surface), and then with 100 µL of assay buffer (3 mg/mL BSA, 0.05 M potassium acetate, 100 µM ATP, 1 µM DTT, 80 mM PIPES, 1 mM EDTA, 4 mM $MgCl_2$, 0.02 mM Taxol, pH 6.9). Finally, 40 µL of kinesin-bead complexes were introduced into the channel and the flow cell was sealed. To minimize the presence of reactive oxygen species, final samples were protected with an oxygen scavenger system (0.25 mg/mL glucose oxidase, 0.03 mg/mL catalase, 4.7 mg/mL beta-D-glucose (MP Biomedicals)). To ensure motility in the single-molecule regime, kinesin dilutions were used in which only ~50% of the tested beads in a given sample displayed movement.

pPSF acquisition and *E. coli* visualization

Samples of 100 nm beads

Microscope slides and coverslips were cleaned prior to use for 5 min in a plasma cleaner (Harrick Plasma) at 1 Torr (ambient air). Flow channels were made using double-sided tape. Polystyrene beads of 100 nm in diameter (Invitrogen, F8803) were diluted 1:100 from the stock in miliQ water and sonicated during 10 min, followed by a second 1:100 dilution in miliQ water and sonication over additional 10 min. After a final 1:100 dilution in HEPES buffer (50 mM HEPES, 10 mM $MgCl_2$, pH 7.5) beads were introduced into a flow channel and allowed to bind to the coverslip

Samples of bacteria

E. coli TOP10 cells were grown overnight in Luria Broth medium. A sample of a 1:100 dilution in fresh medium was introduced into flow channels. Coverslips were used uncoated or coated with poly-L-lysine. Experiments were performed at room temperature, (22±2)°C.

Optical Microscopy and CEBFM

We perform background subtraction and frame averaging on all our images. To eliminate unwanted, uneven background arising from specks of dust or reflections inlenses, a total of 250 frames are captured and averaged to produce a single background frame that is subsequently subtracted from all incoming frames. Background subtraction is further optimized by displacing the microscope stage in 3D (along non-closed paths covering distances of a few micrometers) while background frames are taken. This last action is performed with the piezoelectric stage on which the sample is mounted, and has the effect of averaging out intensity contributions in the final background image due to small debris found on the coverslip surface. We reduce electronics noise by arithmetical averaging of 50 background-free frames, producing a single low-noise, high-contrast image of a given subject at a specified *z*-position. A typical *z*-stack of 70 frames is acquired in ~2.5 min, and stored as a set of text files for further processing/analysis. During processing, the original 8-bit images are converted to 16-bit and carried out in that form throughout. Image acquisition and digital processing was performed using LabView 8.5 (add-on package Vision, National Instruments).

LOV-domains expression and purification

For all LOV-domains expressed the procedure was the same; an inoculum was left overnight at 37°C with constant shaking, then a 1:100 dilution in fresh Luria Broth (LB) was done and the culture was grew until 0.4-0.6 O.D with constant shaking at 37°C. Then after 15 min shaking at 18°C the culture was induced with 100 □M of IPTG. For proteins expressing a biotin binding tag 5 μM biotin was added to the LB medium. The induction was left for 22 hours shaking at 18°C under constant illumination. The cells were harvest and flash freeze.

For protein purification, the pellet was resuspended on Extraction Buffer (10% glycerol, 150 mM NaCl, 50mM HEPES, pH 8, inhibition cocktail EDTA free and 1% Triton X-100) and lysed by sonication (6 pulses of 20 s with pauses of 40 s). The lysate fraction was spin at 15000 rpm at 4°C for 30min.

The clarified supernatant was passed through the corresponding resin (Ni-NTA, Glutathione resin, SoftLink Avidin Resin) and onwards the proteins were kept at 4°C.

After three wash steps with corresponding Wash Buffer (for Ni agarose resin: 10% glycerol, 150 mM NaCl, 50mM HEPES, 10mM Imidazole, pH 8; for Glutathione resin and SoftLink Avidin Resin: 10% glycerol, 150 mM NaCl, 50mM HEPES, pH 8) the protein was released with Elution Buffer (for Ni agarose resin: 10% glycerol, 150 mM NaCl, 50mM HEPES, 200mM imidazole pH 8; for Glutathione resin: 10% glycerol, 150 mM NaCl, 50mM HEPES, 10mM reduced glutathione, pH 8, for SoftLink resin: 10% glycerol, 150 mM NaCl, 50 mM HEPES, 5 mM biotin, pH8)

Aggregation assays

Aggregation kinetics. Stored protein samples were resuspended to the proper glycerol and initial protein concentrations. For all samples the final buffer (DB) composition was:20 mM imidazole, 150 mM NaCl, 50 mM HEPES, pH8, and glycerol content was 10% unless otherwise specified. Samples containing 150 μL each were loaded on the flat bottom of a 96–well plate, and 70 μL of mineral oil was added at the top of each well to avoid evaporation. To establish the initial condition, a BL LED (Sink PADII, Royal-Blue, λ = 440-460 nm, Luxeon) was used to illuminate the plate for 5 min, which was then taken to a microplate spectrophotometer (Synergy, Biotek), and absorption spectra (300-600nm) were acquired every 30 min at constant, controlled temperature (25°C, unless otherwise specified). All the tested proteins or molecules used to probe effects on the aggregation of VVD (GSH, DTT, trolox, dimethylurea, propyl gallate, BSA, linoleic acid-oleic acid-albumin, superoxide dismutase, catalase, glucose, glucose oxidase, and glycerol) were first resuspended in DB and then added fresh to the VVD samples.

Effect of consecutive BL pulses on aggregation. VVD samples were loaded on the 96-well plate and illuminated for 5 min with BL. Absorption spectra were then acquired every 12 min in otherwise dark conditions, and after 48 min the plate was re–illuminated during 5 min with BL and the acquisition of spectra was resumed. This

re–illumination sequence was repeated up to 4 times. As a control experiment, an initial BL pulse was given, followed by the same re–illumination procedure but now using a red LED (Sink PADII, Deep Red, λ = 650-670 nm, Luxeon).

Effect of temperature over VVD aggregation. VVD samples were loaded in a 96–well plate where a BL pulse was applied, and left to incubate during 4 h in dark conditions at different temperatures. Levels of protein aggregation were measured by recording the absorbance at λ=550 nm for all samples. Measured absorbance in a 50% glycerol (unaggregated) VVD sample was used as a control and to establish the base line absorption value. Different temperature data were normalized with respect to the measured absorption at 37°C. Adduct mean lifetimes at different temperatures were obtained from exponential fits to absorption recovery data at λ=450 nm, measured every 30 min. To avoid aggregation of VVD at high temperatures, the oxygen scavenger system was added.

Western Blot

To detect oligomers in aggregated VVD, Penta-His biotin conjugate (QIAGEN, cat. 34440) and ultra–sensitive Streptavidin–Peroxidase Polymer were used in standard SDS–PAGE and Western blot assays. To detect carbonyl groups, three sample conditions at the same protein concentration were evaluated. A fresh resuspended sample (unaggregated), a sample incubated for over 12 h at 25°C (aggregated) and an intentionally oxidized VVD sample (incubated during 15 min with 1.5 mM $NiCl_2$ and 33 mM H_2O_2) were supplemented with 5 mM biotin-hydrazide and left to incubate for 3 h at room temperature. Ultra-sensitive streptavidin peroxidase polymer was used to detect the biotin-hydrazide label.

Mass Spectrometry

The pellet fraction of an aggregated sample was loaded on a SDS-PAGE gel. The protein band was excised from the gel and reduced with 10 mM DTT, 25 mM ammonium bicarbonate, followed by protein alkylation with 55 mM iodacetamide. Protein was digested with Trypsin Gold (PROMEGA, V5280). Nanoscale LC separation of tryptic peptides was performed with a nanoACQUITY UPLC System (Waters, Milford, MA, USA) and tandem mass spectrometry analysis was carried

out in a SYNAPT HDMS (Waters). MS/MS data sets were used to generate PKL files using the Protein Lynx Global Server v2.4 (PLGS, Waters). Proteins were then identified using PKL files and the MASCOT software. Searches were conducted against the NCBI protein database.

Oligos for DNA tethering

Digoxigenin tag: 5'-DigN-GGG CTT CTA CCA GAC AAA CCA-3´

Biotin tag5'-Biotin-CGC TCT TCT CGT ATT GAA GCC-3'

To prepare a DNA-protein conjugate using histidine-tag (His-tag) chemistry "Biotechnol Lett. 2008 Nov;30(11):2001-6. doi: 10.1007/s10529-008-9784-4."

5'-NTA (GenLink Cat. no. 26-6444-02)-GGGCTTCTACCAGACAAACCA-3'

Oligos for tagged protein

Some constructions were first tried with pET28(Dr SCF) but the sequence in this vector was mutated and the 6xHis tag was missing. So the constructions were made in pET28(Dr. Samuel) where the 6xHis tag was not mutated but the thrombin site was interchanged for a PreScission cleavage site.

F-Biot-VVD XhoI GG

5´GAGATCTCGAGTCATTCATGCCATTCAATTTTTTGTGCTTCAAAAATATCATTCAGAC CACCACCTTCCGTTTCGCACTGGAAACCCAT-3'

F-49envoy-BioTag GG

5´GAGATCTCGAGTCATTCATGCCATTCAATTTTTTGTGCTTCAAAAATATCATTCAGAC CACCACCTACTTCGGCTTGTAACCCGACGGCATA-3´

R-BioTag 49envoy 15aa

5´CATGCCATGGGTCTGAATGATATTTTTGAAGCACAAAAAATTGAATGGCATGAATCC GTGATATATCCTGGCATTTACTCGGCT-3´

R-6His VVD

5´CTTCTACATATGATGTATACGATCTACGCTCCCGGCGGT-3´

F-6His envoy

5′GAGATCTCGAGTCATACTTCGGCTTGTAACCCGACGGC-3′

R 6His 49envoy

5′CTTCTACATATGTCCGTGATATATCCTGGCATTTACTCGGCT-3′

R-6His-Envoy

5′CTTCTACATATGGTTCCTTCAGGGTCTTCAAAACTACCG-3′

F-49envoy-6His

5′GAGATCTCGAGTACTTCGGCTTGTAACCCGACGGCATA-3′

GST-ENVOY(Δ49)-6HIS. pGEX, Ampicillin, BL21(DE3)

GST-LOVBLR1-6HIS. pGEX, Ampicillin, BL21(DE3)

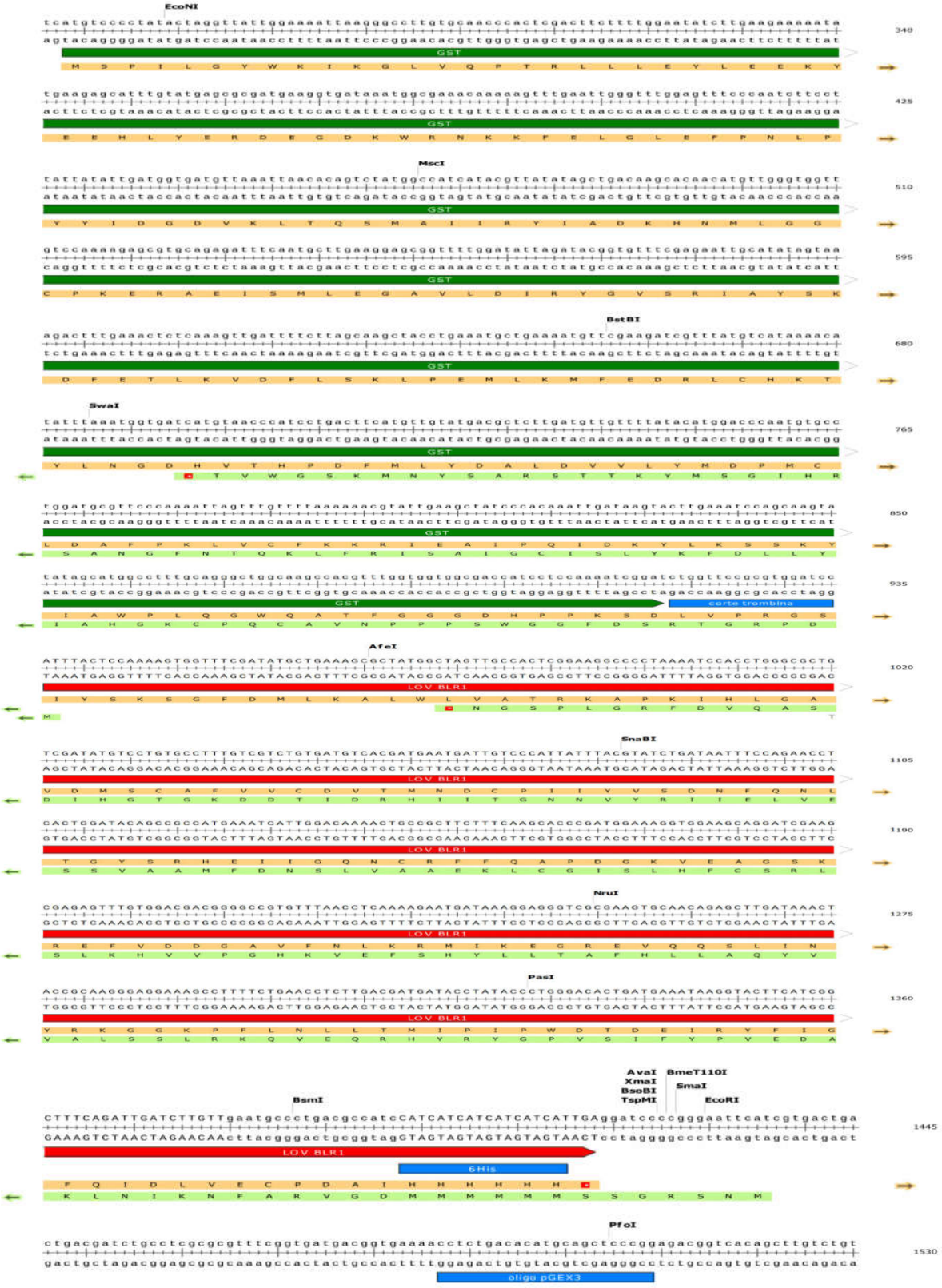

6HIS-ENVOY(Δ49). pET28 (Dr.Samuel),TOP10, kanamycin NOTE: This construction was not corroborated by sequencing.

6HIS-ENVOY(Δ49)-BiotinTag. pET28(Dr.Samuel), BL21(DE3), kanamycin

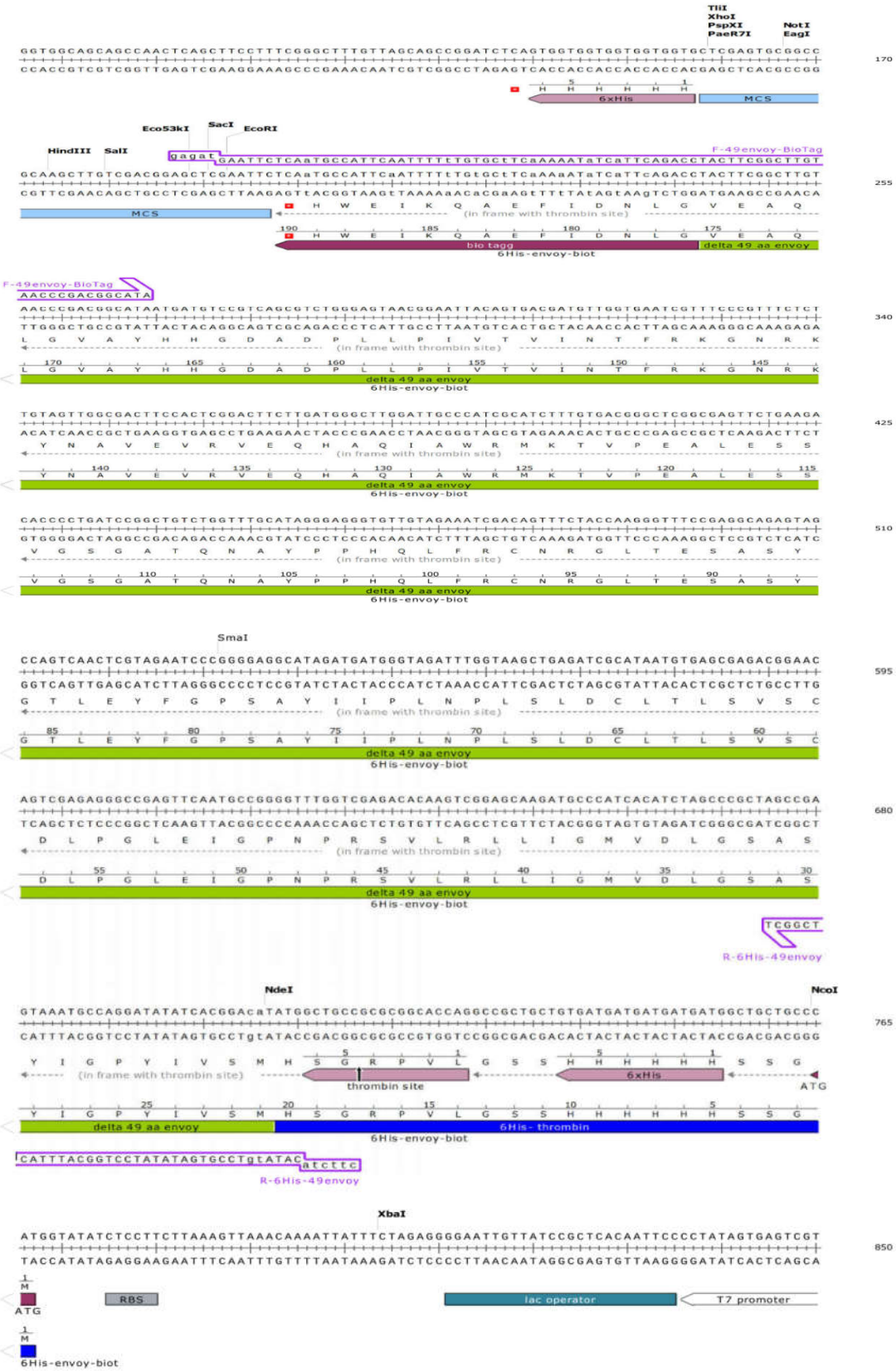

6HIS-ENVOY. pET28(Dr.Samuel), BL21(DE3), kanamycin

StrepTagII-VVD-6HIS (buy to DNA 2.0). pD441-SR:T5-sRBS-ORF. kanamycin

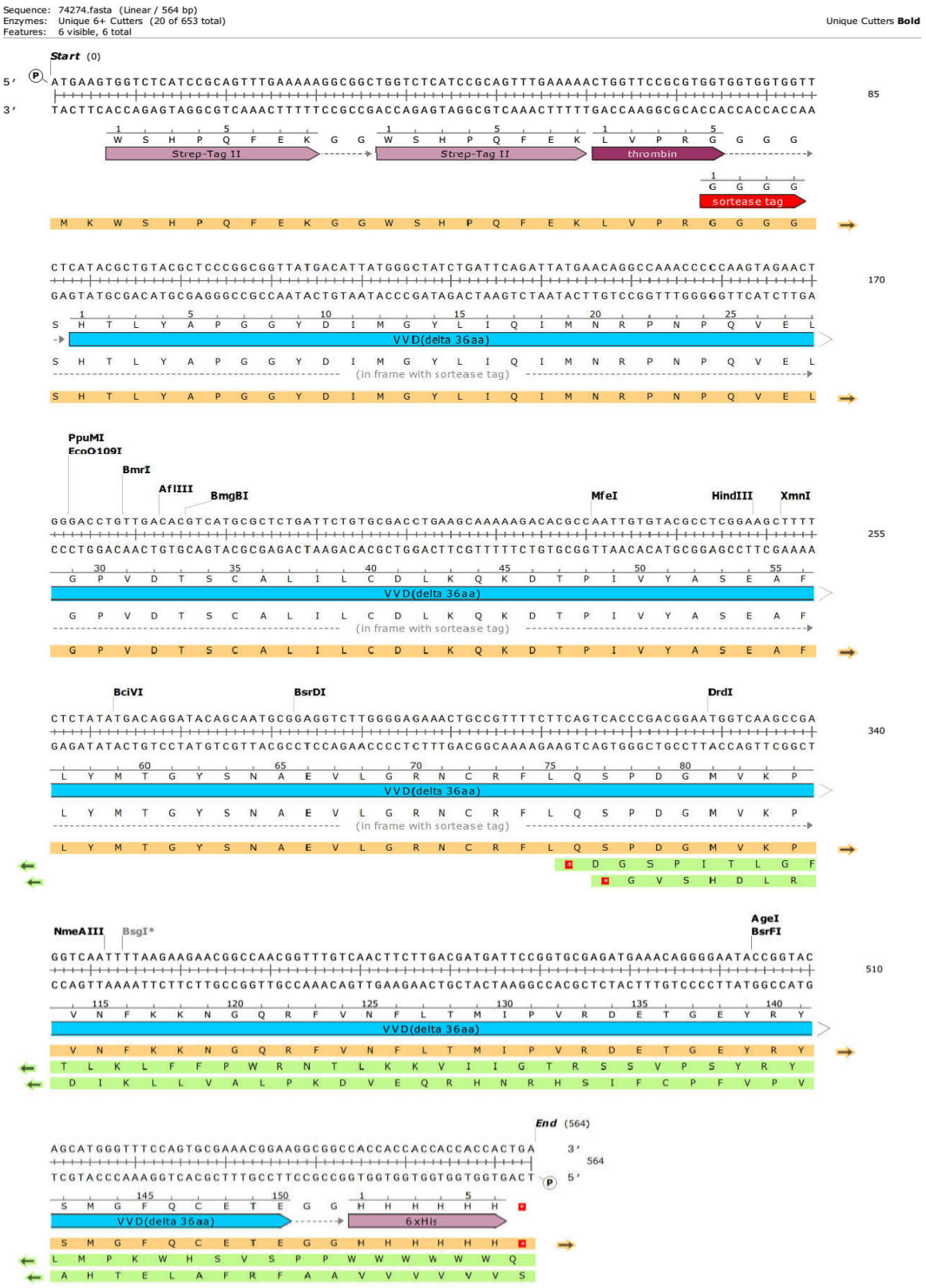

Vector pET28 (Dr. Samuel)

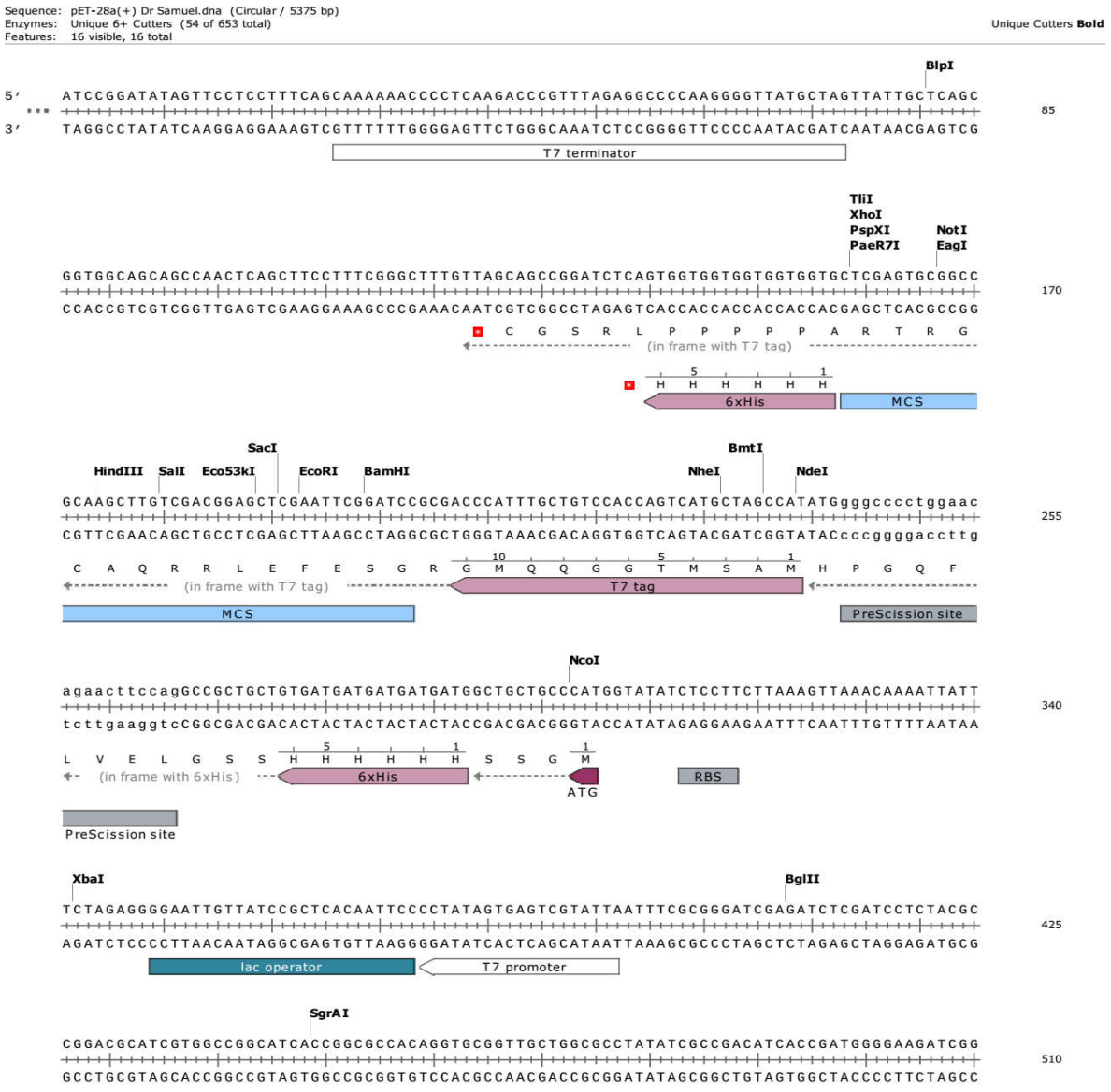

Appendix B

OPEN ACCESS Freely available online

PLOS | ONE

Direct Imaging of Phase Objects Enables Conventional Deconvolution in Bright Field Light Microscopy

Carmen Noemí Hernández Candia[1], Braulio Gutiérrez-Medina[2]*

1 Program in Molecular Biology, Instituto Potosino de Investigación Científica y Tecnológica, San Luis Potosí, Mexico, **2** Advanced Materials Division, Instituto Potosino de Investigación Científica y Tecnológica, San Luis Potosí, Mexico

Abstract

In transmitted optical microscopy, absorption structure and phase structure of the specimen determine the three-dimensional intensity distribution of the image. The elementary impulse responses of the bright field microscope therefore consist of separate absorptive and phase components, precluding general application of linear, conventional deconvolution processing methods to improve image contrast and resolution. However, conventional deconvolution can be applied in the case of pure phase (or pure absorptive) objects if the corresponding phase (or absorptive) impulse responses of the microscope are known. In this work, we present direct measurements of the phase point- and line-spread functions of a high-aperture microscope operating in transmitted bright field. Polystyrene nanoparticles and microtubules (biological polymer filaments) serve as the pure phase point and line objects, respectively, that are imaged with high contrast and low noise using standard microscopy plus digital image processing. Our experimental results agree with a proposed model for the response functions, and confirm previous theoretical predictions. Finally, we use the measured phase point-spread function to apply conventional deconvolution on the bright field images of living, unstained bacteria, resulting in improved definition of cell boundaries and sub-cellular features. These developments demonstrate practical application of standard restoration methods to improve imaging of phase objects such as cells in transmitted light microscopy.

Citation: Hernández Candia CN, Gutiérrez-Medina B (2014) Direct Imaging of Phase Objects Enables Conventional Deconvolution in Bright Field Light Microscopy. PLoS ONE 9(2): e89106. doi:10.1371/journal.pone.0089106

Editor: Jonathan A. Coles, Glasgow University, United Kingdom

Received November 9, 2013; **Accepted** January 19, 2014; **Published** February 18, 2014

Funding: This work was supported by grant Fondos Sectoriales-SEP-2009 (CB-2009/133053) from Consejo Nacional de Ciencia y Tecnología (CONACYT, http://www.conacyt.gob.mx) to BG. The funders had no role in study design, data collection and analysis, decision to publish, or preparation of the manuscript.

Competing Interests: The authors have declared that no competing interests exist.

* E-mail: bgutierrez@ipicyt.edu.mx

Introduction

Optical imaging systems present aberrations, diffraction effects at apertures and out-of-focus intensity contributions that result in images affected by blur. Consequently, the image of a point object is an extended, three-dimensional (3D) distribution of intensity (the point-spread function, PSF) [1]. Likewise, the image of a pure line object is the two-dimensional (2D) line-spread function (LSF) [2]. In terms of spatial frequency, the effects of blurring are characterized by the optical transfer function (OTF), the Fourier transform of the PSF. The point- and line-spread functions (and the corresponding transfer functions) are characteristic of linear, shift-invariant optical systems [3] and their knowledge provides valuable information to perform deconvolution image processing (or restoration), a powerful technique that removes blur [4].

In light microscopy, deconvolution processing has traditionally been linked to fluorescence–to the extent that the termì deconvolution microscopy" almost always assumes this microscopy modality [5–8]. A main reason behind this association is that for the case of self-luminous objects one needs only to consider signal intensity, leading to a unique spread function and making deconvolution a linear process. This is not the case in transmitted light microscopy, where two spread functions are needed to describe image formation, as discussed below. In the case of fluorescence, the 3D image of an object $i(x,y,z)$ is given by the convolution of the object intensity distribution $o(x,y,z)$ with the PSF(x,y,z):

$$i = o \otimes \mathrm{PSF}, \tag{1}$$

where the symbol $\otimes$ denotes the convolution operation. Therefore, the object intensity distribution can be determined (through deconvolution) if the PSF is known. Accordingly, several approaches have been developed for the evaluation of the PSF [5–8]. Theoretical computations of the fluorescence PSF often model light propagation along idealized imaging optics. Conversely, the PSF is experimentally measured by immobilizing on a coverslip a fluorescent bead of size below ($\sim 1/3$) the resolution limit of the microscope, followed by imaging the bead at different axial positions. The resulting stack of 2D images is the 3D PSF, which takes into account both aberration and diffraction effects present in the microscope. Despite its tremendous success and extensive use, fluorescence deconvolution microscopy requires exogenous tags and is susceptible to the effects of photostability and phototoxicity induced by the excitation light [9] during applications such as live-cell imaging.

Bright field (BF) microscopy has been proposed as an alternative to fluorescence in deconvolution image processing due to its simplicity and the possibility to observe unstained objects on a continuous basis over extended periods of time. However, its practical realization has been scarce, mainly because, unlike fluorescence, the corresponding PSF is not unique. In a classic analysis of the transmitted light microscope, Streibl showed that

OPEN ACCESS Freely available online

PLOS ONE

A Minimal Optical Trapping and Imaging Microscopy System

Carmen Noemí Hernández Candia[1], Sara Tafoya Martínez[2¤], Braulio Gutiérrez-Medina[3]*

1 Program in Molecular Biology, Instituto Potosino de Investigación Científica y Tecnológica, San Luis Potosí, Mexico, **2** Program in Physics, Universidad Autónoma de San Luis Potosí, San Luis Potosí, Mexico, **3** Advanced Materials Division, Instituto Potosino de Investigación Científica y Tecnológica, San Luis Potosí, Mexico

Abstract

We report the construction and testing of a simple and versatile optical trapping apparatus, suitable for visualizing individual microtubules (~25 nm in diameter) and performing single-molecule studies, using a minimal set of components. This design is based on a conventional, inverted microscope, operating under plain bright field illumination. A single laser beam enables standard optical trapping and the measurement of molecular displacements and forces, whereas digital image processing affords real-time sample visualization with reduced noise and enhanced contrast. We have tested our trapping and imaging instrument by measuring the persistence length of individual double-stranded DNA molecules, and by following the stepping of single kinesin motor proteins along clearly imaged microtubules. The approach presented here provides a straightforward alternative for studies of biomaterials and individual biomolecules.

Citation: Hernández Candia CN, Tafoya Martínez S, Gutiérrez-Medina B (2013) A Minimal Optical Trapping and Imaging Microscopy System. PLoS ONE 8(2): e57383. doi:10.1371/journal.pone.0057383

Editor: Alexandre J. Kabla, University of Cambridge, United Kingdom

Received October 31, 2012; **Accepted** January 21, 2013; **Published** February 25, 2013

Funding: This work was supported by grant Fondos Sectoriales-SEP-2009 (S-3158) from Consejo Nacional de Ciencia y Tecnología (CONACYT, http://www.conacyt.gob.mx) to BG, and by a UC MEXUS-CONACYT (http://ucmexus.ucr.edu/) grant and a George E Brown Jr Award to BG. The funders had no role in study design, data collection and analysis, decision to publish, or preparation of the manuscript.

Competing Interests: The authors have declared that no competing interests exist.

* E-mail: bgutierrez@ipicyt.edu.mx

¤ Current address: Program in Biophysics, University of California, Berkeley, California, United States of America

Introduction

Over the last two decades, optical traps (or optical tweezers) have become a standard tool in the physical and biological sciences, allowing the measurement of sub-nanometer displacements of optically trapped microparticles, as well as the exertion of piconewton-level, controlled forces on these particles [1,2,3]. Taking advantage of this versatility, studies on the mechanical and biochemical properties of biomolecules at the single-molecule level using optical tweezers are now widespread. In these assays, individual molecules, attached to trapped particles, can be pulled on or stretched (or even twisted) using the laser trap, and the molecular displacement and force (or torque) responses can be measured with high spatial (~1 nm) and temporal (~100 kHz) resolution [4]. These experiments provide unique information on molecular mechanisms that complement traditional biochemical studies.

Typically, an optical tweezers arrangement consists of a single laser beam tightly focused by a microscope objective of high numerical aperture (NA) (1.0–1.4), which traps microparticles near its focal point [5,6]. Position detection of the trapped particle relative to the laser beam axis is achieved through back focal plane (BFP) detection, where the trapping beam (or a secondary beam of low-power) is directed to a position-sensitive detector (PSD) located in a plane conjugate to the condenser BFP [7]. In many trapping setups, these requirements are implemented by substantial modifications of a commercial inverted light microscope in order to accommodate holders, mounts, and a stable stage platform fitted with a piezoelectric stage (for fine sample movement). Alternatively, an optical trap can be built entirely from individual optical components, providing increased flexibility in the design, often reducing costs, and facilitating the choice of parts. This last option is the one we have followed in this work.

Successful development of an optical tweezers apparatus often requires appropriate means to visualize small objects (~20–200 nm). Indeed, a variety of cellular and single-molecule assays require the localization and subsequent tracking of nanoparticles [8], or the imaging of individual slender polymer filaments such as microtubules (MTs, with diameters of only ~25 nm) [9]. Because small objects scatter light weakly, their visualization has traditionally not been performed using bright field microscopy. Instead, localization is achieved by employing a number of specialized imaging techniques, in the case of MTs: fluorescence [10], dark field [11], polarization [12], phase contrast [11], or Nomarski differential interference-contrast (DIC) microscopy [13]. However, some of these visualization methods exhibit inherent limitations in the context of optical trapping. For example, it is well-known that the Wollaston prisms required in DIC optics can introduce significant asymmetries in the optical trap [14]. Likewise, because the Wollaston prisms generally produce or recombine two displaced beams with orthogonal polarizations, DIC microscopy prohibits the operation of an optical tweezers setup where polarization of the trapping beam requires high purity and independent adjustment (as in an "optical torque wrench" [15]). Introducing optical elements such as prisms, apertures, phase masks, or polarizers in the laser beam path unavoidably constrains the possibilities for optical trapping, especially when control of phase or polarization effects is necessary, as in holographic [16] or interferometric [17] optical tweezers.